

**Combining body wave tomography,  
surface wave inversion, seismic interferometry  
and laboratory measurements to characterize the  
black shales on Bornholm at different scales**

**Dissertation  
zur Erlangung des akademischen Grades  
"doctor rerum naturalium"  
(Dr. rer. nat.)  
in der Wissenschaftsdisziplin "Geophysik"**

**eingereicht an der  
Mathematisch-Naturwissenschaftlichen Fakultät  
der Universität Potsdam**

**von  
Maria Baumann-Wilke**

**Potsdam, im Juni 2013**

This work is licensed under a Creative Commons License:  
Attribution - Noncommercial - Share Alike 3.0 Germany  
To view a copy of this license visit  
<http://creativecommons.org/licenses/by-nc-sa/3.0/de/>

Published online at the  
Institutional Repository of the University of Potsdam:  
URL <http://opus.kobv.de/ubp/volltexte/2013/6900/>  
URN [urn:nbn:de:kobv:517-opus-6900](http://nbn-resolving.org/urn:nbn:de:kobv:517-opus-6900)  
<http://nbn-resolving.de/urn:nbn:de:kobv:517-opus-69007>

---

## Abstract

Black shales are sedimentary rocks with a high content of organic carbon, which leads to a dark grayish to black color. Due to their potential to contain oil or gas, black shales are of great interest for the support of the worldwide energy supply. An integrated seismic investigation of the Lower Palaeozoic black shales was carried out at the Danish island Bornholm to locate the shallow-lying Alum Shale layer and its surrounding formations and to characterize its potential as a source rock. Therefore, two seismic experiments at a total of three crossing profiles were carried out in October 2010 and in June 2012 in the southern part of the island. Two different active measurements were conducted with either a weight drop source or a minivibrator. Additionally, the ambient noise field was recorded at the study location over a time interval of about one day, and also a laboratory analysis of borehole samples was carried out. The seismic profiles were positioned as close as possible to two scientific boreholes which were used for comparative purposes.

The seismic field data was analyzed with travelttime tomography, surface wave inversion and seismic interferometry to obtain the P-wave and S-wave velocity models of the subsurface. The P-wave velocity models which were determined for all three profiles clearly locate the Alum Shale layer between the Komstad Limestone layer on top and the Læså Sandstone Formation at the base of the models. The black shale layer has P-wave velocities around 3 km/s which are lower compared to the adjacent formations. Due to a very good agreement of the sonic log and the vertical velocity profiles of the two seismic lines, which are directly crossing the borehole where the sonic log was conducted, the reliability of the travelttime tomography is proven. A correlation of the seismic velocities with the content of organic carbon is an important task for the characterization of the reservoir properties of a black shale formation. It is not possible without calibration but in combination with a full 2D tomographic image of the subsurface it gives the subsurface distribution of the organic material.

The S-wave model obtained with surface wave inversion of the vibroseis data of one of the profiles images the Alum Shale layer also very well with S-wave velocities around 2 km/s. Although individual 1D velocity models for each of the source positions were determined, the subsurface S-wave velocity distribution is very uniform with a good match between the single models. A really new approach described here is the application of seismic interferometry to a really small study area and a quite short time interval. Also new is the selective procedure of only using time windows with the best crosscorrelation signals to achieve the final interferograms. Due to the small scale of the interferometry even P-wave signals can be observed in the final crosscorrelations.

In the laboratory measurements the seismic body waves were recorded for different pressure and temperature stages. Therefore, samples of different depths of the Alum Shale were available from one of the scientific boreholes at the study location. The measured

velocities have a high variance with changing pressure or temperature. Recordings with wave propagation both parallel and perpendicular to the bedding of the samples reveal a great amount of anisotropy for the P-wave velocity, whereas the S-wave velocity is almost independent of the wave direction. The calculated velocity ratio is also highly anisotropic with very low values for the perpendicular samples and very high values for the parallel ones. Interestingly, the laboratory velocities of the perpendicular samples are comparable to the velocities of the field experiments indicating that the field measurements are sensitive to wave propagation in vertical direction.

The velocity ratio is also calculated with the P-wave and S-wave velocity models of the field experiments. Again, the Alum Shale can be clearly separated from the adjacent formations because it shows overall very low  $v_P/v_S$  ratios around 1.4. The very low velocity ratio indicates the content of gas in the black shale formation. With the combination of all the different methods described here, a comprehensive interpretation of the seismic response of the black shale layer can be made and the hydrocarbon source rock potential can be estimated.



---

## Zusammenfassung

Schwarzschiefer sind Sedimentgesteine, die einen hohen Gehalt an organischem Kohlenstoff aufweisen, was zu einer dunkelgrauen bis schwarzen Färbung führt. Da Schwarzschiefer das Potenzial besitzen, Öl oder Gas zu enthalten und somit zur weltweiten Energieversorgung beitragen könnten, sind sie von großem Interesse. Mit Hilfe der Kombination verschiedener seismischer Messverfahren wurden die Schwarzschiefer des Unteren Paläozoikums auf der dänischen Insel Bornholm untersucht um den oberflächennahen Alaunschiefer und dessen Umgebungsgestein dort zu lokalisieren und sein Potenzial als Muttergestein abzuschätzen. Dafür wurden im Oktober 2010 und im Juni 2012 im südlichen Teil der Insel zwei seismische Experimente auf insgesamt drei sich kreuzenden Profilen durchgeführt. Für zwei aktive seismische Messungen wurden ein Fallgewicht und ein Minivibrator als Quellen genutzt. Zusätzlich wurde im Messgebiet noch das Wellenfeld des umgebenden Rauschens über einen Zeitraum von etwa einem Tag aufgezeichnet. Außerdem wurden Labormessungen an Bohrkernen aus dem Alaunschiefer durchgeführt. Die seismischen Messprofile befanden sich so nah wie möglich an zwei wissenschaftlichen Bohrungen, die für Vergleichszwecke genutzt wurden.

Um die P- und S-Wellengeschwindigkeitsmodelle des Untergrundes zu erhalten wurden die seismischen Felddaten mittels Laufzeitomographie, Oberflächenwelleninversion und seismischer Interferometrie ausgewertet. Die P-Wellenmodelle, die für alle drei seismischen Profile erstellt wurden, zeigen den Alaunschiefer zwischen dem Komstad Kalkstein, der den Alaunschiefer überdeckt, und der Læså Sandsteinformation, die die Basis der Modelle bildet. Für die Schwarzschieferschicht ergeben sich mit rund 3 km/s deutlich geringere P-Wellengeschwindigkeiten als für die umgebenden Gesteine. Zwei seismische Profile liegen direkt an einer der Bohrungen, für die verschiedene Bohrloch-Logs durchgeführt wurden. Der Vergleich des Sonic-Logs mit den vertikalen Geschwindigkeitsprofilen beider Modelle am Bohrpunkt zeigt eine sehr gute Übereinstimmung aller Geschwindigkeiten. Dies ist ein Indiz für die Plausibilität der durchgeführten Laufzeitomographie. Um die Reservoirereigenschaften der Schwarzschieferschicht einordnen zu können, wurde versucht, die seismischen Geschwindigkeiten mit dem Gehalt an organischem Material zu korrelieren. Ohne geeignete Kalibrierung ist diese Korrelation schwierig, kann aber mit Hilfe der Tomographieergebnisse ein zweidimensionales Abbild der Verteilung des organischen Materials im Untergrund liefern.

Auch das S-Wellengeschwindigkeitsmodell, welches mit der Oberflächenwelleninversion der Vibroseisdaten erstellt wurde, bildet den Alaunschiefer gut ab. Hierbei zeigen sich S-Wellengeschwindigkeiten um 2 km/s. Obwohl jeweils nur 1D-Modelle für jede Quellposition bestimmt wurden, ergibt sich für die gesamte Untergrundstruktur des untersuchten Profils ein einheitliches Bild der Geschwindigkeiten. Einen sehr neuen Ansatz bildet die Anwendung der seismischen Interferometrie auf ein sehr kleines Untersuchungsgebiet

und über einen sehr kurzen Zeitraum. Neu ist außerdem, dass für die Bestimmung der endgültigen Interferogramme nur Zeitfenster der Kreuzkorrelationen ausgewählt werden, in denen die Signalqualität hinreichend gut ist. In den berechneten Kreuzkorrelationen sind sogar P-Wellen enthalten, was auf die geringen Abstände der seismischen Rekorder zurück zu führen ist.

Bei den Labormessungen wurden die Raumwellen für verschiedene Drücke und Temperaturen aufgezeichnet. Die Messungen der Geschwindigkeiten sowohl parallel als auch senkrecht zur Schichtung der Proben zeigen eine starke Anisotropie für die P-Welle. Dagegen scheint die S-Wellengeschwindigkeit fast unabhängig von der Ausbreitungsrichtung der Wellen zu sein. Auch das Verhältnis der Geschwindigkeiten weist starke Anisotropie auf. Für die Wellenausbreitung senkrecht zur Schichtung zeigen sich sehr niedrige Werte, die Werte für die Messungen parallel zur Schichtung sind dagegen deutlich erhöht. Ein interessanter Aspekt der aus den Labormessungen resultiert ist, dass die Geschwindigkeit der Messungen senkrecht zur Schichtung mit den Geschwindigkeitswerten der Feldmessungen übereinstimmen. Damit scheinen die Feldmessungen besonders die Ausbreitung der Wellen in vertikaler Richtung zu registrieren.

Das Geschwindigkeitsverhältnis wurde auch mit den P- und S-Wellenmodellen der Feldexperimente berechnet. Auch hier hebt sich der Alaunschiefer mit deutlich verringerten Werten um 1.4 vom Umgebungsgestein ab. Solch geringe Werte für das Verhältnis der Geschwindigkeiten deutet auf den Gehalt von Gas im Schwarzschiefer. Mit der Kombination der verschiedenen Methoden ist es möglich, die seismische Antwort der Schwarzschieferschicht umfassend zu beschreiben und Schlussfolgerungen darüber zu ziehen, ob die hier untersuchte Schwarzschieferschicht das Potenzial hat als Kohlenwasserstofflagerstätte zu fungieren.

# Contents

<b>1</b>	<b>Introduction</b>	<b>1</b>
<b>2</b>	<b>Topic of study</b>	<b>5</b>
2.1	Black shales . . . . .	5
2.2	Seismic measurements . . . . .	6
2.3	Geology of Bornholm . . . . .	8
2.4	Integration of borehole information . . . . .	10
<b>3</b>	<b>Traveltime tomography</b>	<b>15</b>
3.1	Introduction . . . . .	15
3.1.1	Mathematical principles of traveltime tomography . . . . .	16
3.1.2	Model parametrization . . . . .	18
3.1.3	Ray-tracing . . . . .	18
3.2	Processing and inversion . . . . .	21
3.2.1	Data processing and traveltime picking . . . . .	21
3.2.2	Velocity modeling in one and two dimensions . . . . .	25
3.2.3	Resolution of the velocity models . . . . .	31
3.3	Results . . . . .	36
3.3.1	Final tomography models . . . . .	36
3.3.2	Comparison with borehole information . . . . .	40
3.3.3	Correlation to the TOC content . . . . .	41
3.4	Discussion and conclusions . . . . .	44
<b>4</b>	<b>Surface wave inversion</b>	<b>47</b>
4.1	Introduction . . . . .	47
4.1.1	Dispersive nature of surface waves . . . . .	48
4.1.2	The neighbourhood algorithm . . . . .	50
4.2	Data processing and inversion . . . . .	52
4.2.1	Processing of the SH vibroseis data . . . . .	52
4.2.2	Inversion with the neighbourhood algorithm . . . . .	53
4.2.3	The problem with low velocity zones . . . . .	55

---

4.3	Resulting S-wave velocity models . . . . .	56
4.4	Discussion and conclusions . . . . .	58
<b>5</b>	<b>Seismic interferometry</b>	<b>61</b>
5.1	Introduction . . . . .	61
5.2	Methodological background . . . . .	62
5.3	Data preparation . . . . .	64
5.4	Extracted interferograms . . . . .	67
5.5	Discussion and conclusions . . . . .	70
<b>6</b>	<b>Laboratory analysis</b>	<b>71</b>
6.1	Principles of ultrasonic measurements . . . . .	71
6.2	Ultrasonic measurements . . . . .	72
6.2.1	Sample preparation . . . . .	72
6.2.2	Experimental setup . . . . .	73
6.2.3	Wave recordings . . . . .	75
6.2.4	Dead time correction . . . . .	76
6.2.5	Error estimation . . . . .	77
6.3	Velocity data . . . . .	78
6.3.1	Velocity with temperature and pressure . . . . .	78
6.3.2	Velocity anisotropy . . . . .	84
6.4	Discussion and conclusions . . . . .	87
<b>7</b>	<b>Joint interpretation</b>	<b>91</b>
<b>8</b>	<b>Conclusions</b>	<b>97</b>
	<b>Acknowledgments</b>	<b>99</b>
	<b>References</b>	<b>105</b>
	<b>Appendix A - Velocity data of ultrasonic measurements</b>	<b>113</b>
	<b>Appendix B - Calculated anisotropy values</b>	<b>127</b>

# 1 Introduction

In recent years the interest in alternative hydrocarbon resources has increased. Conventional hydrocarbon resources are depleted more and more but the demand for oil and gas is still on a high level. Therefore, unconventional hydrocarbon resources, where the oil or gas is adsorbed in the rock formation, are getting in the focus to support the worldwide energy supply. Black shales are sedimentary rocks with a high content of organic carbon and may serve as hydrocarbon source rocks. With the interest in alternative energy resources also the interest in black shales increased. However, geophysical investigations of black shales are still rare (e. g., D. H. Johnston, 1987; Vanorio et al., 2008; Prasad et al., 2009).

In the work presented here, black shales are investigated with different seismic methods to extract parameters which are representative for the characterization of hydrocarbon resources. The study area is located in the southern part of the Danish island Bornholm. In that part of the island, the Lower Palaeozoic black shales of the Alum Shale Formation are present at shallow depth. They show a high content of organic carbon (Buchardt et al., 1986) and are thermally mature (Buchardt et al., 1997). Thus, it is likely that the Alum Shale on Bornholm has generated oil or gas.

The first investigation of seismic velocities on Bornholm was carried out by Sharma (1974) where outcrops of different formations were analyzed with refraction seismic. Sharma (1974) found the Alum Shale with considerably lower velocities ( $v_P = 2.6$  km/s) than the other Palaeozoic formations on Bornholm. The present work combines different seismic methods to analyze the shallow-lying Alum Shale and the adjacent formations in more detail. Therefore, active and passive experiments and a laboratory analysis of borehole samples were conducted to extract the P-wave and S-wave velocities and the velocity anisotropy. This integrated approach covers different scales and gives a comprehensive insight into the seismic response of black shales.

The topic of the study is presented in Chapter 2. First, a short overview is given about black shales in general. The deposition and properties of the sedimentary rock with the typical high amount of organic matter are briefly discussed. The geological setting of the area around and on Bornholm which is characterized by strong faulting is also described in this chapter. Then the study area with the seismic profiles is introduced.

Two measurement campaigns were carried out in 2010 and 2012 in the southern part of the Danish island Bornholm and different seismic sources were used on a total of three crossing profiles. Close to the seismic lines, two scientific boreholes were located. One of the boreholes was drilled shortly before the seismic measurements were carried out and provided logging and sample information directly at the cross point of two of the seismic profiles. The lithostratigraphical interpretation of both boreholes gave a first idea about the expected underground structure.

The seismic data achieved with a weight drop source was analyzed using traveltime tomography. The method and the applied techniques are described in Chapter 3. Manually picked traveltimes of all of the three seismic profiles were inverted with the software **SIMUL** (Thurber, 1983; Evans et al., 1994; Eberhart-Phillips & Reyners, 1997) which is based on a damped least squares inversion and on ray-tracing. Resolution tests were carried out to prove the reliability of the final tomographic models. Therefore, checkerboard tests were applied, the spread value of the models was calculated and an imaging test for the resolution of a high velocity layer was performed. The final tomographic results clearly reveal the black shale layer with velocities around 3 km/s. In two of the three profiles, the black shale is partly or completely overlain by a limestone layer with higher velocities. The bottom of the black shale layer is imaged very consistently in all models. It forms the boundary to a sandstone layer with again higher velocities than the black shale. Finally, the two models of the profiles which were crossing one of the boreholes are compared to the sonic log information. Additionally, correlations between the total organic carbon content of samples from the borehole are brought in correlation to the seismic velocities. In Chapter 4, the surface wave inversion is described. It was not possible to extract any S-wave information from the weight drop data and, therefore, the Love waves contained in the SH vibroseis data of one profile were used to invert for a S-wave velocity model. Dispersion curves were determined by calculating the phase velocity spectrum and picking its maximum values. They were used for the inversion with the software **DINVER** (Wathelet, 2005, 2008), which is based on the neighbourhood algorithm (Sambridge, 1999). For each of the source locations of the vibroseis profile 1D S-wave velocity models were finally obtained. The high velocity limestone layer on top of the black shale is not imaged by the surface wave inversion. This phenomenon was also analyzed with a synthetic test model including a high velocity layer. All final 1D S-wave models are in good correlation and especially the bottom depth of the black shale layer is imaged very well. The S-wave velocity found for the black shale is around 2 km/s.

In Chapter 5, a short overview of the method of seismic interferometry is given. In addition to the active field experiments, a passive record of the ambient seismic noise was conducted along the profile where also the vibroseis experiment was carried out. The recorders were running for about one day and were also recording during the active weight

---

drop experiment at this profile. To extract the Green's function between station pairs, the signals of these two stations were crosscorrelated in a defined time window of one hour. The crosscorrelations for one station were then stacked for all time windows to determine the final interferograms. The signal-to-noise ratio of the final interferograms was improved by choosing only time windows for the stack, where the noise signals were appropriate. Unfortunately, the data quality was still insufficient for further investigation of the interferograms, which could be analyzed like usually derived seismograms. However, conclusions about the type and origin of the recorded noise signal were achieved and even P-wave signals were visible in the interferograms.

After the drilling of one of the scientific boreholes at the study location on Bornholm, black shale samples were provided for a laboratory analysis. The basic principles of ultrasonic measurements and their execution are described in Chapter 6. The measurements were carried out under different pressure and temperature conditions either with a P-wave or a S-wave transducer and with wave propagation parallel or perpendicular to the bedding of the sample. The P-wave velocity shows a high amount of more than 30% anisotropy, where the higher P-wave velocity is observable for wave propagation parallel to the bedding. In contrary, the measured S-wave velocity shows almost no anisotropy at all. The compressional to shear wave velocity ratio is found to be independent of pressure or temperature changes, whereas the individual velocities are significantly increasing or decreasing with increasing pressure or temperature. The anisotropy has a reverse behavior to the velocity showing decreasing values with pressure and increasing values with temperature.

All the individual methods of investigating the black shale on Bornholm are combined in Chapter 7. The joint interpretation reveals the  $v_P/v_S$  velocity ratio of the subsurface at one of the seismic profiles. With that information, the shale gas potential of the black shale formation can be estimated. The complementary character of the combined measurements is shown and all the different methods and results are brought together in the context of the thesis.





## 2 Topic of study

### 2.1 Black shales

Black shales are fine-grained sedimentary rocks (mudrocks) with a high content of organic matter. The dark color of black shales differentiates them from other mudrocks. The color is thereby influenced by the amount, type and maturity of the contained organic carbon (Arthur & Sageman, 1994). Weissert (1981) suggested the range of the organic carbon content (TOC) varying between 1 and 30 %, but higher values are also possible.

During the last decade, the interest in black shales increased because of their potential to act as a hydrocarbon source rock. The organic matter may have generated liquid or gaseous hydrocarbons which may have accumulated in reservoirs or be adsorbed in the black shale formation itself (Tourtelot, 1979). Black shales show a low carbonate content. Meyers and Mitterer (1986) pointed out, that the lack of carbonates additionally increases the organic carbon content and also the content of associated heavy metals. The Kupferschiefer of Permian age in Central Europe is an example of the enrichment of metals.

Black shales are found throughout the Earth's history and in all parts of the Earth. Thereby, they show a high regional variability in the content of organic matter and may therefore describe the evolutionary development of life on Earth (Woodring, 1954). Organic-rich sediments like black shales are deposited in an anaerobic marine environment with the abundance of oxygen. Primary controls for the accumulation of organic material are the sedimentation rate, the organic productivity and the amount of oxygen. Didyk et al. (1978) introduced three models of depositional environments under which organic material may be accumulated: the restricted circulation model (1), the open ocean model (2) and the continental shelf model (3).

(1) The restricted circulation model is a classical model describing the accumulation of organic material which is often used. The main approach of that model is that the oxygen content of the water column is not renewed by circulation. Therefore, organic material can be accumulated at the ocean bottom even if the organic productivity is small.

(2) In the open ocean model, the circulation is present but the sedimentation rates are so rapid, that there is not enough time for the complete oxidation of organic matter. Even if the environment is oxic, organic-rich sediments can be accumulated at the ocean bottom. The sediments will become anoxic a few millimeters below the surface of the sediments

because of bacterial decomposition.

(3) The continental shelf model is very similar to the open ocean model, but here the water column is much shallower. Due to the circulation, the oxygen content at the bottom is large. Nevertheless, the high sedimentation rate favors the accumulation of organic-rich sediments. A few millimeters beneath the surface, the sediments again will be anoxic because of bacterial processes.

Over the years, the accumulated organic material underwent the process of diagenesis, where temperature and pressure transformed the sediments into black shale. C. D. Curtis (1977) in detail described the stages of black shale diagenesis.

## 2.2 Seismic measurements

Our seismic measurements were carried out in the years 2010 and 2012 on the Danish island Bornholm. The island is located in the Baltic Sea north-east of Germany (Figure 2.1). The study area was located in the southern part of Bornholm because the particularly interesting Palaeozoic Alum Shale black shale Formation is present at this location (see Section 2.3).

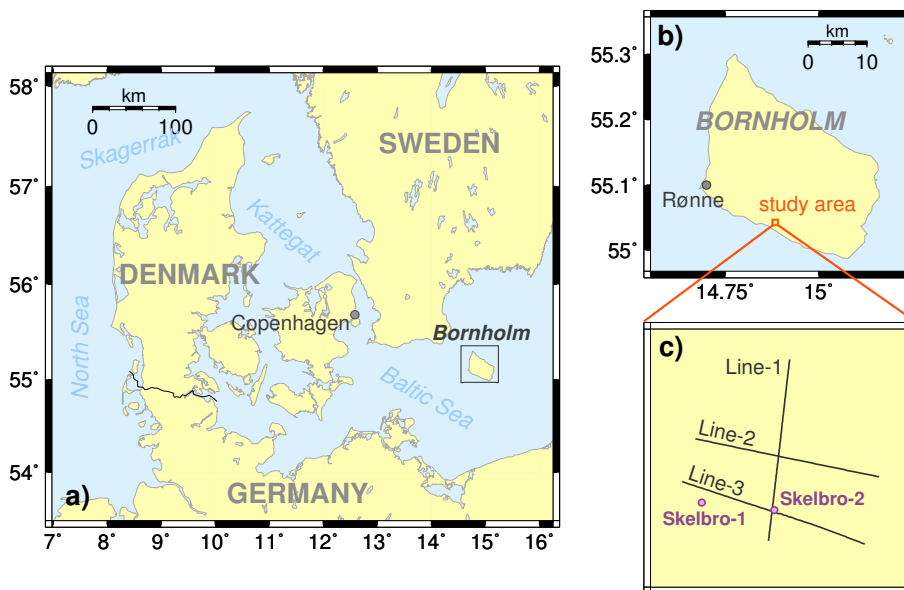


**Figure 2.1:** (a) Map of Denmark including the island Bornholm. (b) Detail of the island Bornholm with the study area. (c) Location of the acquired seismic profiles and the borehole locations Skelbro-1 and Skelbro-2.

In October 2010, the first two seismic profiles (Line-1 and Line-2 in Figure 2.1c) were acquired near the well locations Skelbro-1 and Skelbro-2 (see Section 2.4) with the aim to characterize the black shale formation seismically and to estimate its local extension. Both profiles were located as near as possible to the borehole locations and were arranged

perpendicular to each other to estimate the three-dimensional extension of the subsurface structures. The profile Line-1 was N-S directed and 690 m long. It crossed a main road which caused a lack of seismic information in this part of the profile. The perpendicular profile (Line-2), which was W-E directed, was 720 m long and could not be arranged crossing a well location due to the mentioned road and a small lake. For both profiles, the receiver spacing was 2 m and the source spacing was 12 m. All receivers were active for every shot. Therefore, a total of 58 shots each with 340 receivers for Line-1 and 61 shots each with 359 receivers for Line-2 were recorded. Single vertical component geophones running with the GEODE system (Geometrics Inc.) were used. They had a natural frequency of 10 Hz. Additionally, up to 119 stand-alone digital data recorders (GFZ-Cubes) with 4.5 Hz vertical component geophones were attached to reach the full extend of each profile. A Propelled Energy Generator (PEG-40 by R. T. Clark Companies, Inc.) with a weight drop of 40 kg was used as a source. It was dropped onto a striking plate ten times at every shot location to reduce noise in the data later on by vertical stacking. The main frequency of the source was 35 - 40 Hz and the sampling rate was 1 ms.

In June 2012 an additional seismic measurement took place at the Skelbro location. Along a cycle track crossing the Skelbro-2 borehole location, a combination of weight drop and vibroseis experiment was carried out (Line-3 in Figure 2.1c). First, an additional refraction profile was arranged with the same acquisition parameters as for the 2010 experiment. Again, the PEG-40 weight drop source was used at a total of 61 shot locations and the two different geophone types were spread every 2 m over a full profile length of 720 m. The vibroseis experiment was also conducted at the cycle track between the distances of 120 and 600 m along Line-3. The minivibrator called ELViS (**E**lectrodynamic-**V**ibrator **S**ystem by Geosym) was used as the source. It could be rearranged to be operated either as P-wave or SH-wave source. A 10 s long sweep was used with a frequency range of 20 - 160 Hz for either of the sources. The first vibrator position was 120 m to the east of the first source point of the weight drop experiment at the same profile. The first and last six sources had a spacing of 12 m and the shots in between were spread every 6 m. Two profiles were carried out, one with P-wave arrangement and the other adjusted to SH-wave recordings, both achieved with a roll-along configuration: the full profile length of 480 m was reached with individual spreads of 240 m length, leaving an overlap of 120 m (Figure 2.2). P-wave and S-wave geophones of the Geode system were spread every meter. Additionally, stand-alone digital data recorders (GFZ-Cubes) were arranged between the Geode receivers, so that in parts of the profile the receiver distance decreased to 0.5 m (light blue areas in Figure 2.2). For the P-wave vibroseis experiment (Figure 2.2 top), all 205 GFZ-Cubes could be used to decrease the receiver spacing and to record the vertical component of the wave field. Five individual spreads were arranged to reach the full profile

length of the vibroseis experiment. The bottom plot of Figure 2.2 shows the configuration of the SH vibroseis experiment with eight individual spreads. The GFZ-Cubes of the SH experiment were arranged to concentrate the receivers in the near-field distance of the sources. Here, only the 85 three-component GFZ-Cubes could be used, because only the horizontal N-S component of the SH wave field, which was transmitted in N-S direction, was needed.

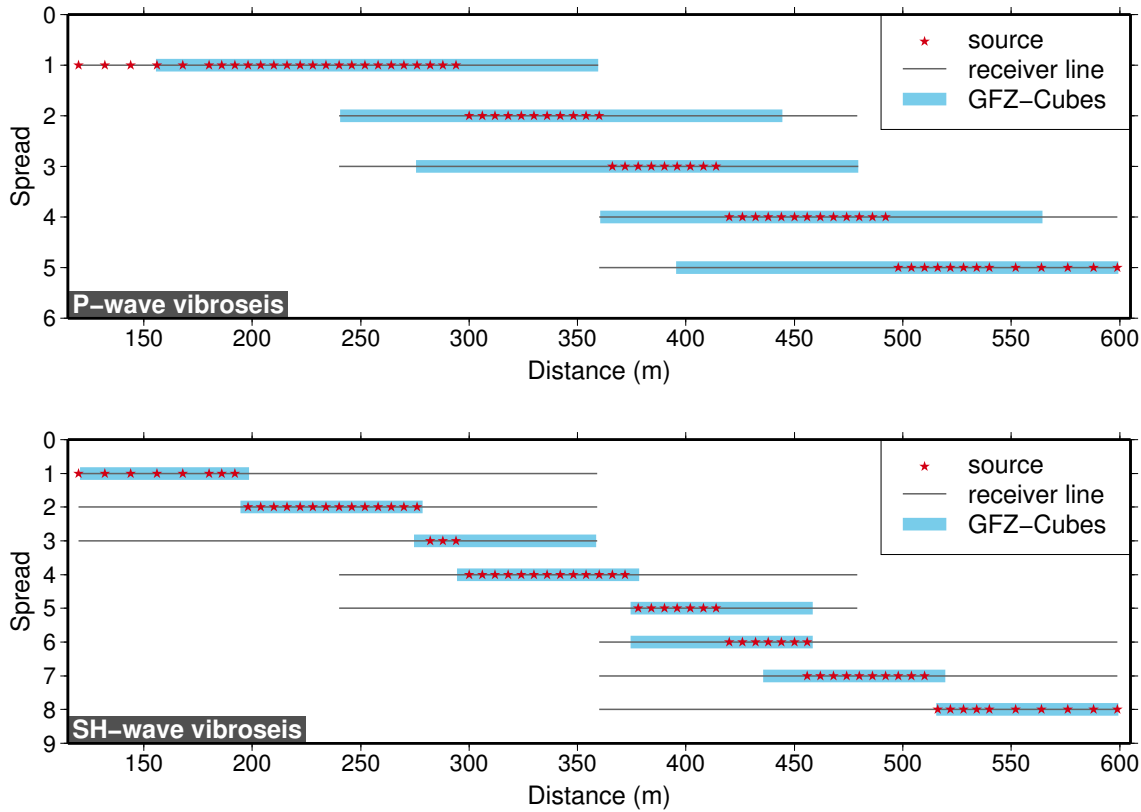


**Figure 2.2:** Configuration of the vibroseis experiments. Top: The P-wave vibroseis experiment with five individual spreads. Colored in light blue are the parts of the spreads where the GFZ-Cubes were arranged. Bottom: The S-wave vibroseis experiment, where the 71 sources were distributed over eight individual spreads.

## 2.3 Geology of Bornholm

Bornholm is a basement horst block located within the Fennoscandian Border Zone (Vejbæk et al., 1994; Graversen, 2009). The Fennoscandian Border Zone is a strongly block-faulted zone (Sorgenfrei & Buch, 1964) which separates the Fennoscandian Shield to the north-east from the Danish Basin to the west and south-west (Michelsen & Nielsen, 1993). The Fennoscandian Border Zone is divided into two zones: the Sorgenfrei-Tornquist Zone to the west and the Skagerrak-Kattegat Platform to the east. South of Bornholm,

the Sorgenfrei-Tornquist Zone passes over into the Teisseyre-Tornquist Zone to the east with the Rønne Graben separating both zones. Liboriussen et al. (1987) proposed that the Fennoscandian Border Zone has been tectonically active from the Early Palaeozoic up to recent times. The Sorgenfrei-Tornquist Zone underwent an uplift of 1700 - 2000 m during the inversion tectonics of the Late Cretaceous to Early Tertiary and the uplift of Fennoscandia in the Late Tertiary.

The Danish island Bornholm is characterized by a mosaic of fault blocks (Figure 2.3). The faulting took place from Precambrian to Tertiary times. In the northern parts of the island, Precambrian granites and gneisses are present, whereas the southern part is dominated by Palaeozoic and Mesozoic sediments. The Palaeozoic rocks are composed of Lower Cambrian sandstone and black to gray shales of Middle Cambrian to Silurian age. Primary bioclastic carbonate beds occur as a minor component in the succession (Nielsen & Schovsbo, 2006; Stouge & Nielsen, 2003). The Cambrian sand and siltstones on Bornholm can be divided into the Nexø, the Hardeberga and the Læså Formations (Nielsen & Schovsbo, 2006). The Nexø Formation is a reddish colored slightly arkosic sandstone and the Hardeberga Formation shows well-sorted, strongly cemented quartzite sandstones including subordinate silt- and mudstone layers. The Læså Formation is composed of greenish gray siltstone with a variable amount of glauconite. At several levels, phosphorite nodules are present. In the upper part of the formation, sandstone layers are common. The regionally widespread Rispebjerg Sandstone is the top member of the Læså Formation.

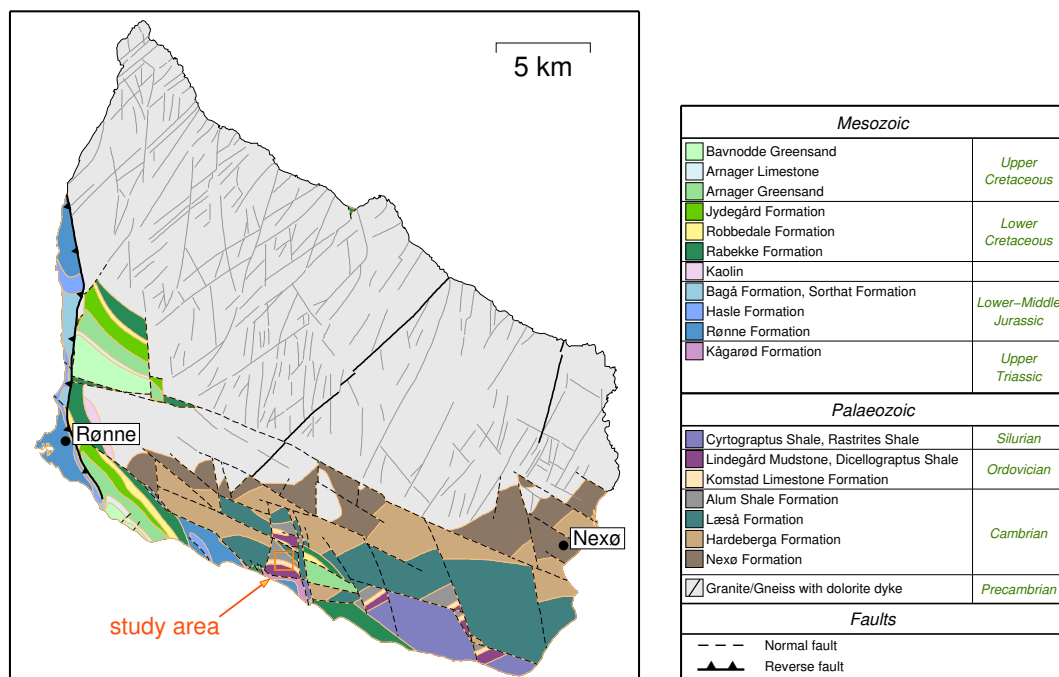


**Figure 2.3:** Geology of Bornholm (after Graversen, 2009).

The Cambrian to Lower Ordovician Alum Shale Formation consists of dark organic rich mudstone with abundant disseminated pyrite. Schovsbo (2002) distinguished two forms of the Alum Shale lithology: (1) The *outer shelf type* has a small proportion of diagenetic carbonate beds and is present on Bornholm and in southern Sweden (Scania). (2) The *inner shelf type* shows the Alum Shale with higher proportions of non-shale beds including primary carbonates, conglomerates and diagenetic carbonate concretions. That type is present in the south-central parts of Sweden and on Öland. In the lower parts of the Alum Shale Formation thin layers of Exsulans and Andrarum Limestones (both < 1 m thick) occur (see Figure 2.4). These marker beds are primary bioclastic limestones and represent important stratigraphical horizons that are particularly easy to recognize on the gamma ray logs due to their low gamma ray response.

The Ordovician Shales and the limestone formations on Bornholm above the Alum Shale are composed of the Komstad Limestone Formation, the Dichellograptus Shale and the Lindegård Formation (Stouge & Nielsen, 2003). The Komstad Limestone is a thin bedded cold-water bioclastic carbonate unit which contains a variable amount of clay, phosphorite and glauconite. The Dichellograptus Shale is a gray to dark mudstone. The lower part contains numerous bentonite beds including the up to one meter thick Kinnekulle Bentonite. The top of the formation, corresponding to the Fjäckå Shale of south-central Sweden (Jaanusson, 1963), is developed as a black mudstone which contains up to 4% TOC in Scania and on Bornholm.

The Lower Palaeozoic shales were buried to a depth of 3 - 4 km in the Late Silurian to Early Devonian during the Caledonian orogeny (Buchardt et al., 1986; Jensenius, 1987; Vejbæk et al., 1994). Thermal maturation of the organic carbon to oil and dry gas occurred during that interval (Buchardt et al., 1986; Jensenius, 1987). The Alum Shale Formation on Bornholm is directly overlain by the Middle Ordovician Komstad Limestone. Compared to the more complete stratigraphy in Scania, the uppermost part of the Alum Shale (Ceratomyge Shale), the Bjørkåsholmen Formation and the Tøyen Shale are missing on Bornholm (Schovsbo, 2011). That is an indication for a slight uplift and adjustment of the plate margins (Stouge & Nielsen, 2003).

## 2.4 Integration of borehole information

As mentioned in the description of the seismic measurements (Section 2.2), two scientific boreholes were located close to the seismic profiles (see Figure 2.1c), namely Skelbro-1 (Pedersen, 1989) and Skelbro-2 (Schovsbo et al., 2011). The results of core and logging analyses of the boreholes which are mostly related to this work are presented in the following.

## Skelbro-1

The Skelbro-1 borehole was drilled in May 1984 with the aim of extracting fresh core material for the analysis of the structure, sediment composition and diagenesis of the Lower Palaeozoic shales on Bornholm (Pedersen, 1989). Later on, the cores have also been studied according to their stratigraphy (Pedersen & Klitten, 1990; Koren & Bjerreskov, 1997), their geochemistry (Buchardt et al., 1986), their maturity (Buchardt & Lewan, 1990) and fluid inclusions (Jensenius, 1987). The only logging that was carried out in the Skelbro-1 borehole was a gamma ray log; it is reported by Pedersen and Klitten (1990). A simplified stratigraphical profile of the Skelbro-1 well can be seen in the left panel of Figure 2.4.

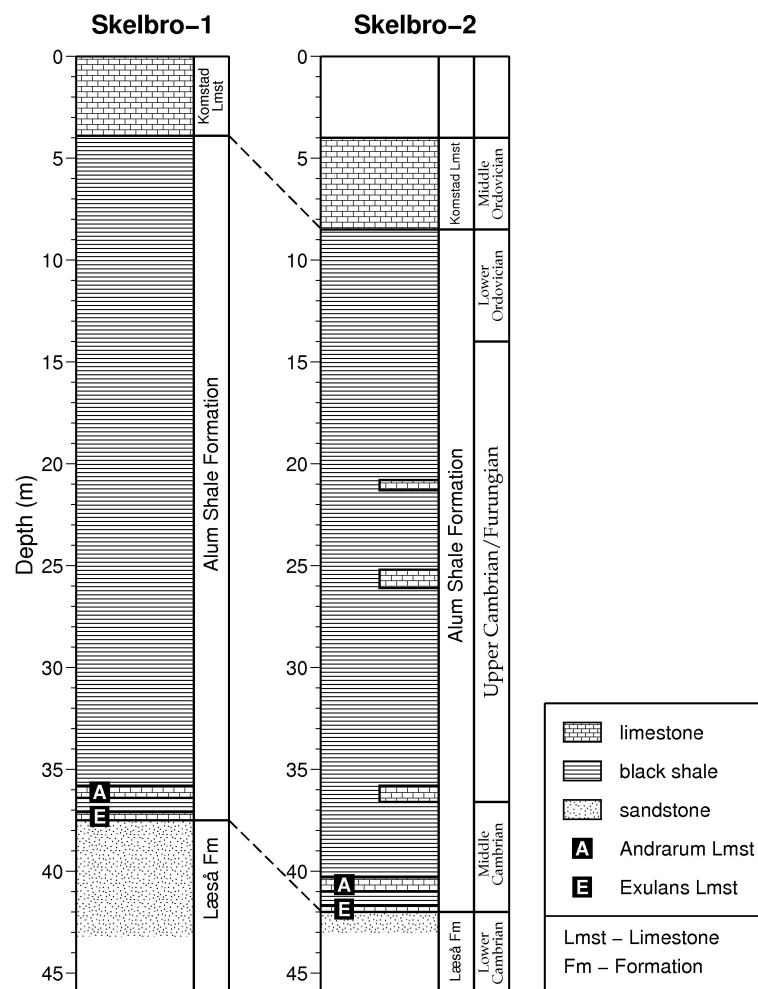


**Figure 2.4:** Lithostratigraphy of the boreholes Skelbro-1 (left panel, simplified after Pedersen, 1989) and Skelbro-2 (right panel, after Schovsbo et al., 2011 and Schovsbo, *pers. comm.*). The elevation at Skelbro-1 and Skelbro-2 are 35 m and 39.5 m, respectively. The difference of 4.5 m in the depth levels of both stratigraphies is, therefore, only due to the difference in elevation.

The first 3.9 m of the Skelbro-1 borehole were drilled through the Komstad Limestone Formation (Figure 2.4 left), after which the 33.6 m thick Alum Shale Formation follows. Included in the Alum Shale are the Middle Cambrian Andrarum Limestone and the Exsulans Limestone. These limestone beds are important regional markers (Nielsen & Schovsbo, 2006). After the base of the Alum Shale was reached at a depth of 37.5 m below ground, the borehole was stopped in the Læså Formation at a depth of 43.2 m. The top 3.2 m of the Læså Formation constitute the Rispebjerg Sandstone Member.

## Skelbro-2

The Skelbro-2 well was drilled in August 2010 about 270 m east of Skelbro-1 with the purpose of extracting new core material and improving the stratigraphy described by Pedersen (1989). The stratigraphical profile of Skelbro-2 is plotted in the right part of Figure 2.4 and was first reported by Schovsbo et al. (2011). Here, the Komstad Limestone has a thickness of 4 m and reaches down to a depth of 8.5 m. Then, the Alum Shale follows with a thickness of 33.5 m, again showing the Andrarum and Exsulans limestone marker beds. Included in the Alum Shale Formation are characteristic beds and nodules of diagenetic carbonates. The black shale layer is divided into three different units which mark the different depositional ages of this layer. The uppermost unit is the Lower Ordovician part of the Alum Shale. It is followed by the Upper Cambrian or Furungian part and, finally, by the Middle Cambrian part of the black shale layer. The base of the Alum Shale at Skelbro-2 is 42 m beneath the surface and the drilling was stopped in the Læså Formation at a depth of 42.9 m.

Both boreholes Skelbro-1 and Skelbro-2 show an almost identical stratigraphy. The difference in the depths of the formations is only caused by the different elevations of the borehole positions and, therefore, different reference heights. The elevation at Skelbro-1 and Skelbro-2 are 35 m and 39.5 m above sealevel, respectively. The difference in elevation of 4.5 m is exactly the difference value found in both stratigraphies.

One month after the drilling of Skelbro-2, in September 2010 borehole logging was carried out by the Geological Survey of Denmark and Greenland (GEUS). Due to technical problems, the sonic log could not be obtained in September, but it was then repeated in November 2010. All logs are summarized in Figure 2.5. The sonic log (Figure 2.5, fourth panel from left) was used for a comparison with the results of the travelttime tomography (Section 3.3.2). Schovsbo (2011) found a very strong inverse correlation between the sonic log velocities and the content of organic carbon (TOC) of the Alum Shale.

The Alum Shale is characterized by higher gamma ray values than the other units (Figure 2.5, first panel from left). The gamma ray responses of the Alum Shale are caused by the thorium content of the clays, potassium feldspar and by the uranium content



(Baumann-Wilke et al., 2012). Schovsbo (2002) showed, that the uranium content of the black shale formation is related to the TOC content due to the joint precipitation of uranium from seawater and the organic matter. Therefore, the variation in gamma ray value is also an indication of the TOC content. The fluctuations found in the gamma ray response are caused by the diagenetic carbonate concretions with lower gamma values. It can be seen, that at a depth of about 30 m the gamma ray value decreases. That indicates the transition from the Furungian to the Upper Cambrian Alum Shale.

The core samples of the Alum Shale from the Skelbro-2 well have TOC contents of 4 - 14 % (Schovsbo, 2011), and Buchardt et al. (1986) reported an average TOC value of 9 % for the Skelbro-1 Alum Shale cores. Compared to Mesozoic and younger marine sediments, the TOC content of the Alum Shale is very high (Demaison & Moore, 1980). The preservation of the organic material is a strong indication of an anoxic depositional environment. The Alum Shale is assumed to be a marine deposit because no indication of continental vegetation is found in the preserved organic matter (Buchardt et al., 1986).

The pyrite content was found to be 11 % (Pedersen, 1989), where the most of it is finely disseminated. The dominant clay mineral of the Alum Shale is illite and neither kaolinite nor chlorite minerals occur in this formation (Schovsbo, 2011).

The Alum Shale on Bornholm has a very high thermal maturity (Buchardt & Nielsen, 1985; Buchardt et al., 1986, 1997, 1998; Buchardt & Lewan, 1990; Jensenius, 1987). A maturity map of the Alum Shale in Denmark and Scania has been presented by Buchardt et al. (1997). The Alum Shale does not contain terrestrially derived particles, therefore, direct vitrinite reflectance could not be used to obtain the thermal maturation of the shale. But the unit contains vitrinite-like particles probably of marine origin. Buchardt and Lewan (1990) showed that these particles behave in a similar manner as the true vitrinite. The reflectance of vitrinite-like particles has been widely used as a thermal marker in the shale. Core samples of the Skelbro-1 well have average vitrinite reflectance values of  $R_o = 2.34\%$  (Buchardt & Lewan, 1990) and the Skelbro-2 cores show almost similar average values of  $R_o = 2.36\%$  (Ghanizadeh, *pers. comm.*). That means, the Alum Shale on Bornholm is in the post-mature rank with regard to oil generation and, therefore, favorable for shale gas (Schovsbo et al., 2011).

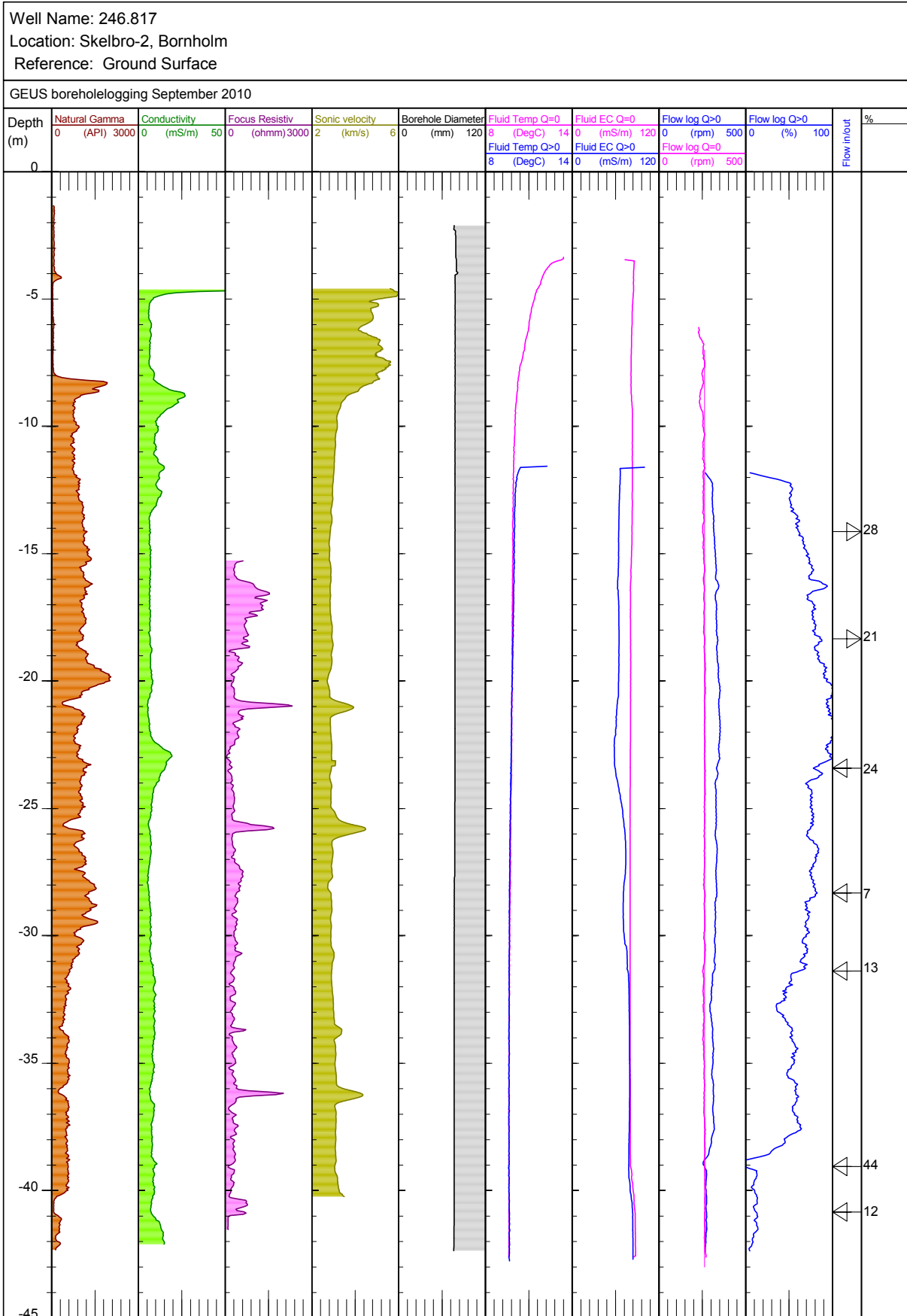


Figure 2.5: Logging report of the borehole Skelbro-2. © GEUS

---

## 3 Traveltime tomography

### 3.1 Introduction

Seismic tomography is a method to map the earth's interior using seismic waves. The linguistic origin of tomography is the Greek word *tomos* meaning *slice*. It was first used in medicine to image the density distribution of a human body with x-rays (W. H. K. Lee & Pereya, 1993). The method was later appropriated by seismologists to map the internal structure of the earth using seismic waves. Today, seismic tomography is one of the most popular techniques of imaging the earth's subsurface structure (Rawlinson & Sambridge, 2003). Most commonly, the traveltimes of body waves between source and receiver are used for the seismic tomography. The reason is, that traveltimes can be easily extracted from the seismograms and the relationship between traveltime and wave velocity is simple. The simplicity and the robustness of the method make traveltime tomography one of the most commonly used seismic imaging techniques.

In this chapter the application of the traveltime tomography method to the weight drop field data is shown. The traveltime tomography was done with the software **SIMUL** developed by Thurber (1983) and enhanced especially by Evans et al. (1994) and Eberhart-Phillips and Reyners (1997). That program is based on a damped least squares inversion and ray-tracing using the pseudo-bending method. Therefore, the description of these techniques is considered in more detail here. The basic principles of traveltime tomography are briefly summarized without going to much into detail. For further interest the reader is referred to the theory described by, e. g., Thurber (1983); Menke (1989); Iyer and Hirahara (1993) or Rawlinson and Sambridge (2003).

The traveltime tomography mainly consists of three different steps: (1) First, a velocity model has to be chosen as an initial model. That is a necessary condition for the inversion routine. That model must then be parameterized to be used in the discrete inversion. (2) The second step is to calculate appropriate ray paths between the given source and receiver position. When the traveltimes of the calculated ray paths properly fit the observed data, the inversion (3) is carried out and the initial velocity model is updated along the ray paths using the damped least squares method.

The recorded field data was first processed using the software **ProMAX®**. Vertical stacking

was used to restrain the unwanted noise caused by traffic and the rebound of the striking plate. Traveltimes were picked manually and the picking uncertainty was calculated with two different approaches. A very important step was to find an initial velocity model for the traveltime tomography. That was done with `SIMUL` and the correct source and receiver geometry, but only for a 1D gradient model. A simple model with increasing velocity with depth was used, because Eberhart-Phillips (1990) showed, that a simple initial model gave the best results. With that initial model, the 2D traveltime tomography was then carried out using the graded inversion strategy described by Evans et al. (1994). That strategy has the advantage of minimizing inversion artifacts by stepwise going from a coarse to a fine model.

The final tomography models, derived after a total of at most 15 iterations, were then fully described by a resolution analysis including the checkerboard test, the calculation of the spread value and an imaging test for high velocity layers. The Alum Shale black shale layer was found with a thickness of approximately 30 m dipping southward. In the southern part of the study area, the Alum Shale is overlain by the Komstad Limestone Formation with a thickness of only 4 m. Below the Alum Shale, the Læså Sandstone Formation is present in all seismic profiles. The comparison with the borehole sonic logs of the Skelbro-2 well gave a good correlation with the obtained tomography models. The TOC content, which is an important parameter for the localization of oil or gas, might be calculated with an empirical relationship that could be derived from sonic logging and sample measurements.

### 3.1.1 Mathematical principles of traveltime tomography

If we assume a continuous velocity medium  $v(\mathbf{x})$ , the traveltime of a ray on a certain ray path  $L$  is given by the line integral

$$t = \int_{L(v)} \frac{1}{v(\mathbf{x})} dl, \quad (3.1)$$

where  $dl$  is a path element. The traveltime can also be calculated by integrating the weighted slowness  $s(\mathbf{x}) = 1/v(\mathbf{x})$  along the ray path. If we now assume a model which is discretized into  $N$  slowness cells, where each  $j$ th cell has an unknown slowness of  $s_j$ , the traveltime integral can be reduced to a summation of the form:

$$t_i = \sum_j l_{ij} s_j, \quad (3.2)$$

where  $l_{ij}$  is the segment length of the  $i$ th ray in the  $j$ th cell. Here, the slowness is weighted by the segment length of the ray. The summation can then be recast to matrix-vector notation as

$$\mathbf{t}' = \mathbf{L}'\mathbf{s}', \quad (3.3)$$

where  $\mathbf{L}'$  is the  $M \times N$  ray path segment matrix with elements  $l'_{ij}$ ,  $M$  is the number of rays,  $N$  is the number of constant slowness cells and  $\mathbf{s}'$  is the actual slowness model.

For an initial slowness model  $\mathbf{s}$ , we have the traveltimes  $\mathbf{t} = \mathbf{L}\mathbf{s}$ . Then we can formulate a perturbed set of traveltime equations:

$$\mathbf{t} - \mathbf{t}' = \mathbf{L}\mathbf{s} - \mathbf{L}'\mathbf{s}', \quad (3.4)$$

with the ray path matrix  $\mathbf{L}$  which is associated with the initial slowness model. The ray path segment matrix  $\mathbf{L}'$  can be approximated by  $\mathbf{L}$  to the second order in the perturbation parameter  $\delta\mathbf{s} = \mathbf{s} - \mathbf{s}'$ , that means  $\mathbf{L}' = \mathbf{L} + O(\delta\mathbf{s}^2)$ . Then Equation 3.4 can be rewritten as

$$\delta\mathbf{t} = \mathbf{L}\delta\mathbf{s}. \quad (3.5)$$

The traveltime tomography relationship between the observed data and the model parameters is nonlinear because the ray path depends on the slowness structure. Under the assumption that the segment lengths do not change when the slowness model is slightly perturbed, the relationship between data and model can be linearized using Equation 3.5. If we now define  $\mathbf{d} = \delta\mathbf{t}$  as the traveltime residuals and  $\mathbf{m} = \delta\mathbf{s}$  as slowness perturbation, the inverse problem can be written as

$$\mathbf{d} = \mathbf{L}\mathbf{m}. \quad (3.6)$$

The aim of the traveltime tomography is to solve the discrete inversion problem of Equation 3.6. Normally, we have many more equations than unknowns. Therefore, the problem can be solved by minimizing the sum of the squared errors:

$$(\mathbf{L}\mathbf{m} - \mathbf{d})^T (\mathbf{L}\mathbf{m} - \mathbf{d}) + \lambda^2 \mathbf{m}^T \mathbf{m} \rightarrow \min. \quad (3.7)$$

The Levenberg-Marquardt damped least squares solution of Equation 3.6 is then

$$\mathbf{m} = (\mathbf{L}^T \mathbf{L} + \lambda^2 \mathbf{I})^{-1} \mathbf{L}^T \mathbf{d}, \quad (3.8)$$

where  $\lambda$  is the damping parameter and  $\mathbf{I}$  is a  $N \times N$  identity matrix.

The resolution matrix  $\mathbf{R}$  is defined after Menke (1989) as

$$\mathbf{R} = \mathbf{L}^{-g} \mathbf{L} = (\mathbf{L}^T \mathbf{L} + \lambda^2 \mathbf{I})^{-1} \mathbf{L}^T \mathbf{L}, \quad (3.9)$$

using the generalized inverse  $\mathbf{L}^{-g} = (\mathbf{L}^T \mathbf{L} + \lambda^2 \mathbf{I})^{-1} \mathbf{L}^T$  of the damped least squares solution. If the resolution matrix equals the identity matrix  $\mathbf{I}$ , each model parameter is uniquely determined. Otherwise, the estimates of the model parameters are weighted averages of the true model parameters.

If the traveltime data are uncorrelated all having an equal variance  $\sigma^2$ , the model covariance matrix can be calculated with

$$\mathbf{C}_m = \sigma^2 \mathbf{L}^{-g} \mathbf{L}^{-gT}. \quad (3.10)$$

### 3.1.2 Model parametrization

The traveltime between a seismic source and the receiver depends on the velocity structure through which the wave is traveling. It is especially important to give an appropriate velocity model for the calculation of the ray paths (Section 3.1.3). For the discrete traveltime tomography, the velocity structure has to be parameterized (Figure 3.1). Therefore, the velocity model is separated into blocks, which are surrounding the grid point  $(x, y, z)$  with the given velocity (Thurber, 1983). The velocity at any point within that block is given by the trilinear interpolation function:

$$v(x, y, z) = \sum_{i=1}^2 \sum_{j=1}^2 \sum_{k=1}^2 V(x_i, y_j, z_k) \left(1 - \left|\frac{x - x_i}{x_2 - x_1}\right|\right) \left(1 - \left|\frac{y - y_j}{y_2 - y_1}\right|\right) \left(1 - \left|\frac{z - z_k}{z_2 - z_1}\right|\right), \quad (3.11)$$

where  $V(x_i, y_j, z_k)$  are the velocity values at the eight surrounding grid points of  $(x, y, z)$ .

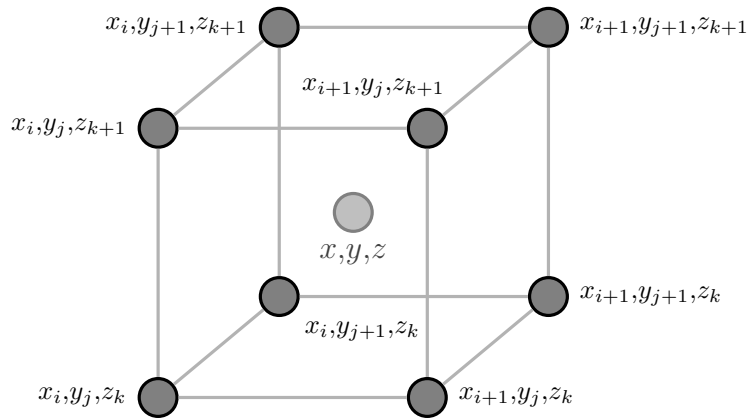


**Figure 3.1:** Definition of velocity structure with grid points after Thurber (1983). The rectangular velocity volume around the given point  $(x, y, z)$  is defined by a trilinear interpolation function.

The model definition of Equation 3.11 ensures that the velocity field will be continuous throughout the model volume, although the velocity gradient from one block to the next block might be discontinuous. That model parametrization technique is often used in the tomography of seismic waves, especially by Eberhart-Phillips (1986) and Thurber and Eberhart-Phillips (1999).

### 3.1.3 Ray-tracing

Traveltime tomography is a ray-based method. Therefore, it is necessary to calculate an appropriate ray path between given source and receiver points. That can be done mainly in two different ways, either with the shooting method or the bending method

(Rawlinson & Sambridge, 2003).

With the shooting method, as the name denotes, rays are shot from the source position through a defined velocity model. The ray path is then modified till the receiver position is reached. The associated two-point boundary value problem cannot be solved directly (Julian & Gubbins, 1977), but can either be transformed in a system of first-order differential equations (Sambridge & Kennett, 1990) or can approximately be solved by shooting a fan of rays from the source through the model and stepwise converging to the receiver position (e.g., Blundell, 1993).

The traveltome tomography software described here uses the bending method, therefore, it is explained in more detail here. The bending method was first described by Julian and Gubbins (1977). It is a technique where an initial ray arbitrarily connects the source and receiver. The shape of the ray is then modified till Fermat's principle is satisfied.

The ray path can be described parametrically as  $\mathbf{x} = \mathbf{x}(q)$ . Then Equation 3.1 can be written as:

$$t = \int_{q_S}^{q_R} sF dq, \quad (3.12)$$

where  $s$  is the slowness and  $q$  can be written as  $q = l/L$ , where  $L$  is the total length of the ray path between source and receiver and  $0 \leq l \leq L$ .  $F$  is defined as follows:

$$F = \frac{dl}{dq} = \sqrt{\dot{x}^2 + \dot{y}^2 + \dot{z}^2}. \quad (3.13)$$

The differentials  $\dot{x}$ ,  $\dot{y}$  and  $\dot{z}$  are taken with respect to  $q$ . That formulation can then be assigned to the Euler-Lagrange equations (Julian & Gubbins, 1977):

$$\begin{aligned} \frac{d}{dq} \frac{\partial}{\partial \dot{x}}(sF) &= \frac{\partial}{\partial x}(sF) \\ \frac{d}{dq} \frac{\partial}{\partial \dot{y}}(sF) &= \frac{\partial}{\partial y}(sF) \\ \frac{\partial F}{\partial q} &= 0. \end{aligned} \quad (3.14)$$

At the starting and end point of the ray, the source position  $\mathbf{x}_S$  and receiver position  $\mathbf{x}_R$  are given. Therefore, two boundary conditions can be defined as  $\mathbf{x}(0) = \mathbf{x}_S$  and  $\mathbf{x}(1) = \mathbf{x}_R$ . Equations 3.14 are non-linear and cannot be solved directly.

A fast method to estimate the ray path is the pseudo-bending technique developed by Um and Thurber (1987) which is based on the approximate computation of path perturbations. An initial ray path is defined by three points which are linearly interpolated. The end points remain fixed (source and receiver) and the center point is then iteratively perturbed using a geometric interpretation of the ray equations till the traveltome converges within a

specified limit. The number of the path segments is then doubled and a new traveltime is calculated along the new path segments. The perturbation scheme is repeated, considering three points at a time beginning from both end points simultaneously. That procedure is repeated iteratively until the traveltime of the entire ray path converges. The pseudo-bending method by Um and Thurber (1987) is schematically described in Figure 3.2.

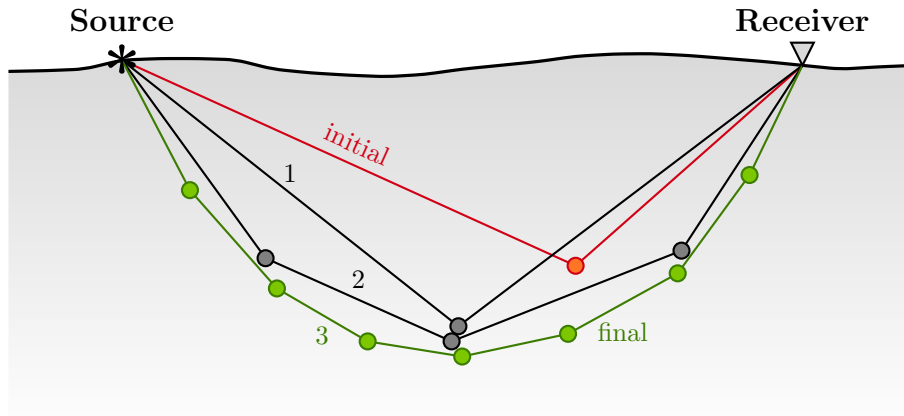


**Figure 3.2:** The pseudo-bending method of Um and Thurber (1987) where an initial three-point ray path is perturbed and successively halved. Sketch after Rawlinson and Sambridge (2003).

Another possible method of finding an accurate ray path is the approximate ray-tracing (Thurber & Ellsworth, 1980). When the velocity in a region close to source and receiver is laterally averaged, a 1D ray-tracer can be used to find the minimum time-path. That estimation of a ray path can be used as an initial path for the bending method. Thurber (1983) developed a variation of that technique, where a large number of circular arcs with different curvature are defined, which are joining source and receiver. Then the traveltimes along the arcs are calculated within a given velocity model and the arc with the minimum traveltime is chosen as an approximation for the first-arrival ray. For ray paths with moderate length ( $\leq 40$  km), that assumption is found reasonable (Eberhart-Phillips, 1986).

For smooth velocity structures, the bending method is more efficient whereas the shooting method is preferred when interfaces and strong velocity gradients occur (Červený, 1993). Nevertheless, due to its computational effectiveness, the bending method is preferred in the traveltime tomography program used here.



## 3.2 Processing and inversion

### 3.2.1 Data processing and traveltimes picking

For the traveltimes tomography, data which were acquired with the weight drop were used (Section 2.2). Examples of the seismic data are shown in Figure 3.3. The data quality is good but the influence of noise is visible, particularly for larger offsets. The main causes of the noise were the heavy wind and the traffic of the main road along Line-3. The processing of the seismic data was done with ProMAX®. Two types of geophones with different natural frequency were used. To equalize seismic traces of the different geophone types, a restitution filter was applied (Astiz et al., 1991). Then, vertical stacking was used to improve the data quality. Therefore, all ten shots at every shot position were stacked.

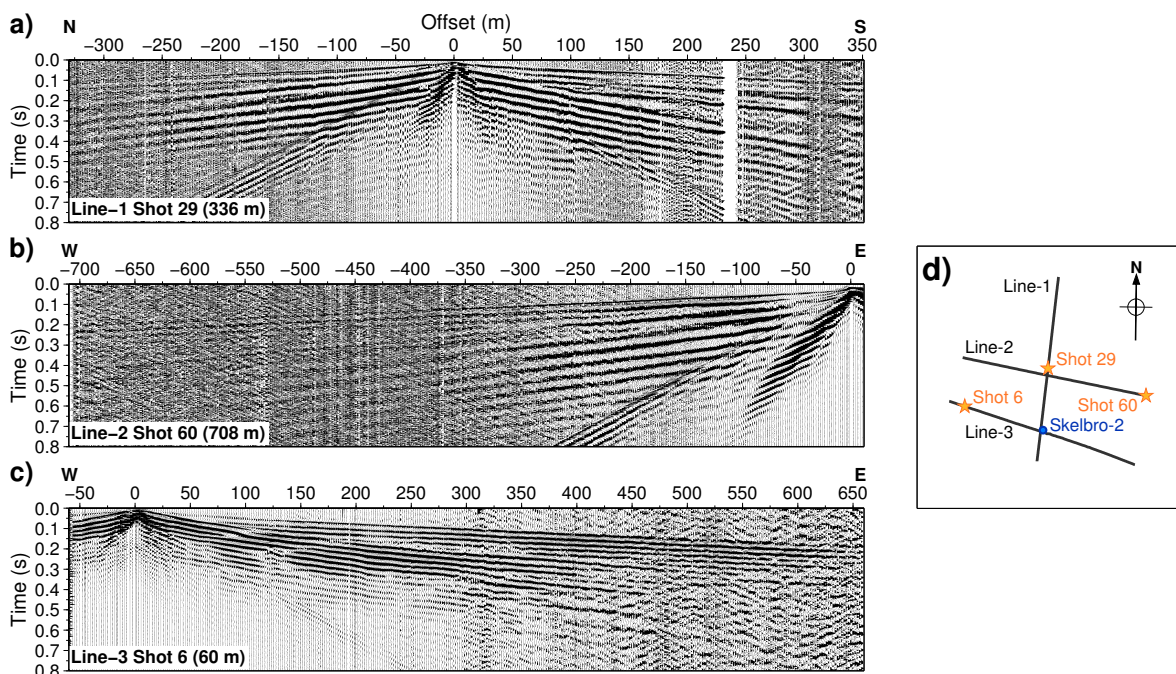


**Figure 3.3:** Examples of the raw data after vertical stacking. (a) Shot 29 of Line-1. (b) Shot 60 of Line-2. (c) Shot 6 of Line-3. (d) Overview of the locations of all profiles and the positions of the plotted shots.

### Improvement by vertical stacking

Noise is a main problem when working with seismic data and much effort is made to restrain such noise. One method to increase the signal-to-noise ratio is vertical stacking, where datasets with the same geometry are summed. Here, all ten shots that were done at one shot location were stacked using a diversity stack (Rashed & Nakagawa, 2006). The diversity stack for vertical stacking is most efficient, when the noise in one seismogram is uncorrelated with the noise in another seismogram of the same shot position. That is

especially the case for high impulsive noise like traffic. When the vertical stack has been applied to the data, only one seismogram at every shot location remained. A diversity stack with a window length of  $\Delta T = 100$  ms was used. For each time window, the traces were scaled by the inverse of their average power  $E$ . The scaling factor  $D$  was calculated with:

$$D = \frac{C}{E}, \quad (3.15)$$

where  $C$  is a constant, for which the value of  $C = 1$  was chosen. The energy of each time window was calculated as follows:

$$E = \sum_{\Delta T} a_i^2, \quad (3.16)$$

where  $a_i$  is either the amplitude or the power of the time window and  $\Delta T$  is the length of the time gate.

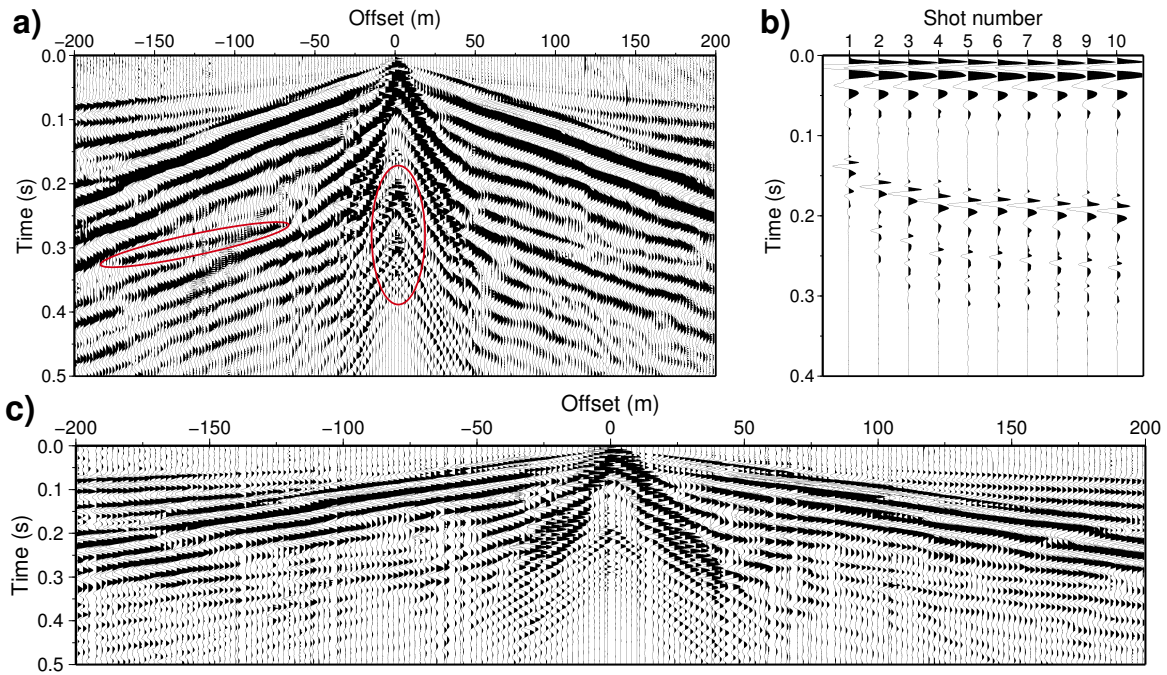


**Figure 3.4:** Effect of the rebound of the striking plate when operating the weight drop on an asphalt way. (a) Additional arrivals in the seismogram of a single shot marked by the red ellipses. (b) Moving of the "rebound arrivals" for the zero-offset traces of all ten shots at one shot location. While the first arrival time remains constant, the arrival time of the striker plate noise increases with increasing shot number. (c) The vertically stacked data of the shots shown in (a) and (b). The energy of the noise signals is minimized and the data quality has been improved.

The improvement of the vertical stack can be seen in Figure 3.4, where the noise of the rebound of the striking plate on an asphalt way is reduced. Figure 3.4a shows a raw shot gather for a shot of Line-3. The rebound of the striking plate is obvious and occurs as an additional arrival with apparent velocities equal to the first arrivals, which are highlighted by the red ellipses. It was possible to repress that additional, unwanted source signal (Figure 3.4c) because it was not equal for all shots but moved with the shot number (Figure 3.4b).

The profiles were really straight, so no approximations had to be applied for implementing the final geometry to the data. After assigning the final geometry to the raw data, the data was ready for picking the first arrival times.

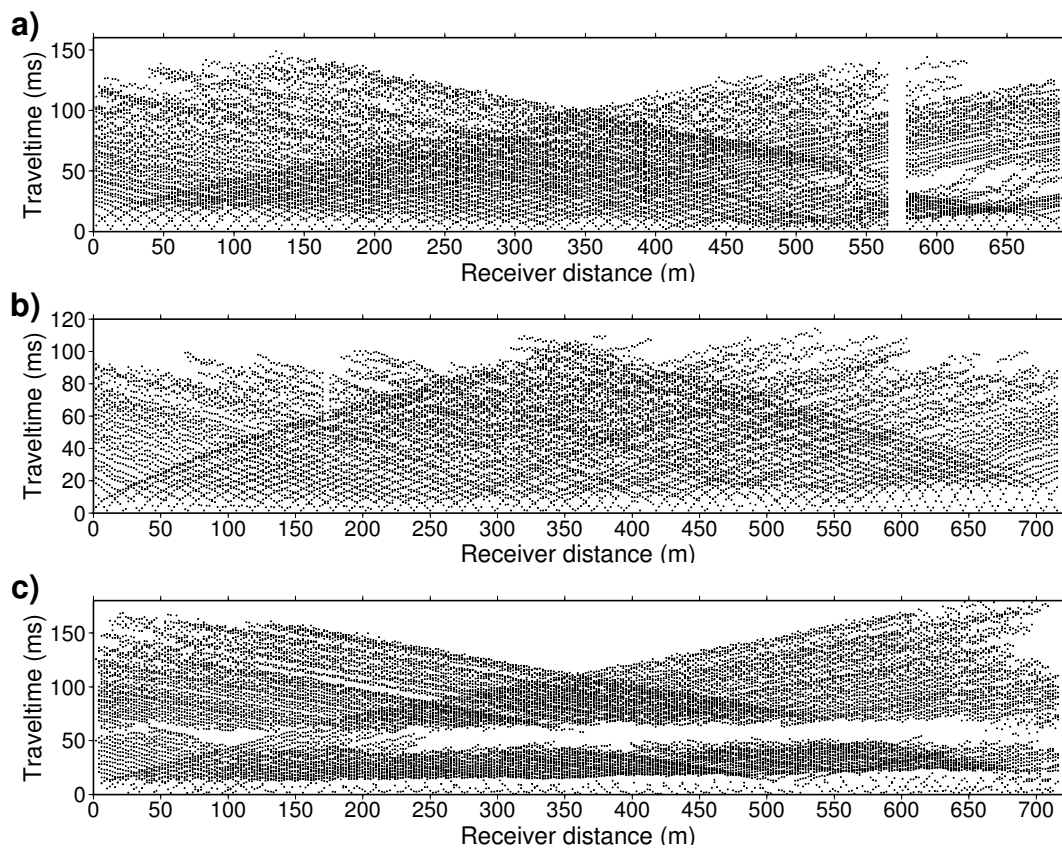


**Figure 3.5:** The picked traveltimes as a function of the receiver distance for Line-1 (a), Line-2 (b) and Line-3 (c).

### Traveltime picks

The traveltimes were picked manually. A total of 17369 traveltimes could be achieved for Line-1, 14622 traveltimes were picked for Line-2 and 18746 traveltimes were used for Line-3. The fewer values of traveltimes picks for Line-2 are due to the higher noise level at this location. The distribution of the traveltimes with receiver distance is plotted in Figure 3.5 and allows a first estimation of the underground structure. The gap in the

plot of Line-1 between receiver distances of 565 and 579 m is caused by the road where no shot points and receivers could be deployed. Figure 3.5a also shows a quite homogeneous distribution of traveltimes for small receiver distances, whereas the traveltimes are more disturbed for great distances. That gives an indication for a changing in the subsurface structure from the beginning to the end of the profile Line-1. The homogeneous distribution of the traveltime data of Line-2 reveals the assumption of a nearly one-dimensional underground at this profile. The distribution plot of the traveltimes of Line-3 (Figure 3.5c) shows a lack of traveltimes around 50 ms, like in the traveltime plot for large receiver distances of Line-1. Therefore, the underground structure of Line-3 is estimated to be equivalent to the structure of the southern part of Line-1.

The quality of the traveltime data can be estimated by calculating differences of the first arrival times of reversed shot and receiver pairs. These differences are plotted in a histogram (Figure 3.6). To predict the picking uncertainties, two different functions were fitted to the histograms and the errors in terms of standard deviations were calculated:

1. **Exponential distribution:**

$$y = f(x) = a \exp(-\lambda x), \quad (3.17)$$

where the standard deviation of the function is given by

$$\sigma = \frac{1}{\lambda}. \quad (3.18)$$

The green lines in Figure 3.6 show the exponential curve fitting the data best.

2. **Gaussian distribution:**

$$y = f(x) = \frac{1}{\sigma\sqrt{2\pi}} \exp\left(\frac{-x^2}{2\sigma^2}\right) \quad (3.19)$$

with  $\sigma$  representing the standard deviation.

The best fitted Gaussian curves are plotted in magenta color (Figure 3.6).

The standard deviations estimated by the above mentioned methods are summarized in Table 3.1.

	<b>Exponential</b>	<b>Gaussian</b>	<b>Mean</b>
	$\sigma$ in ms	$\sigma$ in ms	$\sigma$ in ms
Line-1	2.01	1.2	1.6
Line-2	1.29	1.3	1.3
Line-3	1.38	1.1	1.2

**Table 3.1:** Standard deviations  $\sigma$  estimated with different methods for all profiles.

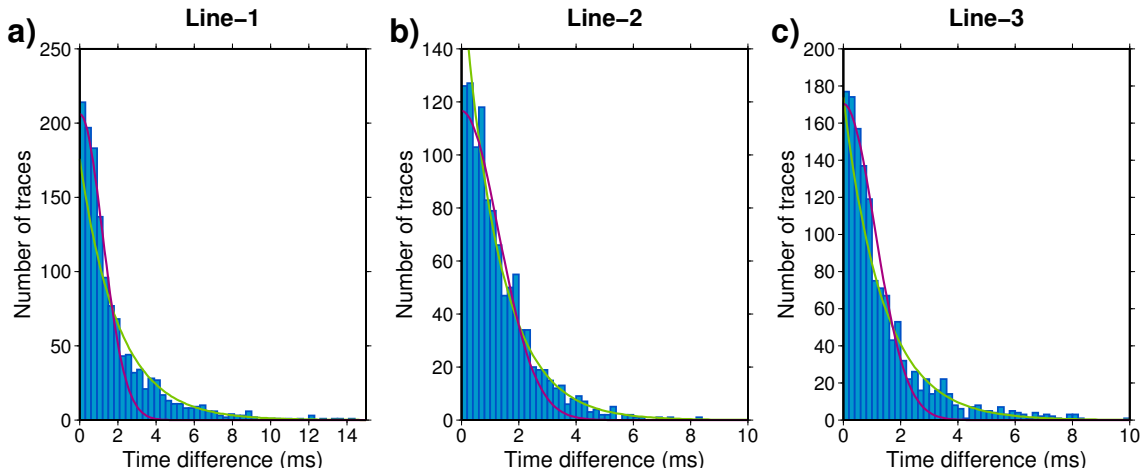


**Figure 3.6:** Traveltime differences for reversed shot and receiver pairs plotted in a histogram for Line-1 (a), Line-2 (b) and Line-3 (c). Inserted are the best fit exponential function (green line) and the best fit Gaussian function (magenta line).

For Line-2 the standard deviations achieved with the different fitting curves lead to almost the same value. Therefore, the uncertainty of the traveltime picks for Line-2 can be fixed at a value of 1.3 ms. The standard deviations for the uncertainty of Line-1 and Line-3 differ depending on the distribution. To get only one value, the mean value of both standard deviations is calculated for each profile. Thus, the picking uncertainty for Line-1 amounts 1.6 ms and the picking uncertainty for Line-3 can be estimated by a value of 1.2 ms.

### 3.2.2 Velocity modeling in one and two dimensions

Before the traveltime tomography could be applied to the 2D data, an initial model had to be found, which on the one hand accurately satisfied the traveltime data and which on the other hand is relatively simple (Eberhart-Phillips, 1990). A 1D velocity model with a positive velocity gradient was used, which means increasing velocity with depth. For Line-1 and Line-2 the same starting model was used. That 1D model satisfied the traveltime data of both seismic profiles very well and it gave a better comparability of both tomography results. The velocity model of Line-3 was obtained by using the sonic log information of the Skelbro-2 borehole. The sonic velocities were resampled to a resolution of 20 m in vertical direction. That means, the initial model of Line-3 was not as coarse as the other starting models, where an initial vertical resolution of 50 m was defined.

The 2D P-wave traveltime tomography was done with the SIMUL package (Thurber, 1983; Evans et al., 1994; Eberhart-Phillips & Reyners, 1997). SIMUL is a damped least-squares inversion algorithm which is based on ray-tracing (s. Section 3.1.3). Originally developed for the inversion of local earthquakes, it is a robust technique which can also be used for active source tomography. During the inversion, a full matrix solution of Equation 3.8

is calculated, which also includes the formal resolution of a certain velocity model and covariance matrices.

It is essential to use damping as a boundary condition to make the inversion stable (Equation 3.8). The optimal damping parameter can be obtained by performing single step inversions for a range of reasonable damping values (Eberhart-Phillips, 1986). After the iteration, the error between calculated and observed traveltimes (data variance) and the variance of the velocity model in relation to the starting model (model variance) is obtained. Both variances can be plotted in a trade-off curve. The optimal damping parameter is found when both variances are minimized, which means that the balance between model perturbation and traveltime fitting is optimized.

The trade-off curves for Line-1, Line-2 and Line-3, respectively, are plotted in Figure 3.7. For the first two profiles a value of 50 can be estimated as the optimal damping value, whereas a value of 100 is chosen optimal for Line-3.

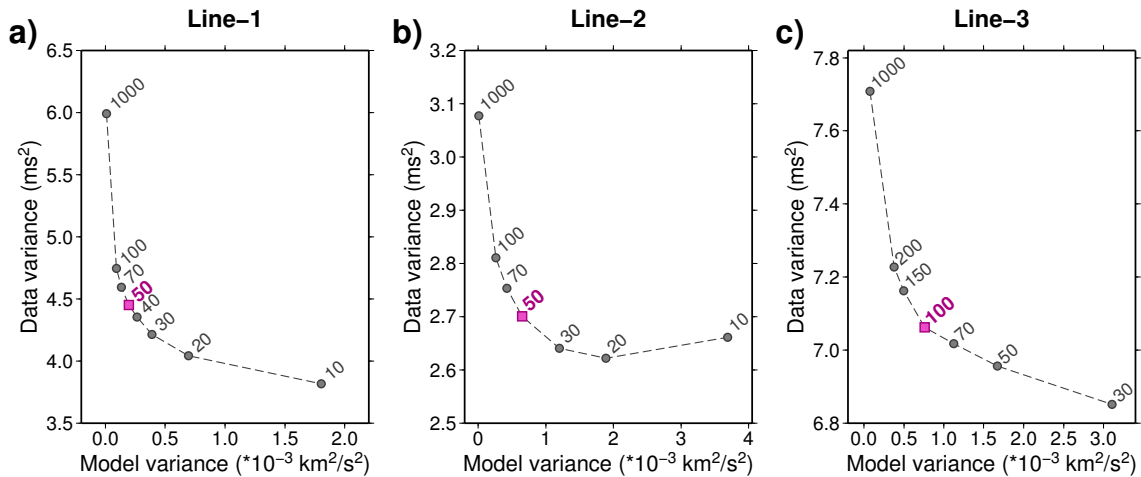


**Figure 3.7:** Trade-off curves for all profiles to estimate the optimal damping parameter.

For a range of damping values, one-step inversions were carried out and the model variances and data variances were calculated. The preferred damping values are highlighted by magenta color and a square.

The linearization approach for the traveltime tomography (Section 3.1.1) is only valid for small model corrections with respect to the initial model (Thurber, 1983). Therefore, a graded inversion strategy was performed (Evans et al., 1994; Baumann-Wilke et al., 2012) where the inversion was started with a coarse model and the model grid was systematically refined. That method reduces the possibility of the algorithm to converge into local minima and also reduces the influence of the initial model on the final velocity structure. Inversion artifacts appearing as hyperbola-shaped velocity anomalies will also be prevented using that technique.

For Line-1 and Line-2, a total of five inversion steps each with three iterations was carried out, whereas four inversion steps each with five iterations were calculated for Line-3. After every inversion step, the achieved model was resampled and served as the input model for the next inversion step. The grid spacings of every inversion step are summarized in Table 3.2.

Inversion step	Horizontal spacing $dx$ (m)	Vertical spacing $dz$ (m)	Figure 3.8
1	200	50	(b)
2	100	20	(c)
3	50	10	(d)
4	20	5	(e)
5	10	2	(f)

**Table 3.2:** Grid spacings of the graded inversion. Every inversion step consists of three or five iterations and the horizontal as well as the vertical grid spacing is systematically decreased. The corresponding figure with the velocity models after every inversion step is indicated in the right column.

The starting model and the velocity models after every inversion step for Line-1 are plotted in the left part of Figure 3.8. Already after six iterations, in the second inversion step (Figure 3.8c, left) the influence of the 1D initial model vanishes and southward dipping structures become visible. A thin high velocity layer at shallow depth in the southern part of the profile emerges in the third inversion step (Figure 3.8d, left) and becomes more clear during the remaining iterations. Figure 3.8f (left) shows the final tomography model after a total of 15 iterations. It will be discussed in section 3.3.1.

The evolution of the graded inversion can also be seen in the left part of Figure 3.9, where residual traveltimes (difference of observed and calculated traveltimes) are plotted for the initial model and all inversion steps of Line-1. The residuals for the starting model ranging between -15 ms and 15 ms are reduced significantly during the inversion process. Only for large source and receiver distances, that means in the southern part of the seismic line, some traveltimes cannot be well resolved. That might be related to the more complex geometry in this part of the profile which can be seen in the final tomography model (Figures 3.8f, 3.15)



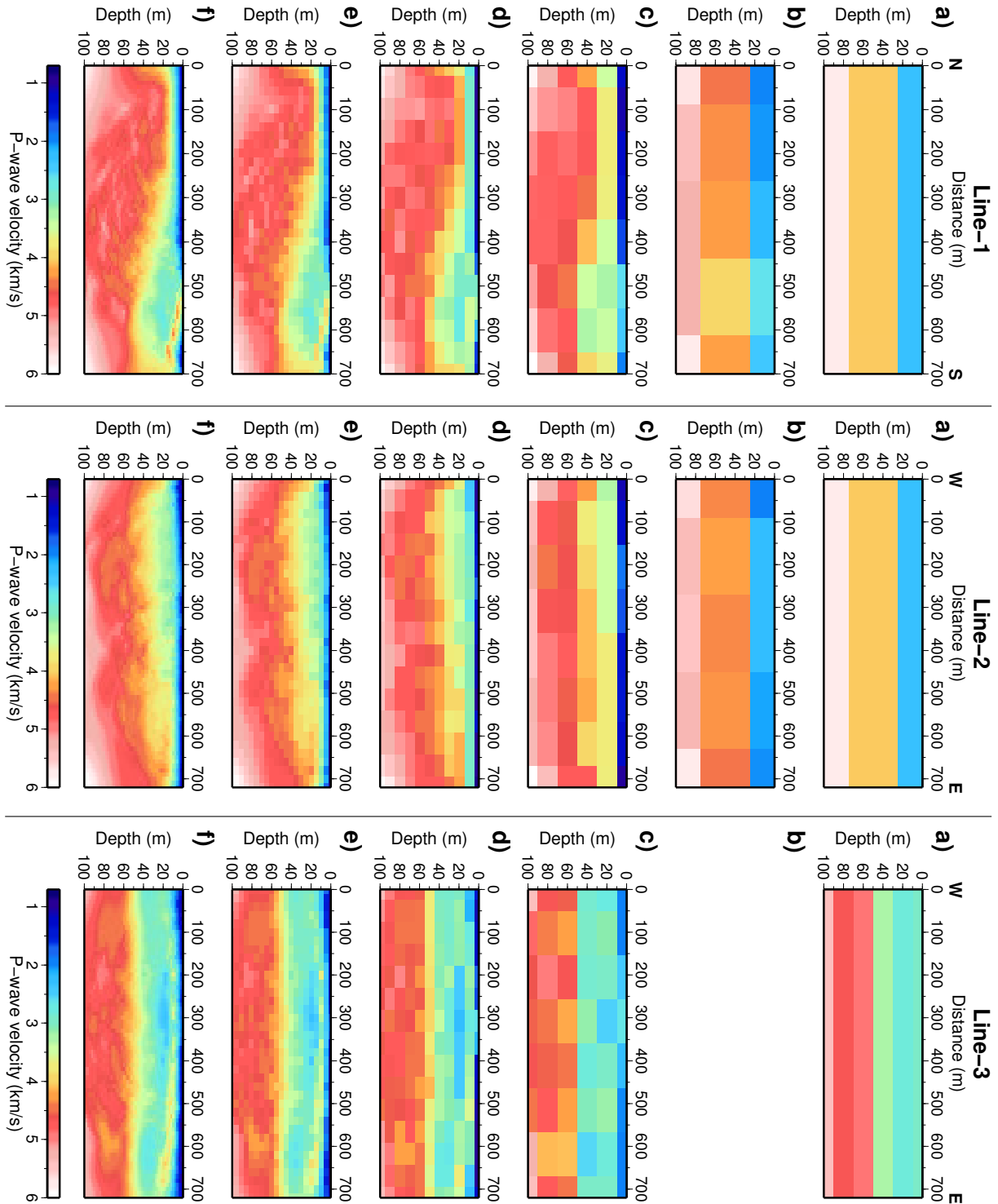


**Figure 3.8:** Development of the graded inversion for all profiles. The velocity models of Line-1 and Line-2 were derived using the same starting model (a). The grid spacing was systematically decreased from  $dx = 200$  m and  $dz = 50$  m (b) to  $dx = 10$  m and  $dz = 2$  m (f). The grid spacings of the individual models can be found in Table 3.2. The left part of the plot shows the velocity models of Line-1, in the middle part the models of Line-2 can be found and on the right side are the tomography models of Line-3.



The velocity models of the graded inversion for the perpendicular profile Line-2 are shown in the middle part of Figure 3.8. It can be seen that the model is only changing little during the inversion steps. All tomography models show an overall relatively one-dimensional velocity increase with depth. But a slightly westward dipping of the structures is visible after inversion step 3 (Figure 3.8d, middle).

The traveltime residuals for Line-2 (Figure 3.9, middle) show a good resolution during the inversion. Only near the zero-offset traces (diagonal line) the calculated traveltimes tend to be a little too low compared to the observed traveltimes which leads to higher residuals. That might be affected by the unconsolidated subsurface in the shallowest part of the profile.

As in the other profiles, also the tomography model of Line-3 (Figure 3.8, right part) relatively fast finds the upper boundary of the high velocity structure at great depth of the model. But in the model of Line-3, that boundary shows constant depth of about 50 m over the whole horizontal distance. Similar to the southern part of Line-1, the high velocity structure is overlain by a low velocity layer between 10 and 50 m depth and again a high velocity layer between 5 and 10 m depth. The high velocity structure above at shallow depth is not as clear as for Line-1.

The traveltimes of Line-3 are well resolved after some iterations (Figure 3.9, right). Only at the jumping point of the traveltime, the residuals are a little higher than in the other parts.

The evolution of the traveltime residuals can also be described by the RMS (root mean square) error (Figure 3.10), which is calculated with

$$\text{RMS} = \sqrt{\frac{\sum_{i=1}^n (t_i^{cal} - t_i^{obs})^2}{n}}, \quad (3.20)$$

where  $t_i^{cal}$  are the calculated traveltimes,  $t_i^{obs}$  are the observed traveltimes and  $n$  is the number of measurements.

For Line-1, the RMS error for the starting model is 5.6 ms and converges to a value of about 2.1 ms during the inversion process, whereas the RMS for Line-2 already starts at a relatively low value of 3.9 ms. The error for Line-2 only slightly decreases till it reaches a value of 1.5 ms. The RMS error for the starting model and the traveltimes of Line-3 is at a value of 9.4 ms. It strongly decreases during the first inversion step consisting of five iterations. Afterward, the change is not as dramatically as for the first step and a final value of 2.4 ms is reached after 20 iterations. All final RMS values are greater than the determined picking uncertainty (Section 3.2.1). It means, that the tomography was not over-iterated into noise which might be a cause of artifacts.

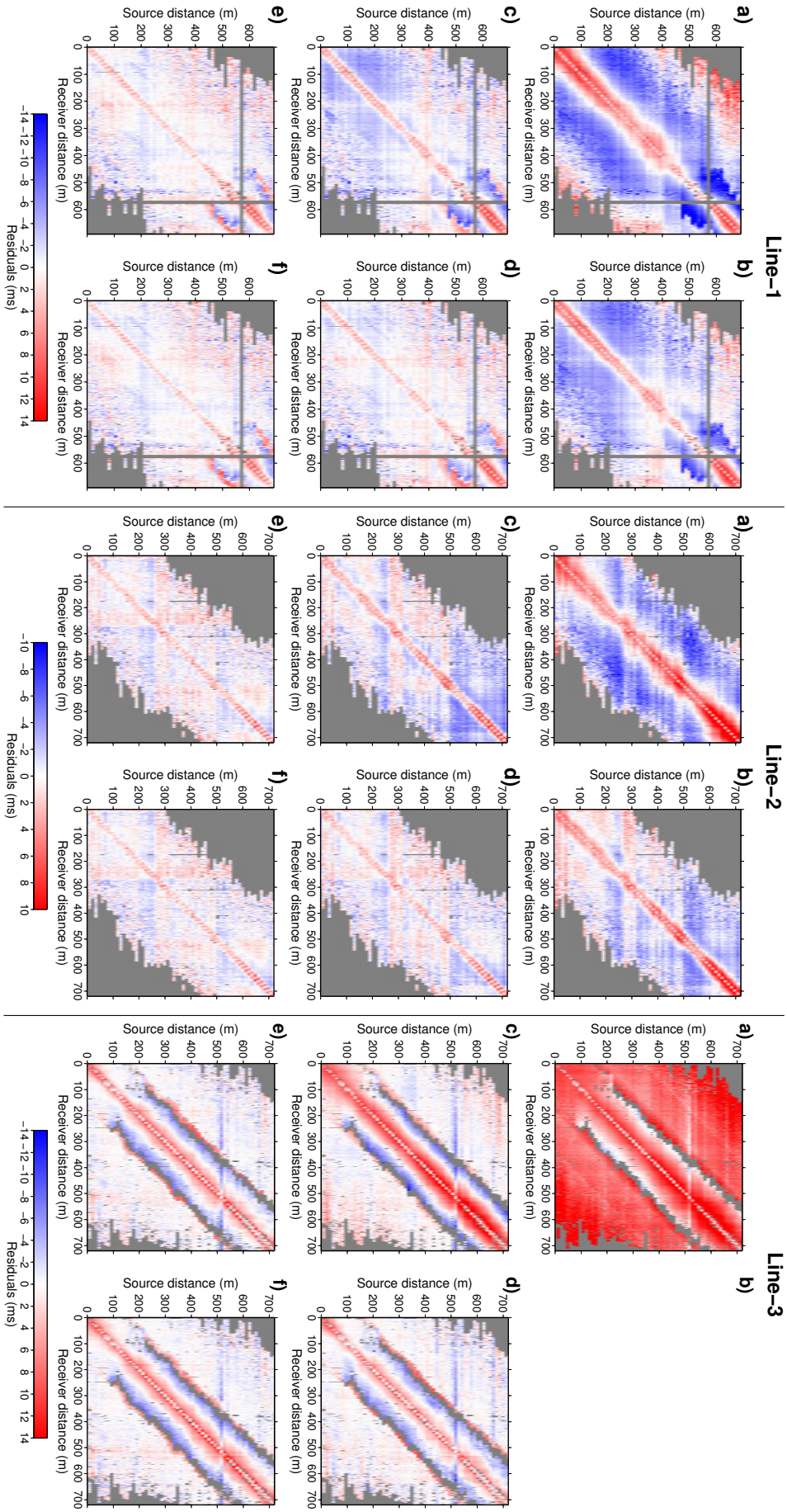


**Figure 3.9:** Development of the graded inversion shown with the residual traveltimes for all lines. The labeling of the plots (a) - (f) is consistent with Figure 3.8 and indicates the different inversion steps.

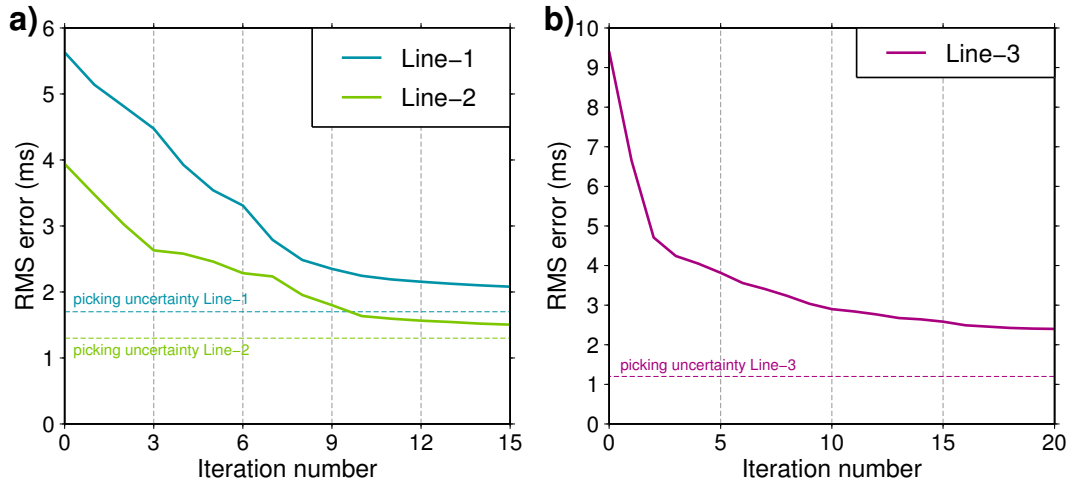


**Figure 3.10:** Evolution of the RMS (root mean square) error during the iteration steps. Every end of an iteration step is indicated by a dashed gray line. (a) RMS error for both Line-1 and Line-2, where every inversion step consisted of 3 iterations. (b) The RMS error for Line-3.

The difference between the final RMS value and the estimated picking uncertainties is much smaller for the profiles Line-1 and Line-2 as it is for Line-3. That might be an indication that the final tomography model of Line-3 is not as well resolved as the other models. For Line-3 also other starting models were tested, but a smaller RMS than that depicted in Figure 3.10 could not be reached. The reason of that large difference of final RMS and picking uncertainty must be found in the complexity of the subsurface structure itself.

### 3.2.3 Resolution of the velocity models

#### Checkerboard test

Resolution tests are important to estimate the reliability of the final velocity models. One method to analyze the lateral resolution of tomography models is the checkerboard test (Zelt, 1998). Therefore, the velocity model is superimposed by a checkerboard pattern of alternating positive and negative velocity perturbations. Different checkerboard sizes are used to analyze the resolution of the tomography model at different scales. Therefore, the checkerboard patterns depend on the lateral size  $dx_{cb}$  and the vertical size  $dz_{cb}$ . The checkerboard can then be described by the following equation:

$$cb = \sin\left(\frac{\pi x}{dx_{cb}}\right) \sin\left(\frac{\pi z}{dz_{cb}}\right), \quad (3.21)$$

where  $x$  is the distance and  $z$  denotes depth. The checkerboard values vary between  $cb = -1.0$  and  $cb = 1.0$ . An example of a checkerboard pattern is plotted in Figure 3.11.

It is necessary to use a relatively smooth change from one checkerboard cell to an adjacent cell. Otherwise, with sharp boundaries, inversion artifacts will occur.

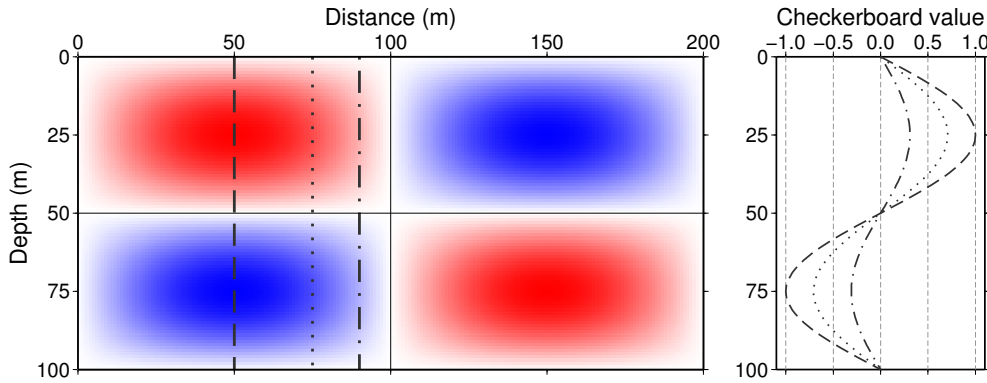


**Figure 3.11:** Example of a checkerboard pattern of the size  $dx_{cb} = 100$  m and  $dz_{cb} = 50$  m. The lines in the right panel correspond to the checkerboard values with depth for  $x = 50$  m (dashed),  $x = 75$  m (dotted) and  $x = 90$  m (dashed-dotted).

The checkerboard patterns (Equation 3.21) were superimposed on the starting model of the tomographic inversion of Line-1, that means the result of the 1D inversion, with a grid spacing of  $dx = 10$  m and  $dz = 2$  m. Three different pattern sizes for the checkerboards were used:  $70 \times 10$  m,  $140 \times 20$  m and  $180 \times 25$  m, where the aspect ratio was chosen equal to the ratio of horizontal and vertical extension of the tomography model. The subsurface structure was expected to be laterally layered, therefore, the checkerboard patterns were chosen with a higher horizontal extension compared to the vertical size of the patterns. For each checkerboard model, traveltimes were calculated using the source and receiver configuration of the real measurements (Section 2.2). To approximate true measuring conditions, Gaussian noise was added to the synthetic traveltimes. Therefore, the standard deviation of the Gaussian distribution was chosen similar to the picking uncertainty (Section 3.2.1).

With the noisy traveltimes, three iterations were then carried out using the same inversion parameters and starting model as for the tomographic inversion in Section 3.2.2. The starting model was subtracted from the obtained tomography model to achieve the resolved checkerboard patterns. The comparison of original and resolved checkerboard patterns for the used patterns sizes is plotted in Figure 3.12. The checkerboard test was performed only for the geometry of Line-1. But the results should be transferable to the other seismic profiles because source distances and receiver spacings of all lines were equal.

The recovered checkerboard patterns show a good resolution for shallow depths. The resolution decreases with increasing depth and also with decreasing checkerboard size.

Checkerboard patterns of  $70 \times 10$  m can sufficiently be recovered up to 50 m depth, whereas greater checkerboard patterns ( $140 \times 20$  m,  $180 \times 25$  m) can be imaged over the full vertical extension of the model. Due to the noise which was added to the traveltime data, the resolved checkerboard patterns are not as clearly defined as the original checkerboard patterns. The semicircular shape of the recovered checkerboard patterns is caused by the insufficient ray coverage in the boundary areas. The ray coverage can be described by the spread value.

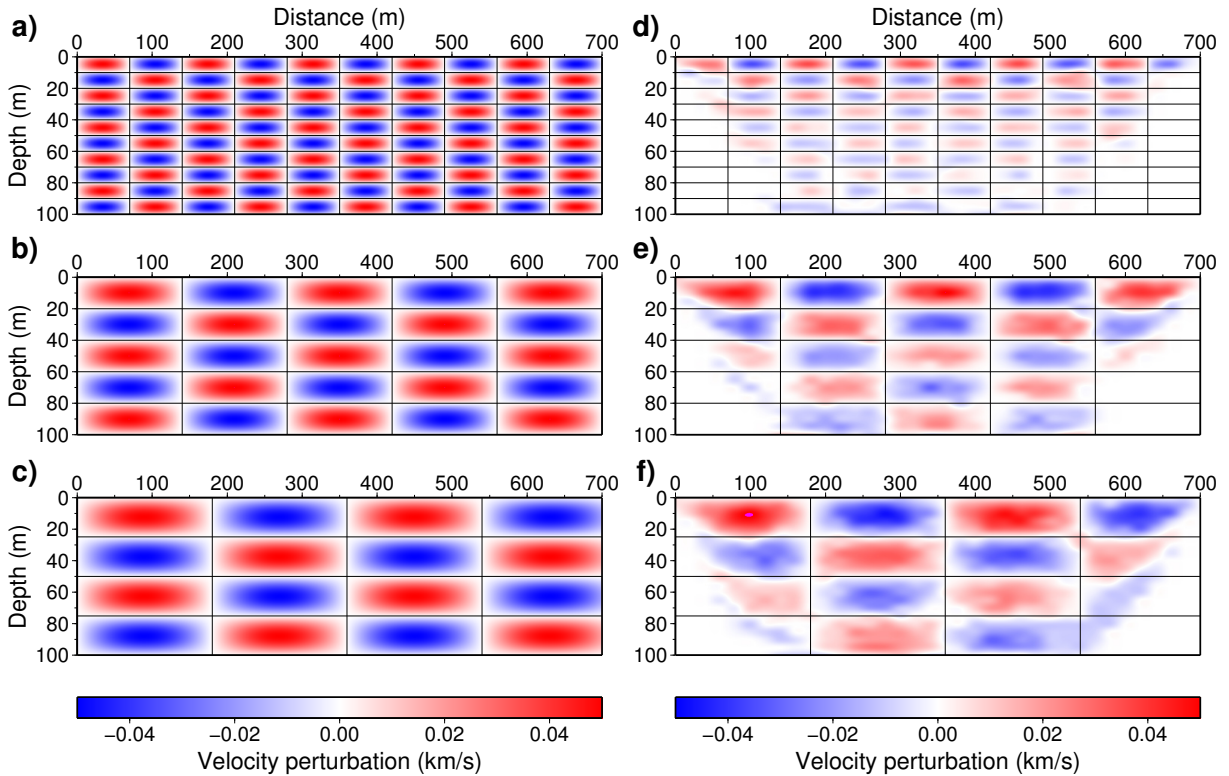


**Figure 3.12:** Original and resolved checkerboard patterns for three pattern sizes: (a) and (d)  $70 \times 10$  m, (b) and (e)  $140 \times 20$  m and (c) and (f)  $180 \times 25$  m, respectively.

### Spread value

The spatial resolution of the velocity model can further be estimated using the resolution matrix (Menke, 1989; Toomey & Foulger, 1989) which is calculated during the inversion. It gives an impression of the ray coverage of the model: well covered areas show a good resolution. The resolution matrix has the shape of an identity matrix if the velocity model is perfectly resolved. Otherwise, the off-diagonal elements of the resolution matrix characterize the dependency of the single model parameters among one another. The sensitivity of each model parameter is then represented by the value of the diagonal elements.

The spread value  $s_j$  of a model node  $j$  can be calculated after Michelini and McEvelly



(1991) using the resolution matrix  $\mathbf{R}$  (Eq. 3.9):

$$s_j = \log \left( \left\| \mathbf{r}_j \right\|^{-1} \sum_{k=1}^N \left( \frac{r_{kj}}{\left\| \mathbf{r}_j \right\|} \right)^2 D_{jk} \right), \quad (3.22)$$

where  $\mathbf{r}_j$  is the averaging vector of the  $j$ th model parameter,  $r_{kj}$  are the elements of the corresponding rows of  $\mathbf{R}$ ,  $D_{jk}$  is the distance between the model nodes and  $N$  is the number of model parameters.

The calculated spread values for all seismic profiles are plotted in Figure 3.13. Areas with low spread values are well resolved, whereas high spread values indicate an insufficient resolution. The final tomography models (Figures 3.15, 3.16) are clipped according to their resolution at a spread value of  $s_j = 4$ , which is a little less than half of the maximum occurring spread value.

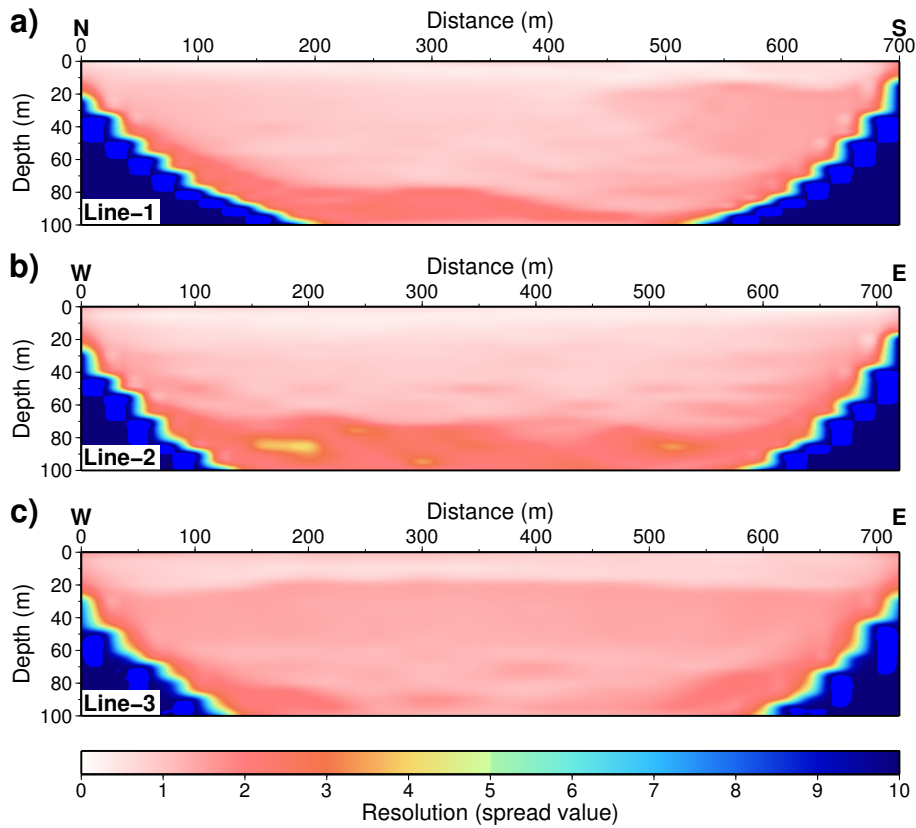


**Figure 3.13:** Distribution of the spread value for Line-1 (a), Line-2 (b) and Line-3 (c). High spread values denote insufficient resolution, whereas in parts with low spread values, the velocity model is well resolved.

### High velocity layer

High velocity layers (HVL) mostly pose a problem for the ray-based tomographic inversion only using traveltimes. Most of the seismic energy will be concentrated in the HVL and the velocity layers below will only be sufficiently imaged if a velocity gradient is present

and the source and receiver distance is large enough to have long ray paths.

The lithostratigraphy of both scientific boreholes Skelbro-1 and Skelbro-2 (Section 2.4) along the profile Line-3 indicate that the Komstad Limestone layer is covering the Alum Shale at shallow depth throughout the whole profile. To test, if such a velocity structure can be accurately resolved with traveltimes tomography, traveltimes were calculated for a synthetic velocity model including a HVL (Figure 3.14a). The synthetic traveltimes were then used for a tomographic inversion with the same parameters as for the analysis of the real data of Line-3.

After 20 iterations of the graded inversion, the velocity model displayed in Figure 3.14b arose. In Figure 3.14c, the vertical profiles through the synthetic model (solid line) and through the resolved velocity model (dashed line) are shown for a quantitative comparison of the velocities. It can be seen, that the velocity of the HVL is not reached in the resolved model and that the thickness of the HVL is overestimated leading to higher velocities in the layers directly beneath the HVL. The difference in the velocity value of the HVL between synthetic and resolved model is about half of the maximum value of this layer. At the outer edges of the resolved model, the HVL is thickened to greater depths. However, the velocity structure beneath the HVL is imaged very well and, despite the discrepancy in the velocity values of the HVL, the traveltimes tomography gives accurate results.

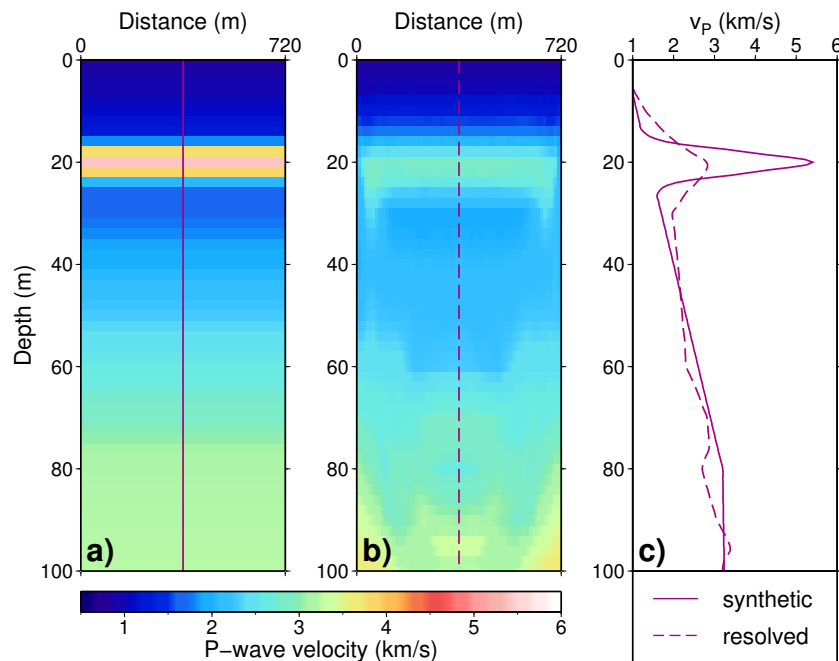


**Figure 3.14:** Imaging test of a high velocity layer (HVL). (a) Synthetic model with HVL at shallow depth. (b) Resolved velocity model using the synthetic traveltimes of (a). (c) The velocity of the HVL is not reached, but the velocity structure beneath is accurately imaged.

## 3.3 Results

### 3.3.1 Final tomography models

The final tomography models (Figures 3.15 - 3.17) were derived after a total of 15 iterations (Line-1 and Line-2) or 20 iterations (Line-3) and with a grid spacing of  $dx = 10$  m and  $dz = 2$  m. The final RMS errors (Figure 3.10) reached 2.1 ms, 1.5 ms and 2.4 ms, respectively, and are all above the picking uncertainty which prevented iteration of noise. The results of Line-1 and Line-2 are also described by Baumann-Wilke et al. (2012).

In the image of the final tomography model of Line-1 (Figure 3.15), the position and depth of the borehole Skelbro-2 is marked by the blue triangle and the blue line. The connection to the borehole was used for the separation of the different layers. It is known from Schovsbo et al. (2011) (Section 2.4), that the top of the black shale layer (Alum Shale) at Skelbro-2 is at 8.5 m depth and the bottom is at 42 m depth. The top of the limestone layer (Komstad Limestone) was found at 4.5 m depth. These depth values were used to define the boundary velocities in the tomograms. The contour lines with the achieved boundary velocities were calculated and served as input parameters for a linear regression. The final velocity model (Figure 3.15) shows the derived linear boundaries between the different formations with dashed gray lines. The transition of the overburden to the consolidated material is indicated by the contour line at low depth which has not been linearized. All calculated linear layer boundaries are tilted to the south showing all the same dipping angle of  $7^\circ$ .

After Schovsbo et al. (2011), the Læså Formation is found at greatest depth in the final tomogram. It shows the highest thickness of all layers in the velocity model. This sandstone layer has high velocities around 5 km/s and it is overlain by the Alum Shale Formation in the southern part of the profile. The Alum Shale is characterized by P-wave velocities around 3 km/s and is, therefore, clearly separated from the sandstone layer with higher velocities. The most southern part of the Alum Shale is overlain by the Komstad Limestone Formation. The limestone layer has a thickness of about 4 - 5 m and velocities around 4 km/s, which are again higher than the velocities of the black shale layer. But, the achieved limestone velocities are lower than it was expected from the sonic log of the Skelbro-2 borehole (Section 2.4).

At the southern edge of the model, the tomogram is influenced by border effects leading to a smearing of the velocity structure and, therefore, higher velocities for the Alum Shale layer. Although, following the definitions of Section 3.2.3, this part of the model is well resolved, it must be examined critically. The linear layer boundaries are inserted beyond the resolved part of the model, because that is the expected trend of the different formations. But that trend cannot be clearly identified in the southernmost part of the velocity structure of the tomogram.



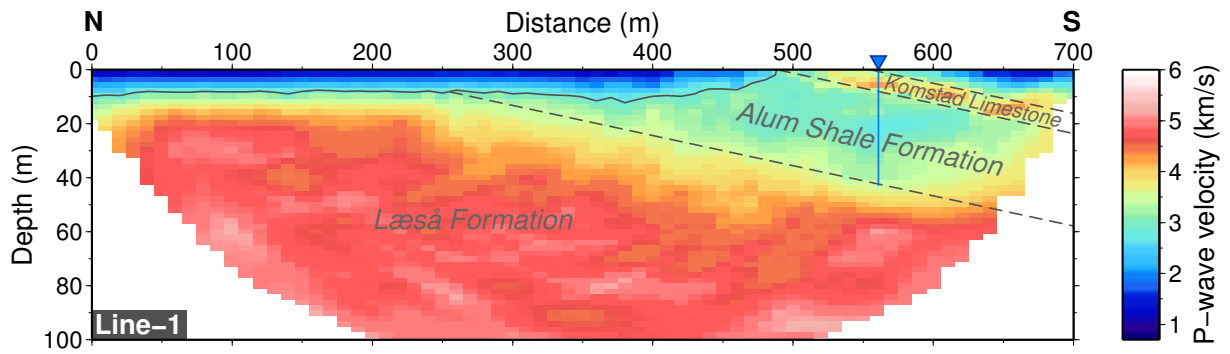


**Figure 3.15:** The final P-wave tomography model of Line-1 shows three identified layers: the Læså Sandstone Formation, the Alum Shale Formation and the Komstad Limestone Formation. All layers are found dipping southward. The position and depth of the borehole Skelbro-2 is indicated by the blue triangle and line.

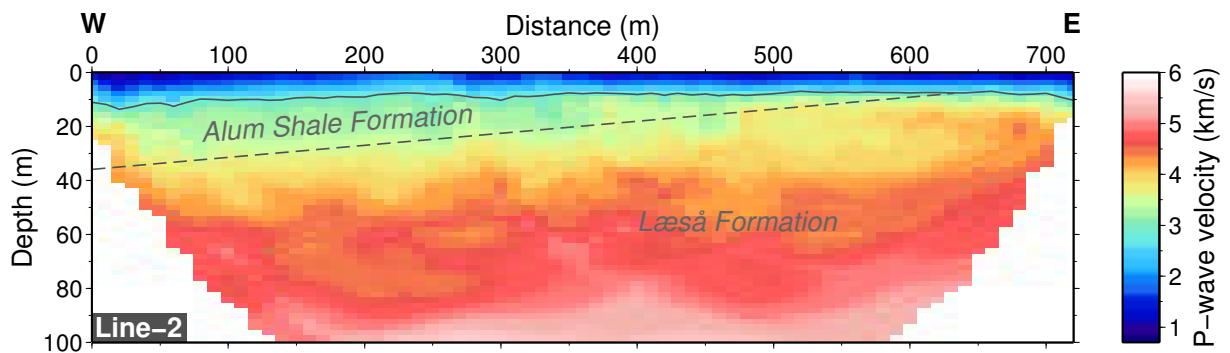


**Figure 3.16:** In the final P-wave velocity tomogram of Line-2 the Læså Formation and the Alum Shale could be identified. An overall increasing velocity with depth is found for this profile.

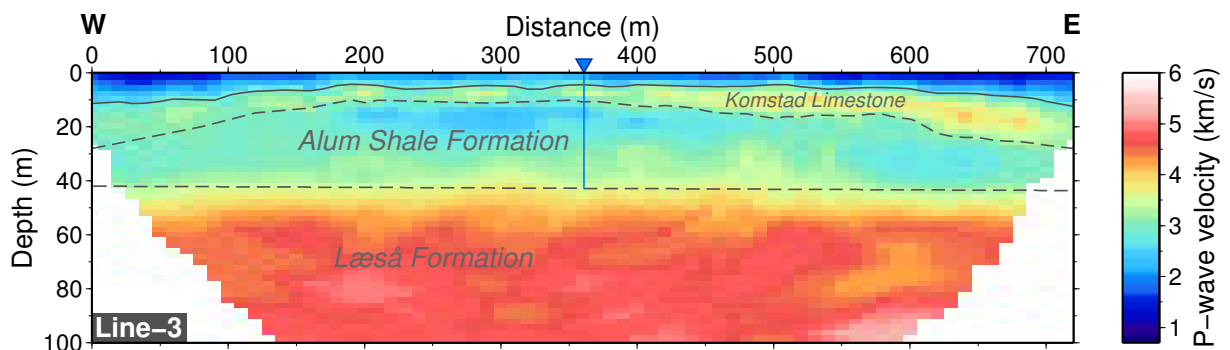


**Figure 3.17:** Final P-wave velocity model for Line-3. The Alum Shale is overlain by the Komstad Limestone Formation throughout the whole profile distance. No dipping of the layers is visible. The limestone velocities of the first seismic profile are not reached here.

Within the Læså Sandstone Formation, a difficulty of the ray-based traveltime tomography is obvious: the velocity is smeared along hyperbolas. That problem has its cause in the fine resolution of the model. Some cells of the final model are no longer penetrated by rays, therefore, the model is not updated in those parts. On the other hand, in cells where a ray is passing, the velocity is updated at each iteration. Due to the variance in the update of the model, the ray paths slightly become visible in the final velocity structure.

Nevertheless, if the above mentioned difficulties are disregarded, the final tomography model of Line-1 is very well resolved. Even small scale velocity perturbations can be localized inside the Alum Shale Formation. On top of the black shale layer, the P-wave velocity is around 2.8 km/s and at the bottom of the Alum Shale velocities of 3.5 km/s are found. That means, there is an increasing black shale velocity with depth. That is also observed in the sonic log velocities (Figures 2.5 and 3.19).

In the final P-wave tomography model of Line-2 (Figure 3.16), the black shale velocities cannot be separated as clearly as for the result of Line-1. The velocity increase with depth in the shallow part of the model is not as rapid as for Line-1, so that the boundary between the different stratigraphical formations is not very strong. The black shale layer in the model of Line-2 is separated from the adjacent formations using the top and bottom velocities of the Alum Shale derived for the tomogram of Line-1. The contour line for the lower boundary (velocity: 3.5 km/s) has again been linearized with a regression. The Alum Shale Formation is now found slightly dipping westward with a thickness of at most 25 m and only covering the Læså Sandstone Formation in the west part of the profile. No limestone layer is visible, but it was not expected from the result of Line-1, where the Komstad Limestone fades out before the distance where Line-2 is crossing. The P-wave velocity is increasing with depth and no low-velocity layer is present. The velocity gradient at the first 50 m depth is a little smaller compared to Line-1, so that the top of the sandstones has velocities around 3.8 km/s. The gradient becomes larger for greater depth and the Læså Formation reaches velocities which are higher ( $\sim 5.5$  km/s) then for Line-1.

The boundary between the Læså Sandstone Formation and the Alum Shale Formation is clearly visible and appears horizontally in the P-wave tomography result of the additional profile Line-3 (Figure 3.17). The velocities of the black shale layer and the sandstone formation are comparable to the velocities found in Line-1. But the Komstad Limestone Formation shows not as high velocities as in the model of Line-1. In the western part, the limestone can almost not be distinguished from the Alum Shale because both show velocities around 3 km/s. The limestone layer is found throughout the whole profile

distance covering the Alum Shale. The overlaying high velocity layer is problematic for the imaging of the deeper structures. Nevertheless, all stratigraphical formations of the Skelbro-2 borehole are also found in that tomographic result. Possible difficulties can be seen in the thickening of the limestone at the east and west edge of the model and in the weak velocity contrast of Alum Shale and Komstad Limestone.

At the borehole location, the boundary between the Læså Formation and the Alum Shale is found at a depth of 42.8 m, which matches with the tomography model of Line-1 at this position. The top of the Komstad Limestone is found at 4.4 m depth and the bottom at 10.8 m. That means, in that velocity model, the limestone layer is stretched vertically compared to the model of Line-1 and also compared to the lithostratigraphy described in Section 2.4.

The combined plot of all velocity models shows a good correlation (Figure 3.18). Although the models were derived independently and in part calculated with different starting models, all profiles match very well. Especially the bottom depth of the Alum Shale is well resolved by all models and shows almost no difference at the cross points of the profiles. The Komstad Limestone velocities of Line-1 are higher compared to the velocities in Line-3, but the structure of the limestone layer is appropriately resolved in both profiles. Line-1 and Line-2 show a slightly dipping of the layers, whereas in Line-3 no such behavior can be observed. Therefore, the Alum Shale layer is expected to dip southward.

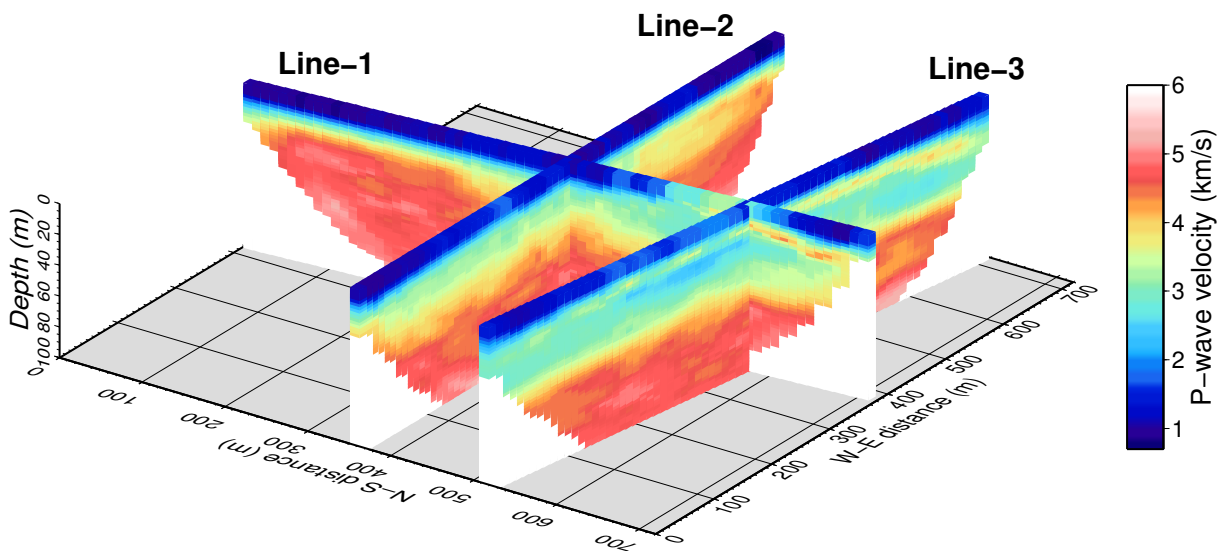


**Figure 3.18:** Final velocity models of Lines 1 to 3 in a combined plot. The three-dimensional structure of the identified layers can be estimated with that plot. Although the models were derived with different initial models and a different number of total iterations, they match really well at the cross points.

### 3.3.2 Comparison with borehole information

The sonic log of the Skelbro-2 borehole drilled in August 2010 (right part and gray line in Figure 3.19) was used for a comparison with the velocities of the traveltime tomography. For better comparability, the sonic log velocities in the right plot of Figure 3.19 were resampled with a vertical distance of 2 m according to the parametrization of the final tomography models. In the resampled sonic log, the small scale velocity fluctuations are reduced and the main velocity structures are visible. The middle part of Figure 3.19 shows the sonic log as image plot, so that it is comparable to the velocity tomograms of both seismic profiles crossing the borehole.

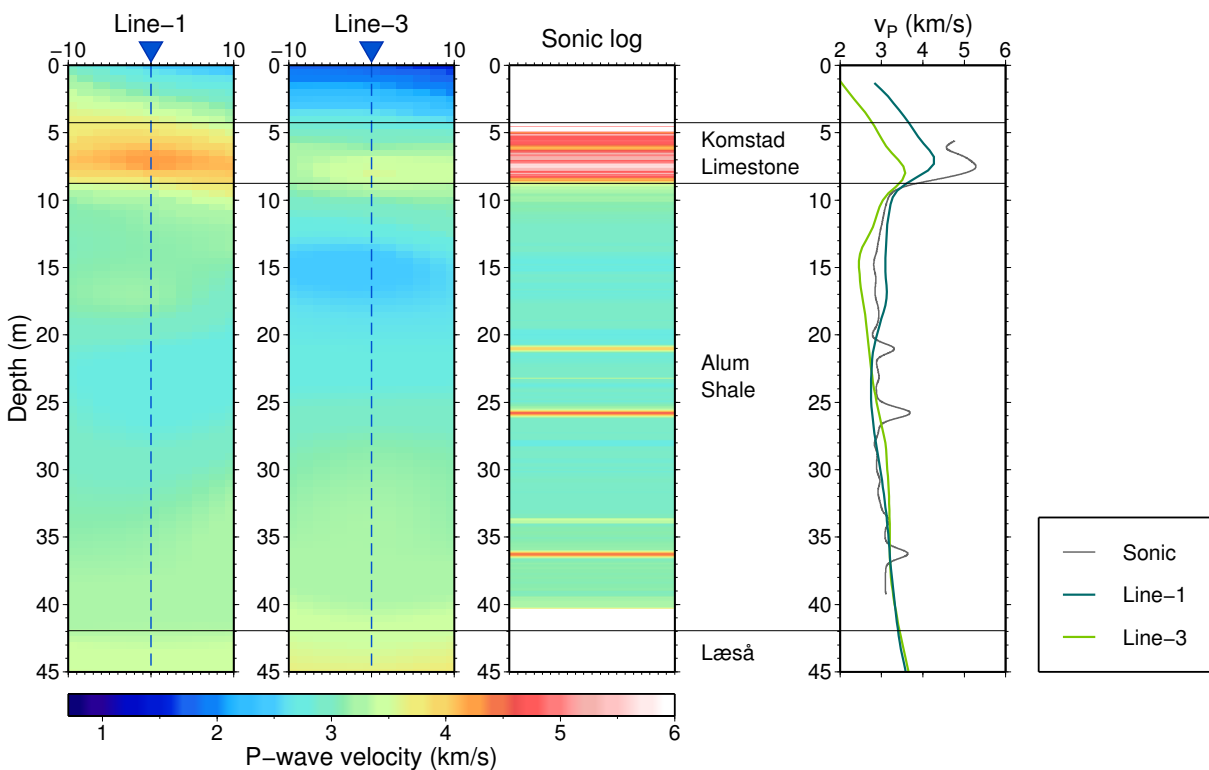


**Figure 3.19:** The vertical velocity profiles of the resulting models of Line-1 and Line-3 at the borehole location compared with the sonic log velocities of the Skelbro-2 well.

The two left panels of Figure 3.19 are showing details of the final tomography models of Line-1 and Line-3, respectively, for a distance of  $\pm 10$  m around the borehole location Skelbro-2. Inserted in the figure are the boundaries of the stratigraphical classification marked by the thin black lines (cf. Section 2.4). The depth of the Komstad Limestone layer is imaged very well by the tomogram of Line-1 but it is a little overestimated by the velocity model of Line-3. The overall velocity of the Alum Shale is imaged quite well with both models but a better assessment can be made with the plot of the vertical velocity

profiles at the borehole location shown in the right panel of Figure 3.19.

The vertical velocity profile of Line-1 very well fits the sonic log. Also the Komstad Limestone layer is resolved, only the velocity is too low. The Alum Shale velocities match very well, but in the upper part they are a little too high. Here, the model velocities are influenced by the higher limestone velocity and by the smoothness of the travelttime tomography. The smoothness is also the reason for not resolving the small scale inclusions of limestone in between the Alum Shale. At greater depth (below 20 m), there is a really good match between the tomography velocities and the sonic log velocities. That is also visible for the vertical velocity profile of Line-3. Nevertheless, at shallow depth there are great differences in the velocity profile of Line-3 and the sonic log. The velocity of the Komstad Limestone is not reached at all and the Alum Shale velocities of the upper 10 m of that formation are also underestimated. Again, the small scale inclusions of diagenetic limestone are invisible for the travelttime tomography.

The reasons for the large differences in the shallow part of the subsurface might be diverse. One problem is the Komstad Limestone layer itself because it covers the Alum Shale in large parts of the profile (Line-1) or throughout the whole seismic line (Line-3). In Section 3.2.3 an imaging test was carried out with a synthetic model which revealed that it is not possible to recover the true velocities of a high velocity layer at shallow depth using travelttime tomography. The velocities of the high velocity layer are considerably underestimated as it is the case for the travelttime tomography results of the field data. Anisotropy effects may cause the differences between the perpendicular profiles Line-1 and Line-3. The differences are only found in the upper part of the Alum Shale which could be in correlation to the lithostratigraphical subdivision of the black shale into different units (Section 2.4). Therefore, the Ordovician part of the Alum Shale may show anisotropy effects, whereas the Furungian and Cambrian parts below have no such behavior. Besides the anisotropy or resolution effects, the velocity of a formation is also influenced by the porosity, water saturation and other geochemical properties which will affect the different measurements in a different way.

However, in the upper part of the Alum Shale, the average of both velocity profiles of Line-1 and Line-3 will almost perfectly match the sonic log velocities and in the deeper parts all individual profiles show a very good agreement. That is an indication for the validity and reliability of the travelttime tomography method. Possible causes of the observed differences will be discussed in more detail in Section 3.4.

### 3.3.3 Correlation to the TOC content

Schovsbo et al. (2011) found a linear correlation between the seismic velocities of the Alum Shale and the content of organic carbon (TOC) of the black shale formation. The

correlation to the TOC content was proven by using the sonic log velocity and the velocities of the Alum Shale layer derived by the travelttime tomography of the two profiles which were crossing the borehole location.

The TOC content values of Alum Shale samples were provided by the Geological Survey of Denmark and Greenland (GEUS). The sonic log velocity and the tomography model velocities for the depth values were extracted where a TOC content has been measured. Then, the TOC content was plotted as a function of velocity (Figure 3.20) and a linear regression was carried out to extract the linear trend. The slope and intercept of the calculated regression curves ( $TOC = a v_P + b$ ) as well as the corresponding root mean square (RMS) error values (see Equation 3.20) are summarized in Table 3.3.

Correlation with	Slope $a$	Intercept $b$	RMS
Sonic velocity	-9.2232	36.0265	1.1656
Model Line-1	-4.1342	21.1419	1.3263
Model Line-3	-1.9349	14.3522	1.4529

**Table 3.3:** The calculated regression values and the RMS errors for the different correlations of TOC and velocity.

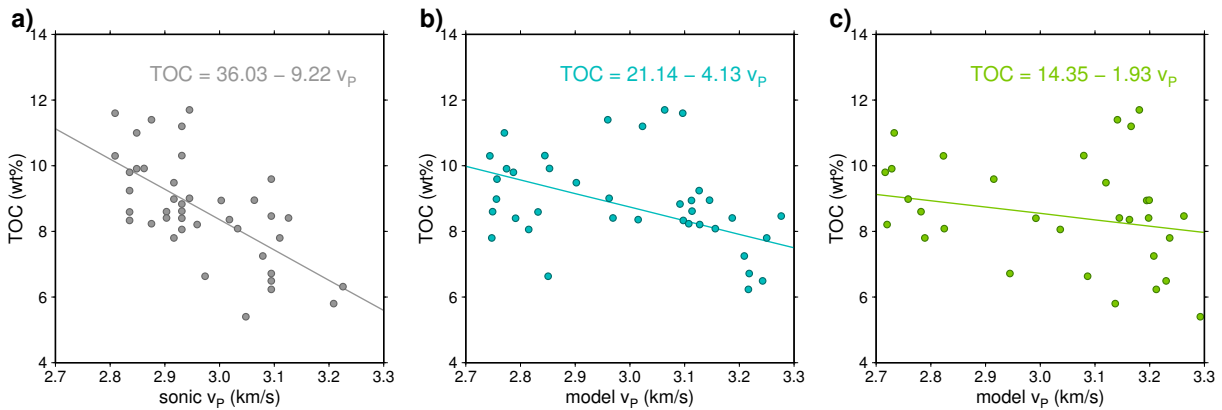


**Figure 3.20:** Correlation of TOC with sonic velocity (a) and tomography model velocities of Line-1 (b) and Line-3 (c). The result of the linear regression is inserted as a solid line and the regression formula is written in the top right corner of each plot.

The correlations with the tomography model velocities (Figure 3.20b,c) show a larger variance which is also reflected in the slightly higher RMS error (Table 3.3) compared to the correlation with the sonic velocity. The deviations from the linear trend marked by the regression line might be caused by scaling effects. The TOC content was measured on small scale black shale samples, whereas the travelttime tomography velocities were

derived on a larger scale. However, all correlations (Figure 3.20a-b) show the same trend of decreasing TOC with increasing P-wave velocity, but the slope of the curve is much larger for the correlation with the sonic log velocity compared to the correlation with the tomography model velocities.

The main aim of the correlation study is to use the correlation extracted from the borehole for the calculation of the spatial extension of the TOC content by applying it to the velocity data of the traveltime tomography profiles. If the correlation of TOC with sonic log velocity and the correlation with tomography velocity do not fit exactly, the TOC content will be over- or underestimated if the correlation achieved from the sonic log will be directly applied to the tomography model velocities. Figure 3.21 shows the estimated TOC values for the Alum Shale layer. Blue dots indicate the measured TOC contents of the Alum Shale samples. The blue lines are the TOC curves calculated from the velocities of Line-1 and inserted in green are the TOC curves calculated with the model velocity of Line-3. Solid lines indicate the values derived with the regression relationship of Line-1 and Line-3, respectively, and the dashed lines are the TOC values calculated with the regression formula of the sonic velocity correlation. It can be seen that the curves obtained with the correlations specific to Line-1 and Line-3 (solid lines) represent the true TOC trend much better compared to the curves where the sonic log velocity is the basis for the calculation of the TOC. Especially in the upper part of the Alum Shale, for the curve of Line-3 the TOC is overestimated when the sonic log calibration for the correlation is used (dashed green line) and the TOC is underestimated when the sonic log calibration is applied to the Line-1 velocities (dashed blue line). However, the trend of the distribution of TOC derived by the tomography models can be estimated also with a calibration only at the borehole location and will give a first impression of the hydrocarbon content in the black shale formation.

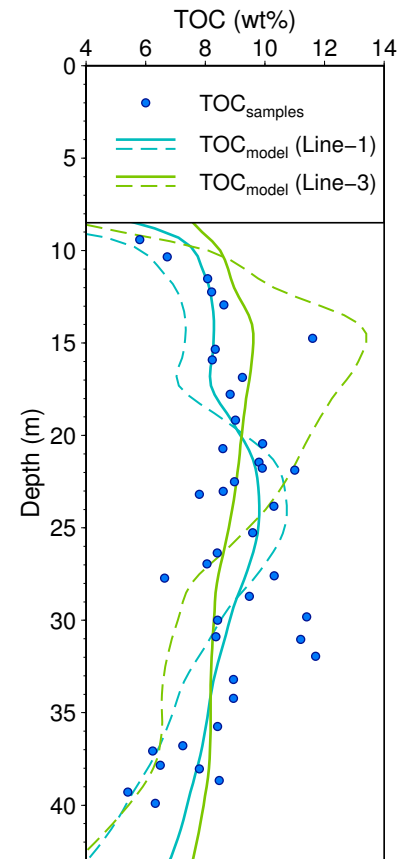


**Figure 3.21:** TOC values.

### 3.4 Discussion and conclusions

The weight drop data of the seismic experiments on Bornholm, which were used for the traveltime tomography, were of high quality. Therefore, it was possible to extract lots of traveltime data. The damped least squares inversion software `SIMUL` was used to obtain P-wave tomography models of the three seismic profiles. A graded inversion strategy was used to reduce the influence of the initial velocity model and to suppress inversion artifacts. Only few hyperbolic structures can be seen in the final tomography models which shows the positive effect of that technique on the tomographic results.

All three of the obtained P-wave velocity models image the different formations at the study location very well: The Komstad Limestone Formation on top, the Alum Shale Formation and the Læså Formation beneath. Even the thin bedded limestone layer at very shallow depth is well resolved and appears in the tomography results of Line-1 and Line-3. Although the Alum Shale is covered by the high velocity Komstad Limestone, the black shale velocities are determined very well which can be seen in the comparison of the vertical velocity profiles through the tomograms with the sonic log velocities. The black shale velocities of  $\sim 3$  km/s are also found in the laboratory study of Alum Shale samples (Chapter 6).

All derived tomography models match very well, especially the boundary of the Alum Shale and the Læså Sandstone Formation at the cross points. No anisotropy can be analyzed in the results, although it was expected to observe anisotropy effects of the black shale layer for the perpendicular aligned profiles. The seismic velocity of the Alum Shale seems, therefore, independent of the horizontal alignment of the profiles.

For the profile Line-3, which represents a connection between the two boreholes Skelbro-1 and Skelbro-2, a horizontal layering of the different formations is found. That is exactly what was expected from the stratigraphical analysis of both boreholes. No dipping is visible in east-west direction, but all layers are inclined to the south direction, which can be seen in the tomography model of Line-1.

In the P-wave velocity model of Line-3 the layer boundaries are not as clearly resolved as in the result of Line-1. Especially, the Komstad Limestone does not emerge as a continuous layer but is separated into small blocks of higher velocity compared to the black shale. At both outer edges of the velocity model of Line-3 the limestone layer is thickened to greater depths. Because the stratigraphy of Skelbro-1 (west edge of the profile) shows no extension of limestone to greater depth, the thickening in the model is assumed to be an inversion artifact. Possibly caused by the lesser ray coverage at the outer edges of the model, the high velocities of the limestone layer cannot be focused in the thin part of the model between 5 and 10 m depth but are smeared along the ray path.

In the west part of the model of Line-3 the limestone velocity is so low that it almost



cannot be distinguished from the Alum Shale. The further to the east, the higher are the Komstad Limestone velocities and the sharper the layer is separated from the underlying Alum Shale. Because the experimental setup is consistent throughout the whole profile with constant shot and receiver spacings, the ray coverage should be nearly symmetrical to the center of the profile. Changing velocities from west to east are, therefore, not caused by different ray coverage or different model updates but must have its cause in the formation itself. Hence, it can be assumed that a change in the limestone composition leads to increasing velocity from west to east.

The limestone shows higher velocities in the tomography model of Line-1 compared to the model of Line-3. The southward dipping of the layers benefits the imaging of the correct limestone velocity because the rays are mostly penetrating the limestone layer only once, whereas the rays in Line-3 must travel through the limestone twice, one time when going down and another time when coming up again. That means, the limestone can be better focused at the right position and with the right velocities during the inversion of Line-1. All in all, the P-wave velocity tomograms yield a good image of the subsurface in the region of the two scientific boreholes Skelbro-1 and Skelbro-2. The Alum Shale black shale layer is found at shallow depth and its regional extension is characterized by a southward dipping of the layer.

The comparison of the vertical velocity profiles at the Skelbro-2 borehole location shows differences in the upper part of the Alum Shale and for the Komstad Limestone. Why the limestone velocities are not reached in the tomograms, especially for Line-3, has just been discussed. Also the smoothness constraint of the inversion process plays an important role. Because of the smoothness of the model, sharp boundaries cannot be imaged and the high velocities of the limestone layer are smeared over a larger depth range. Thus, also the maximum value of that very thin limestone layer is underestimated. The smoothness constraint is also the reason that the small-scale inclusions of diagenetic limestone are not resolved by the models.

The fact that the high velocities are not reached for the limestone also yield velocities for the underlying Alum Shale which differ from the sonic log velocities. To reach traveltimes equal to the observed values, the traveltime tomography has to balance the part of the model around the incorrect estimated limestone layer. Therefore, the upper part of the Alum Shale directly beneath the Komstad Limestone shows higher velocities in Line-1. In the whole upper part of Line-3 the velocities are underestimated. That cannot be explained by a balancing of the velocities to get the correct traveltimes. Possibly, the overlying limestone layer already gives wrong ray paths during the ray-tracing process. That led to incorrect traveltime estimations and, therefore, incorrect velocities in this part of the model.

Imaging of low-velocity structures beneath high velocity layers is a great problem in geophysics. For traveltime-based inversion techniques like **SIMUL** it is particularly difficult to handle such velocity sequences with sharp boundaries because only the arrival times and no information of, e. g., phase or amplitude are used to resolve the velocity model. However, the resolved velocity profiles at the borehole Skelbro-2 are in accordance with the sonic log velocity trend. After a depth of 20 m the influence of the high velocity limestone layer has vanished and the true black shale velocities are reached for both models.

The information contained in the Alum Shale part of the P-wave tomograms can be used to obtain information about the content of organic carbon (TOC). With the achieved correlation of TOC and seismic velocity from the sonic log it is possible to extract the TOC content of the Alum Shale Formation at other locations by using the result of the seismic P-wave velocity tomography. However, an additional calibration with a drill hole at a new location would be recommended.

## 4 Surface wave inversion

### 4.1 Introduction

In reflection and refraction seismic surveys surface waves are mostly considered as noise and great effort is made to remove that high-energetic wave type. During the last years, ideas came up to use the information contained in the surface waves (Nazarian et al., 1983; Stokoe et al., 1994; Park et al., 1998). Surface waves are dispersive, that means each frequency travels with a different velocity (phase velocity) and, therefore, shows a different wavelength. Surface wave propagation is especially sensitive to the S-wave seismic properties of the shallow subsurface. The most common way to calculate the S-wave velocity profile is to use the dispersive nature of the fundamental mode of the Rayleigh wave (Bullen, 1963).

Nazarian et al. (1983) introduced a method called spectral analysis of surface waves (SASW). The method uses the surface waves generated by an impulsive source and recorded by a single pair of receivers. By rearranging the receivers and changing the receiver spacing, different frequencies can be measured. The data are then analyzed in the frequency domain and dispersion curves are calculated.

Because the use of only a single pair of receivers requires empirical criteria (Stokoe et al., 1994) which are sometimes difficult to achieve, the multichannel analysis of surface waves (MASW) was developed (Park et al., 1999). The MASW uses the information of a full seismic record with several receivers. Here, the dispersion curves are directly calculated from the multi-channel seismic data. The dispersion curves are then backcalculated to obtain a S-wave velocity profile.

In the early 1990s, methods using genetic algorithms were introduced (Sen & Stoffa, 1991; Sambridge & Drijkoningen, 1992) for the inversion of velocity ground models from observed dispersion curves. A technique belonging to the family of genetic algorithms called neighbourhood algorithm was developed some years later by Sambridge (1999). That direct search method searches the minima of the misfit function by investigating the whole parameter space. The misfit function is determined using Voronoi cells. Here a slightly modified version of the neighbourhood algorithm developed by Wathelet et al. (2004) was used for the calculation of 1D S-wave velocity profiles.

The analysis of the weight drop data showed that it was not possible to extract any

S-wave information. It would have been unproblematic to calculate a S-wave model with existing S-wave arrivals using the tomographic method described in Chapter 3, but this was impossible. For the characterization of seismic properties of black shales the analysis of both body wave types was needed, particularly to calculate the velocity ratio (Chapter 7). Therefore, the experiment using the minivibrator operating as SH-wave source was carried out. The refracted SH-wave of the vibroseis data was high-energetic and could be easily picked, but the individual profiles of 240 m were little too short for an appropriate tomography result giving only penetration depths of less than 15 m. Therefore, inversion of Love waves contained in the SH vibroseis data was considered as a good alternative to obtain a reliable S-wave velocity model. Dispersion curves were obtained for each of the source points of the vibroseis data by picking the maximum values of the calculated phase velocity spectrum. S-wave velocity models were then obtained by inverting the dispersion curves at each source point. All determined 1D S-wave velocity profiles were in good accordance throughout the whole investigated seismic profile showing increasing velocity with depth and a black shale S-wave velocity around 2 km/s.

#### 4.1.1 Dispersive nature of surface waves

Compared to body waves which travel through the whole subsurface, surface waves are only concentrated along the earth's surface. Most of the energy of a seismic event is concentrated in the surface waves. Therefore, these high-energetic waves can be easily recorded. There are two main types of surface waves, Rayleigh and Love waves. Rayleigh waves are a combination of transverse and longitudinal waves showing both horizontal and vertical particle motion. Love waves are horizontally polarized waves (SH-waves) that are bounded to a layered medium. In a homogeneous subsurface, no Love waves can be generated at the surface.

The amplitudes of both surface wave types decrease exponentially with depth, so that the penetration depth is often not larger than one wavelength. Correspondingly, waves with lower frequencies can penetrate much deeper. In many cases, increasing velocity with depth is found. Therefore, the lower frequencies which are reaching greater depths are traveling with a higher velocity. That behavior is called normal dispersion, giving the dependency of the phase velocity  $v$  with frequency  $f$ :

$$v = \lambda f, \tag{4.1}$$

where  $\lambda$  is the wavelength. When the velocity decreases with depth, reverse dispersion will be observed where the phase velocity then increases with increasing frequency.

To determine the dispersion curve of seismic data (curve of phase velocity as a function of frequency), the phase velocity spectrum has to be calculated first. Therefore, the seismic

data  $x(t)$  are transformed into the frequency domain using the Fourier Transformation of the form

$$X(f) = \int_{-\infty}^{+\infty} x(t) \exp(-i 2\pi f t) dt, \quad (4.2)$$

where  $X(f)$  denotes the data in the frequency domain after transformation. As the data were measured in a discrete form having discrete time samples, a discrete version of the Fourier Transformation can be used. Walker (1996) summarized the principles of the Fast Fourier Transformation (FFT) which is a simple and time-saving variant of Equation 4.2. After the transformation, the phase velocity spectrum  $p(v, f)$  can be calculated with

$$p(v, f) = \left| \sum_{x_{min}}^{x_{max}} \frac{X(f)}{|x(t)|} \exp\left(i 2\pi f \frac{x}{v}\right) \right|, \quad (4.3)$$

with  $x/v$  being the timeshift which is necessary to correct for the traveltimes due to increased offset.

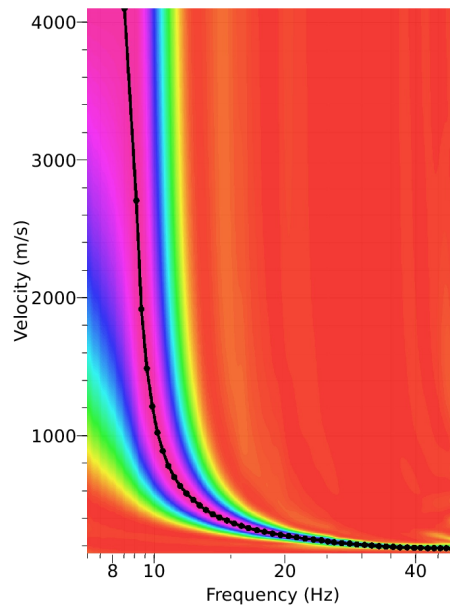


**Figure 4.1:** Phase velocity spectrum of the Love waves of the shot point at a distance of 564 m. The automatically picked dispersion curve (maximum of phase velocity spectrum) is plotted with the black line and dots.

If a frequency travels with a certain velocity, it results in a high value in the phase velocity spectrum due to constructive interference (Figure 4.1). The dispersion curve is achieved by picking the maximum values of the spectrum  $p(v, f)$  for all frequencies. The frequency dependent phase velocity curve (dispersion curve) is then representing the velocities of the shallow subsurface for high frequencies and deeper parts of the earth's interior will influence the low frequencies.

If several phase velocity maxima occur for a single frequency value, higher modes of the surface wave dispersion are found. Higher modes can also be included in the following inversion of dispersion curves but are neglected here, because the fundamental mode is dominant.

### 4.1.2 The neighbourhood algorithm

Many geophysical inverse problems are non-linear but can be solved by a linearization of the given problem using partial derivatives of the data with respect to model parameters (see Section 3.1). For some problems, the linearization fails or is computationally inefficient because the partial derivatives are difficult to calculate. That is the case, e. g., for the problem of the inversion of surface wave dispersion curves. One way to solve the problem is the usage of direct search methods like genetic algorithms, simulated annealing or the recently developed neighbourhood algorithm. All these methods are designed to find the minima of a misfit function by uniformly sample the whole parameter space.

Genetic algorithms were first used in computer sciences and later applied to geophysical problems (Sen & Stoffa, 1991; Sambridge & Drijkoningen, 1992). A genetic algorithm globally searches a model with the optimal data misfit value. The method of simulated annealing was first described by Rothman (1985, 1986). It is a stochastic direct search technique which was originally designed for global optimization problems. Recently, Sambridge (1999) introduced a new variant of direct search methods called the neighbourhood algorithm (NA).

The NA is a direct search method, where the parameter space is searched in a complex self-adaptive way (Sambridge, 1999). Not only the regions of the parameter space with acceptable data fit are considered, but also the information of bad-fitted data are used to construct the model space. A very important advantage of the NA is the usage of previous model space samples for the approximation of the misfit function everywhere in the model space. The misfit function is determined making use of Voronoi cells (Figure 4.2). The Voronoi cells are centered around the previous samples and define the nearest neighbourhood region using a suitable distance measure (e. g.  $L_2$ -norm). The misfit function of the previous samples is known and so a misfit surface is calculated by simply setting the misfit to a constant inside each cell. The size and shape of each cell is determined completely by the previous samples. The model space decomposition with Voronoi cells can be applied to all direct search methods.

Sambridge (1999) showed that the search in the parameter space is best performed with the Gibbs sampler (Geman & Geman, 1984; Rothman, 1986), where a perturbation to a model is generated and always accepted. An efficient search of the parameter space ensures the convergence towards a global solution (Wathelet, 2008). Due to the geomet-

rical properties of Voronoi cells, it is possible that the NA can jump out of local minima to quickly find a better solution. That is especially important for difficult inversion problems like the inversion of surface wave dispersion curves, where the misfit function has multiple minima.

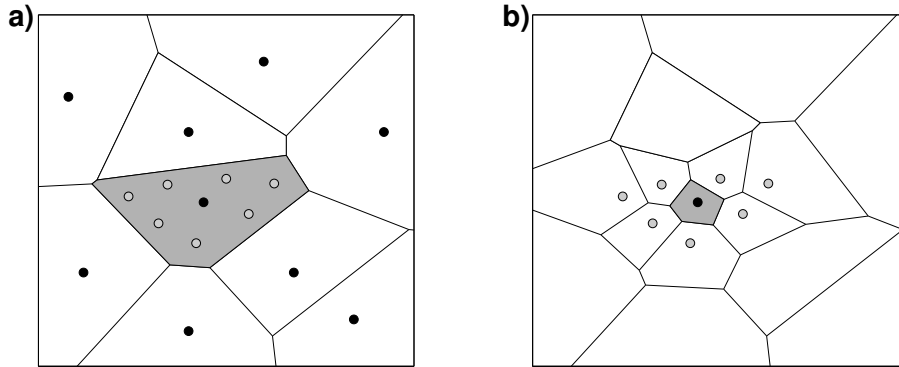


**Figure 4.2:** The development of the Voronoi geometry during the inversion. (a) The Voronoi cells of an ensemble of  $n_{s0} = 9$  models (black dots). For the  $n_r = 1$  cell with the lowest misfit value (shaded in gray) a total of  $n_s = 7$  new models are generated with the Gibbs sampler (light gray dots). (b) After including the new models, the Voronoi cells are re-computed. The sampling density around the lowest misfit region has increased as the sizes of the Voronoi cells decreased.

The original NA developed by Sambridge (1999) needs two parameters to control the inversion process and the computational efficiency. These control parameters are the number of generated models  $n_s$  and the number of cells  $n_r$  with the lowest misfit value. Wathelet et al. (2004) and Wathelet (2008) slightly modified the NA by introducing two additional tuning parameters: the number of total iterations  $it_{max}$  and the number of models  $n_{s0}$  chosen at the beginning of the inversion. So, the inversion process consists of five steps:

1. An initial set of  $n_{s0}$  models is (uniformly) generated in the parameter space.
2. The misfit function is calculated for the most recently generated modes.
3. The  $n_r$  models with the lowest misfit are determined.
4.  $n_s$  new models are generated by performing an uniform random walk (Gibbs sampler) in the Voronoi cell of each of the  $n_r$  chosen models ( $n_s/n_r$  models are generated in each cell).
5. the  $n_s$  new samples are added to the previous models and steps 2. - 5. are repeated till  $it_{max}$  is reached.

The new samples generated at each iteration are concentrated in the neighbourhood of the models with the best data fit (lowest misfit). While the inversion proceeds, the size of the Voronoi cells decreases due to an increase of the sampling rate (Figure 4.2).

## 4.2 Data processing and inversion

### 4.2.1 Processing of the SH vibroseis data

For the surface wave inversion, the Love waves contained in the SH seismic recordings of the vibroseis experiment were used (Section 2.2). The minivibrator was operated as S-wave source with vibration perpendicular to the W-E directed profile Line-3. Horizontal geophones were arranged in N-S direction, therefore, it was ensured that mainly SH-waves with N-S directed vibration were measured along the W-E profile. In some parts of the profile three component geophones were additionally deployed, where only the N-S component was used for the analysis of the Love waves. Ten sweeps were carried out at each of a total of 71 source points. The first six and the last six source points had a distance of 12 m, the rest of the sources were conducted every six meters. The minivibrator could be operated starting the vibration with a positive value either in the north or in the south direction. At each source position five vibrations were carried out starting with positive values to the north (+) and five vibrations were carried out starting with negative values to the north (-). That procedure has an advantage when stacking all vibrations at one shot point.

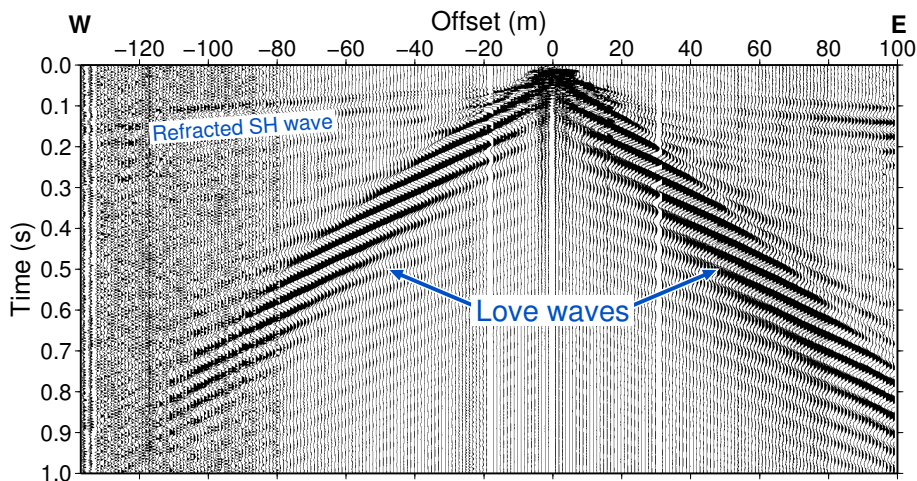


**Figure 4.3:** Example of the SH vibroseis data from the shot point at a distance of 378 m after processing. Clearly visible are the refracted SH-wave around 0.1 s and the strong Love wave which covers the complete time and distance interval.

The processing of the data was done with ProMAX®. As described in Section 3.2.1, a restitution filter was applied to correct for the different geophone types. Again, all ten



vibrations at each shot position were vertically stacked. But due to the special case of the different phases (+ and -) most of the P- and SV-wave information could be removed. This is possible because the P- and SV-wave arrivals show the same phase in both of the source arrangements. When the phase of the (-) measurements is changed by multiplying the data with -1 and then stacked with the (+) measurements, the already weak P- and SV-wave arrivals were fully removed. Due to the reverse behavior of the SH wave phases for the different phase configurations, the information of the SH waves was intensified by that kind of stacking.

After the vertical stacking the vibroseis data were correlated with the sweep signal of the minivibrator. The sweep length was 10s and the final correlated data (Figure 4.3) had a length of 2.5s with a 0.5s forerun for a better visibility of the first arrivals. For the analysis of the Love wave dispersion, the first arrivals were muted. These first arrivals were refracted SH waves and appeared as unwanted noise for the following calculation of the phase velocity spectrum. Additionally, noisy traces were removed from the seismograms. For each shot point a dispersion curve was then obtained by transforming the data into the frequency domain and calculating the phase velocity spectrum (Section 4.1.1). The maximum values of the phase velocity spectrum were picked automatically resulting in dispersion curves for a frequency range of about 15 to 50 Hz depending on the quality of the data. The obtained dispersion curves for each source point were then used as the input for the surface wave inversion.

### 4.2.2 Inversion with the neighbourhood algorithm

The inversion of the dispersion curves was carried out with the software `DINVER` (Wathelet, 2005, 2008) which is based on the neighbourhood algorithm (Sambridge, 1999). A great advantage of that method is, that no initial model is needed but the starting model is estimated from the data themselves.

In the first part of the inversion process, the calculated dispersion curves were loaded and, if necessary, treated further. Therefore, spikes were removed, the curves were cut to the desired frequency range and were smoothed. The dispersion curves were also resampled to a maximum of 100 frequency samples because more data points would have slowed down the inversion process dramatically.

The second part of the inversion was to define the model parametrization with the intended value ranges of P-wave velocity  $v_P$ , S-wave velocity  $v_S$ , density  $\rho$ , Poisson's ratio  $\nu$  and the depth of the individual layers  $z$ . That was the most important step of the inversion because the only influence on the final resolved models is possible by setting the parameter ranges. A priori information or previously acquired knowledge about the subsurface could be involved in the parametrization. The result of the traveltimes tomography of Line-3

was a good starting point for the inversion of the surface waves. The expected depth ranges of the different layers could be estimated from the P-wave velocity tomogram (see Figure 3.17).

The inversion itself was run in two steps. First, only one layer over a half-space was chosen to roughly estimate the dispersion curve and the corresponding ground profile. After that, the parametrization was expanded to recover the subsurface structure of five layers over a half-space. Wathelet et al. (2004) showed that this stepwise procedure is a good compromise between keeping the number of model parameters as low as possible and including all possible 1D structures of the complex measured data.

For the inversion of Love wave dispersion curves the P-wave velocity remained fixed at a relatively high value of  $v_P = 6$  km/s. Although no P-wave information was contained in the data, a P-wave velocity had to be chosen to stabilize the inversion process. It was fixed at such a high value to not fall into local minima (Wathelet, *pers. comm.*). The density was also fixed at a value of  $\rho = 2500$  kg/m<sup>3</sup>. Dispersion curves are not much influenced by the density (Wathelet et al., 2004), therefore, an average value for all depths was chosen. The Poisson's ratio was allowed to vary in a range of  $0.2 \leq \nu \leq 0.5$  but was chosen homogeneous for the complete depth range. S-wave models could then be constructed only for the given range of Poisson's ratio. The S-wave velocities were, therefore, restricted to vary between 0 and 3.67 km/s for the given P-wave velocity of 6 km/s.

Layer	Velocity $v_S$ in km/s	Depth $z$ in m
1	0.15 - 3.5	1 - 50
HS	0.15 - 3.5	

**Table 4.1:** Value ranges for the first inversion run. HS – half-space.

Layer	Velocity $v_S$ in km/s	Depth $z$ in m
1	0.15 - 3.5	1 - 10
2	0.15 - 3.5	5 - 20
3	1.5 - 3.5	10 - 30
4	1.5 - 3.5	20 - 40
5	1.5 - 3.5	30 - 50
HS	1.5 - 3.5	

**Table 4.2:** Value ranges for the second inversion run. HS – half-space.

The S-wave velocity is the parameter, which can be estimated very well from the Love

wave dispersion curve. Thus, only for the S-wave velocity different layers were assumed. The S-wave velocity and the thickness ranges for the first and the second run of the inversion are summarized in Table 4.1 and Table 4.2, respectively. The defined S-wave velocities were in a wide range leaving the possibility for the inversion routine to sample a large model space and to find the best-fit model. The depth ranges of the second run were chosen with an overlap of several meters. That enabled the inversion to have a smoother transition from one layer to the next.

Both runs were carried out one after the other for a total of  $it_{max} = 101$  iterations. The following control parameters were used:  $n_{s0} = 50$ ,  $n_s = 50$  and  $n_r = 50$  (see Section 4.1.2). Wathelet (*pers. comm.*) recommended to use values for  $n_s$  which are not larger than  $n_r$  to achieve the best exploration of the model space. When the two runs were computed, a total of 5100 velocity models had been calculated. The inversion process was then carried out with the same parameters for each of the 71 source points to obtain a two-dimensional S-wave model of the seismic profile Line-3.

### 4.2.3 The problem with low velocity zones

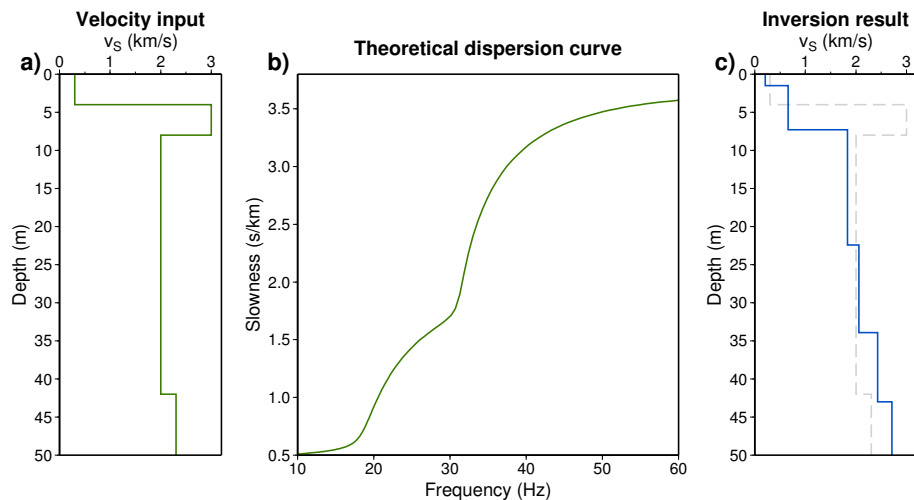


**Figure 4.4:** A simple  $v_s$  model representing the expected structure of Line-3 (a) was used to calculate a synthetic dispersion curve (b). That curve was then input for the inversion of the Love wave dispersion which resulted in the model shown with the blue line in (c). The high velocity layer between 4 and 8 m depth cannot be imaged with the Love wave inversion.

The result of the traveltimes tomography of Line-3 (Figure 3.17) has shown, that the Alum Shale Formation is overlain by a limestone layer with higher velocities than the black shale. Low velocity zones (here: black shale between limestone and sandstone) are a problem for the inversion of surface waves (Wathelet, 2008). The influence of that problem and whether such a thin high velocity layer at shallow depth can be resolved

by the surface wave inversion will be analyzed in this paragraph. Therefore, a synthetic S-wave velocity model was constructed with a high velocity layer on top of the black shale layer. It is depicted in Figure 4.4a. The dispersion curve for that model was then calculated (Figure 4.4b) and served as input for the surface wave inversion. The same control parameters and value ranges as for the inversion of the real data were used. The inversion result (blue line) is plotted in Figure 4.4c as well as the input model (dashed gray line). Both models show a great discrepancy at the shallow part of the profile. The high velocity layer is not imaged at all. Nevertheless, the black shale velocities are represented very well around the given value of 2 km/s. That means, although the high velocity layer cannot be resolved, the velocities of the underlying black shale layer are reliable.

### 4.3 Resulting S-wave velocity models

Following the inversion scheme described in Section 4.2.2, a total of 71 1D S-wave velocity models were calculated, one for each of the source points. The two left images of Figure 4.5 are showing all obtained dispersion curves and the corresponding ground models of one source point color-coded by their misfit value. Blue to magenta colors indicate insufficient resolution, whereas yellow and red lines are well resolved. It can be seen, that it was possible to fit the observed dispersion curve (black dots) very well. Also visible is, that lots of different ground models can be estimated with a very low misfit value and, therefore, a good fit to the data showing the non-uniqueness of the problem. Thus, no single model can be obtained as the best result. To achieve only one representative model for each source point, the models with the best fit to the observed dispersion curve were chosen to calculate an average model. Therefore, models with a misfit lower or equal than 150 % of the lowest observed misfit value were chosen. Due to that condition, a flexible number of models was used for the average calculation which prevented the influence of models with worse resolution. The average model of the example in Figure 4.5 is plotted as a red line in the right panel of that figure, underlain by all obtained velocity models in gray.

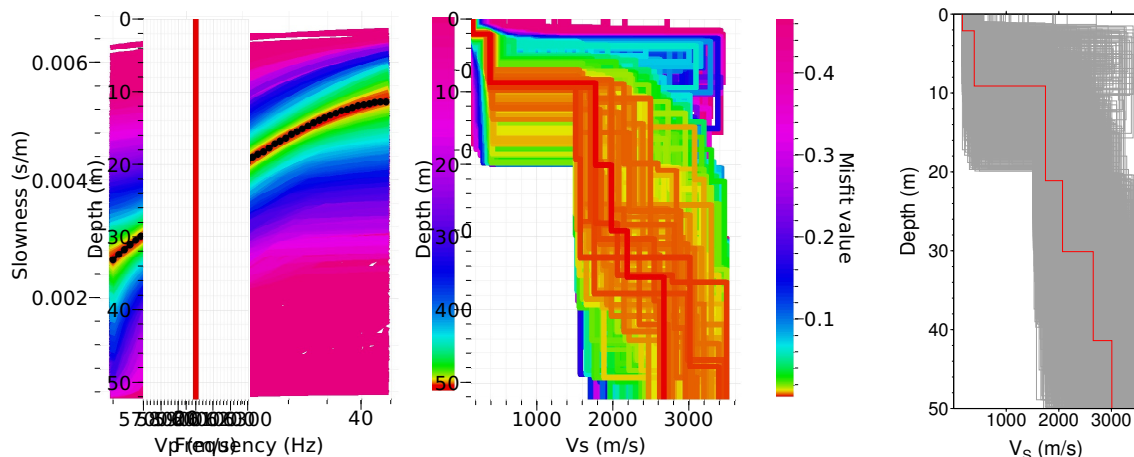
The 1D models can be assumed to represent the subsurface structure directly beneath the source point. That assumption is valid for horizontally layered strata which were found in the P-wave velocity model of Line-3 (Figure 3.17). The 2D structure can then be estimated by merging all 1D models to obtain a pseudo 2D model (see Ivanov et al., 2006; Socco et al., 2010).

Figure 4.6a shows the 1D models of all source points of Line-3 combined in one image. The source distance for the first and last six source points is larger (12 m) than for the rest of the profile (6 m), therefore, the bars of the velocity ground models are wider there. The fluctuations in the depth values of the individual block models are the consequence of

the relatively free parameter space with large overlap in the depth ranges. However, the models are rather consistent throughout the whole profile Line-3 and the velocities vary only little from one source point to the next. The different layers are clearly separated by their velocity values and each block model shows increasing velocity with depth. The dashed black lines inserted in Figure 4.6 are the contour lines separating the different formations found in the P-wave tomography model of Line-3 (Section 3.3.1). Due to the reasons discussed in the previous section, the Komstad Limestone layer is missing in the S-wave model. But the deeper boundary separating the Alum Shale and the Læså Sandstone Formation is imaged very well.

To better compare the derived S-wave model with the P-wave tomogram (Figure 3.17), the block model was interpolated using a surface gridding method and filtered with a Gaussian filter and 10 m window length. The filter was applied in a way that the sharp boundaries between the layers were removed but that not too much velocity information was lost. The smoothed velocity model (Figure 4.6b) gives a better impression of the real two-dimensional S-wave velocity distribution in the subsurface with increasing velocity with depth. The Alum Shale layer shows S-wave velocities between 1.7 and 2.5 km/s. The partitioning of the black shale in three different horizontal layers is still visible in the smoothed model. That seems to characterize the three different units of the Alum Shale Formation presented in the lithostratigraphy of Section 2.4.

The S-wave velocity model of the surface wave inversion along with the P-wave tomogram of Section 3.3.1 will be used to calculate the ratio of compressional and shear wave velocity at the profile Line-3 (Chapter 7).



**Figure 4.5:** Resolved dispersion curves (left) and models (center) of an example source point color-coded by the misfit function. Yellow to red colors highlight curves which are very well resolved. The black dots in the left image indicate the picked dispersion curve. An average model (red line in the right panel) was calculated from the best resolved models.

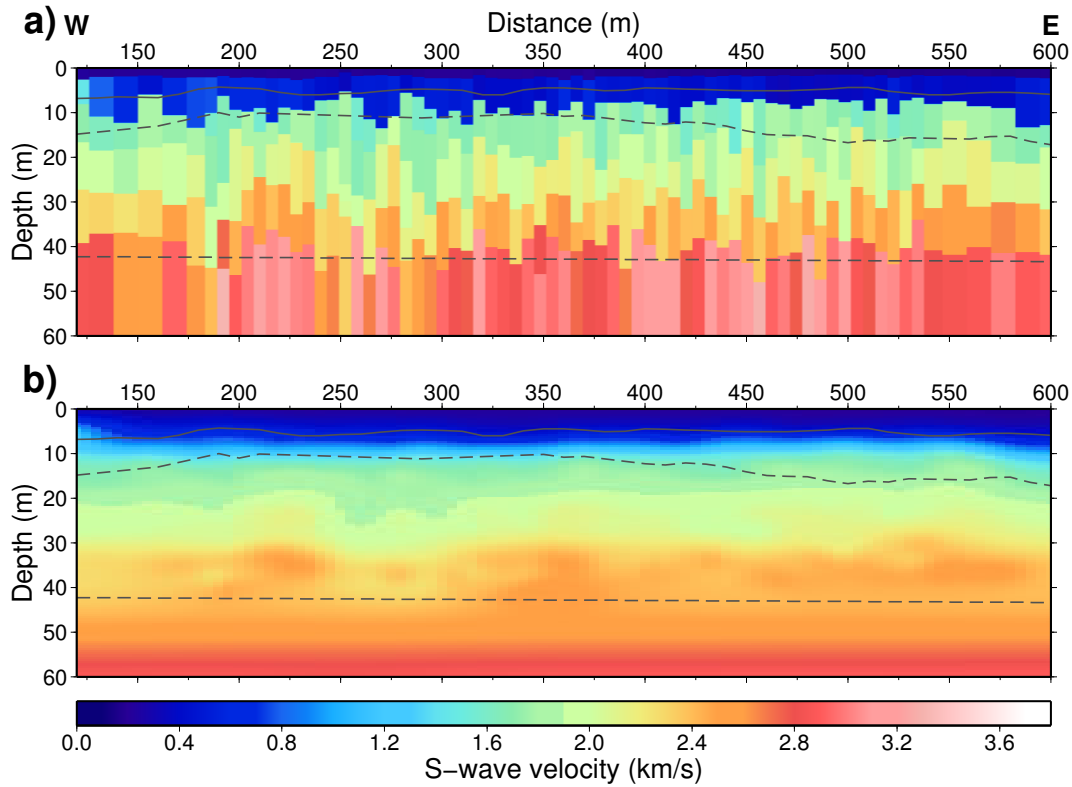


**Figure 4.6:** (a) The derived velocity block models of the Love wave inversion for Line-3. At each source location a velocity model was determined individually. All 1D models were then merged to the pseudo 2D S-wave velocity distribution of the subsurface. (b) The obtained S-wave velocity model after interpolation and filtering. Sharp boundaries were removed and the model shows a smooth increase of velocity with depth.

## 4.4 Discussion and conclusions

The SH vibroseis data clearly showed the occurrence of high-energetic Love waves. That surface wave type was strongly dispersive so the phase velocity spectrum could be calculated for each of the 71 source points. All spectra were picked automatically to obtain the dispersion curves. For each of the source points inversions were carried out individually and finally, 71 one-dimensional S-wave velocity models were determined.

The main difficulty of the problem was to properly define the inversion parameters. The more layers were defined, the larger the parameter space grew and the more difficult it was to optimally fit the data. There was the need to compromise between a good resolution of the dispersion curve and the simplest possible model. Therefore, two runs were carried out one after the other. In the first run, a two-layer model was chosen and in the second run the model consisted of five layers over the half-space. The layering for the second run was approximated from the P-wave model with overburden over the Komstad Limestone

followed by Alum Shale and Læså Sandstone Formation. The Alum Shale was divided into three different parts according to the lithostratigraphy of the borehole analysis of Skelbro-2.

All calculated velocity ground profiles were investigated to find the best resolved models. Therefore, only models with a very low misfit value were chosen to calculate an average velocity profile representing the structure directly beneath the source point. The non-uniqueness of the problem came out in the calculated velocity profiles with lots of models with low misfit values. But it was handled very well by the neighbourhood algorithm showing non-uniqueness only for the deeper layers.

The final results of the surface wave inversion show a clear separation of the defined layers by the amount of S-wave velocity. All models have increasing velocity with depth and the limestone layer with high velocities at shallow depth is not resolved in the final results. Some calculated models have resolved a ground model with a high velocity layer on top of the black shale layers, but the misfit value of these models is so high, that they are excluded from the estimation of the average model.

Throughout the whole seismic profile Line-3, the individual S-wave velocity models are very consistent and are expected to represent the two-dimensional underground structure at this location. The black shale velocities are found to be around 2 km/s. The bottom of that layer is imaged very well and is also in accordance to the boundary found in the travelttime tomography model of this profile.

The vibroseis experiment was also carried out with P-wave configuration. The Rayleigh wave contained in the P-wave seismograms could be useful to obtain more detailed and clear images of the subsurface by a joint inversion. The investigation of the Rayleigh wave dispersion was beyond the scope of this work, but it might be interesting for future studies. Also with regard to the possibility of resolving the limestone layer additional Rayleigh wave information would be helpful.





---

# 5 Seismic interferometry

## 5.1 Introduction

Using the ambient seismic noise to characterize the subsurface velocity structure is a relatively new approach. In geophysics, the basics for the technique called seismic interferometry were described by Claerbout (1968). But not till the turn of the millennium, seismic interferometry was extensively considered for the investigation of the subsurface velocity distribution (e. g., Weaver & Lobkis, 2001; Snieder, 2004; Wapenaar, 2004).

The aim of the analysis of ambient noise is to recover the Green's function between a pair of continuously recording seismic stations. The Green's function can be estimated by crosscorrelating the signals of the station pair under the assumption that the noise sources are uncorrelated, the sources are far from the stations and equally distributed in space and the noise is recorded for a sufficient long time period (Nicolson et al., 2011). The final calculated crosscorrelations (interferograms) can then be analyzed in the same way as *normal* seismograms of active seismic measurements.

In this chapter only a short overview of the method of seismic interferometry is presented. An exact theoretical derivation of the problem was beyond the scope of this work. For further interest the reader is referred to, e. g., Snieder (2004) and Wapenaar and Fokkema (2006).

The noise data used here was recorded only for a comparatively short time range of little more than one day along a profile of 700 m length. That makes this study very special and will characterize the very shallow part of the subsurface in the study area. Normally, seismic interferometry is applied when noise data collected over several weeks up to years is crosscorrelated (e. g., Saygin & Kennett, 2010). Thereby, also the station distances are much larger (several kilometers) than in the presented analysis. It is shown here, that the small scale and short term investigations also give acceptable interferograms. Also Scherbaum et al. (2003) showed that the application of seismic interferometry to a relatively small area is possible. They analyzed ambient noise data of a seismic array near Cologne, Germany.

Also remarkable in this study is, that the recorded noise was analyzed in different time windows and only high-quality time windows were then selected for the stacking of the final interferograms. This procedure considerably improved the signal-to-noise ratio of the

data and gave a hint about the sources of the recorded ambient noise field. It is shown that the main source of noise was caused by the traffic of the road which runs parallel to the seismic profile.

Only preliminary results of the crosscorrelations are shown in this chapter. Unfortunately, the data quality of the final interferograms was not good enough for further investigations like dispersion curve analysis and surface wave inversion. Figure 5.1 shows an example of a calculated phase velocity spectrum of one of the final interferograms. The maximum values are not easy to pick and no clear dispersive trend is visible. Compared to that, in the spectrum of the surface waves from the active experiment (Figure 4.1) a dispersion curve could be easily extracted.

However, the extracted interferograms show the potential to be a good enhancement or even an alternative to the active seismic data. The interferograms thereby cover a different depth and frequency range compared to the active experiments (see Chapter 7). Even P-wave arrivals emerge in the preliminary results presented here which will provide the opportunity for further processing.

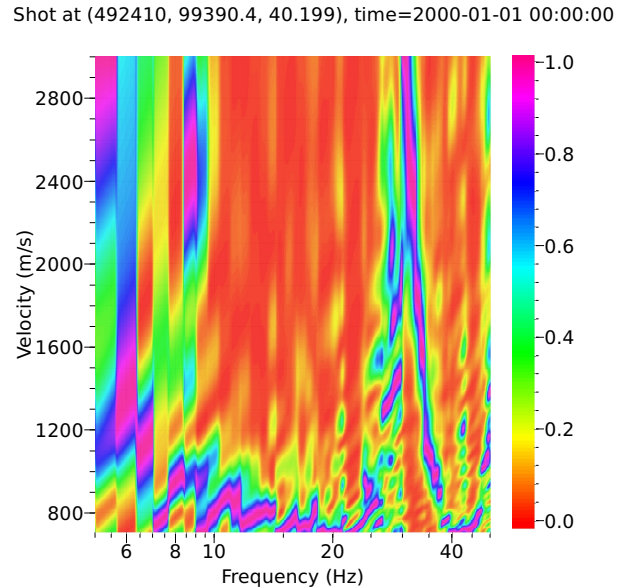


**Figure 5.1:** Phase velocity spectrum of an exemplary interferogram. No clear trend is visible and a dispersion curve is hard to pick.

## 5.2 Methodological background

For many decades, in reflection and refraction seismics much effort was made to remove unwanted noise from the seismograms to improve the signal-to-noise ratio. Nowadays, the ambient noise is not only treated as undesirable but is also used to extract information of the earth's subsurface. During the last years, the method of seismic interferometry evolved with the possibility to create useful signals from ambient seismic noise (e. g. Wapenaar, 2003, 2004; Campillo & Paul, 2003; A. Curtis et al., 2006; Bensen et al., 2007). Ambient seismic noise means seismic waves which are caused by wind, ocean waves, rock fracturing and anthropogenic activity (Nicolson et al., 2011).

The main principle of seismic interferometry is to crosscorrelate long time series of simultaneously recorded noise fields of two or more seismic receivers to extract the Green's function between pairs of receivers. The Green's function contains information of how

seismic energy travels through the subsurface from one receiver to the other.

That principle was first described by Y. W. Lee (1960) who estimated the response of a linear system by crosscorrelating the input and the output signals while the system was excited with white noise. The geophysical analog was demonstrated by Claerbout (1968) who showed that the reflection response can be obtained directly by the autocorrelation of the transmission response of the earth. Claerbout (1968) assumed that if the noise recorded at two receivers is crosscorrelated, a signal could be constructed which would be equal to the signal of one of the receivers if the other had been a source. Claerbout's conjecture was then proven years later by, e. g., Rickett and Claerbout (1999) in the context of helioseismology. In an ultrasonic experiment, Weaver and Lobkis (2001) measured thermally induced random waves at two receivers on a granite block. The crosscorrelation of the signals of both receivers was found to be the elastic impulse response (Green's function) between both receivers. Wapenaar (2004) derived a proof of Claerbout's conjecture with the reciprocity theory. For uncorrelated noise sources he found, that the impulse responses between a station pair reduces to the crosscorrelation of the signals at the two receivers.

Seismic interferometry consists of two fundamental steps: (1) crosscorrelation of the noise signal of two receivers for a given time interval to detect the travelttime difference of the recorded signals between the two receivers and (2) stacking of the signals over the time intervals to improve the signal quality. For two stations/receivers at  $x_A$  and  $x_B$  the crosscorrelation can be calculated as follows:

$$\frac{\partial}{\partial t} G(x_A, x_B, t) = \int_{-\infty}^{+\infty} u(x_A, \tau) u(x_B, t + \tau) d\tau, \quad (5.1)$$

where  $u(x_A, t)$  and  $u(x_B, t)$  are the continuously recorded seismic velocity fields of the receivers at  $x_A$  and  $x_B$ . The result of the crosscorrelation operation (Equation 5.1) is the time derivative of the sum of the Green's function between the two receivers and its time reversed image (Snieder, 2004). Therefore, to construct the true Green's function, a frequency dependent amplitude correction has to be applied. Due to the differentiation in time, there also exists a phase shift between the result of the crosscorrelation of the two signals and the true Green's function. To analyze, e. g., the phase velocity information of constructed surface waves, a correction for the phase shift needs to be applied (Saygin & Kennett, 2010).

Without the application of the above mentioned corrections, the derived crosscorrelation will still be a good approximation of the impulse response (Green's function) between the pair of receivers (Wapenaar, 2004; Manen et al., 2006; Wapenaar & Fokkema, 2006). That is valid providing that the noise sources are uncorrelated, the sources are far from the receivers, evenly distributed in space and the noise is recorded for a sufficiently long

time period (Nicolson et al., 2011).

The result of the crosscorrelation can be termed a seismogram of a *virtual* (imaginary) source at the location of one of the receivers. That seismogram can be processed using traditional seismic techniques and can also be used for the imaging of the subsurface with tomographic methods like *normal* seismograms. The first application of tomographic velocity inversion of virtual seismograms extracted by seismic interferometry was described by Shapiro et al. (2005) and Sabra et al. (2005). They analyzed the surface wave components of the crosscorrelations of many pairs of stations in the California region and used the dispersive character of that wave type to obtain velocity maps.

Caused by the nature of the noise sources, Rayleigh waves tend to dominate the inter-receiver Green's function (Saygin & Kennett, 2010), therefore, the analysis of the surface wave part is the most common technique in recent years. However, it is also possible to extract P-wave information of the Green's function (or its approximation) when the receivers are closely spaced (Roux et al., 2005).

### 5.3 Data preparation

At the location of the third seismic profile (Line-3), additional noise records were conducted during the field campaign in June 2012. Therefore, at the 61 shot locations of the weight drop experiment (Section 2.2) the stand-alone seismic recorders (GFZ-Cubes) were positioned with the first station at the west end of the profile. They recorded the ambient noise field for a time period of 28 hours from a Sunday noon on. Only the vertical component of the wave field was measured and the noise recorders also ran during the active weight drop experiment.

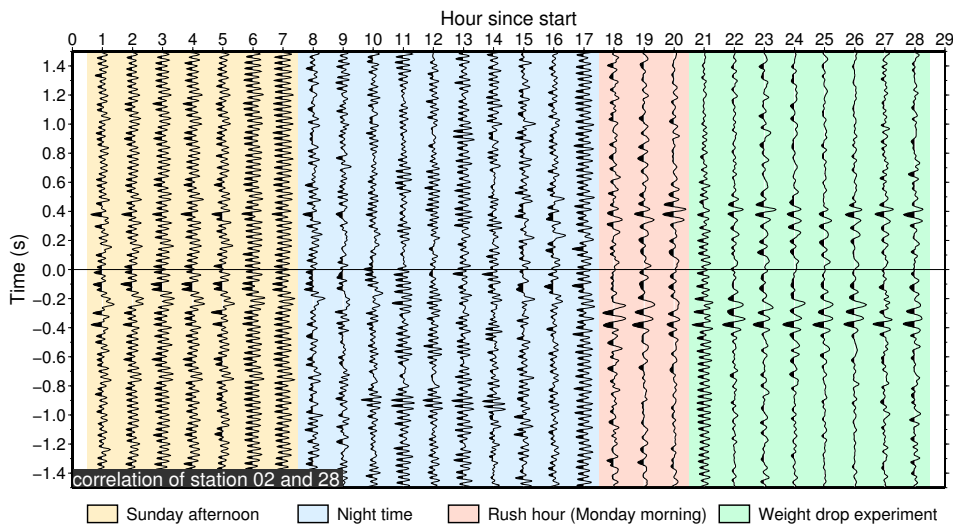


**Figure 5.2:** Trace-normalized and bandpass filtered crosscorrelation of station 2 with station 28 plotted by the hour after the beginning of the noise experiment at Sunday noon. Till the hour 17 the data quality is insufficient for stacking, but from hour 18 on, the data can be stacked for higher quality interferograms.

The data of the continuously running noise measurements were cut in sections of one hour window length. The bias was removed by subtracting the average amplitude value of each time window from the data. Time or temperature shifts were diminished by applying a bandpass filter with a large bandwidth (0.01 - 100 Hz), where only very low and very high frequencies were eliminated. To reduce the influence of large amplitudes from earthquakes or the nearby traffic noise, the data were one-bit normalized (Campillo & Paul, 2003; Larose et al., 2004; Shapiro et al., 2005). Thus, only the sign of the wave field was used for the subsequent crosscorrelation. Campillo and Paul (2003) showed that one-bit correlations will give better results with higher final signal-to-noise ratios compared to the correlation of the data without one-bit normalization.

Crosscorrelations were then calculated in the given time window of one hour for each of the station pairs. For the final interferograms the single crosscorrelations were stacked over the time windows. An example of the crosscorrelations of a station pair showing all individual time windows is depicted in Figure 5.2. The examination of the individual time windows and their noise signal content was very important for the evaluation of the quality of the data after the subsequent stacking.

Great differences can be seen for the different times of the day (different colors in Figure 5.2). At Sunday afternoon (yellow) and during the night time (blue) the noise is quite uncorrelated and a definite signal is hard to detect. From the 18<sup>th</sup> hour on the crosscorrelations show a good signal around  $\pm 0.4$ s. Interestingly, hardly any difference can be observed between the correlations directly before (red) and during the active weight drop experiment (green). Normally, the source of the noise measurement was expected to be very far away from the recording stations. But that would have resulted in equally looking crosscorrelations for all time windows. That brings up the assumption that the nearby traffic was the main cause for the clear noise signatures and shows that not only sources far away from the stations led to acceptable correlations.

The road was aligned parallel to the recorder line, which is favorable for the contribution of the traffic noise to the final noise signals. The cars passed the recorders one after the other only in E-W direction. Therefore, the originally 3D problem was reduced to an almost 1D case.

If all time windows were considered, the stacked crosscorrelations for, e.g., station 30 in the center of the profile, were very noisy (Figure 5.3a). Only the air wave emerged with a clear signal. Surface waves or body waves were not visible or showed only weak signals. If now the correlations were stacked only from hour 18 on, the signals in the interferogram became much clearer and the uncorrelated noise was reduced (Figure 5.3b). But it can also be seen that a large amount of energy is concentrated in the air wave. The air wave showed higher frequencies compared to the useful signals of the surface wave or the body wave. To remove the high-frequency noise from the interferogram, a bandpass filter was

applied with a passband from 2 to 20 Hz. The resulting interferogram after filtering is plotted in Figure 5.3c. The air wave completely vanished and the surface wave information was considerably intensified. Even P-wave signals can be seen in the right part of the figure around 0.2 s.

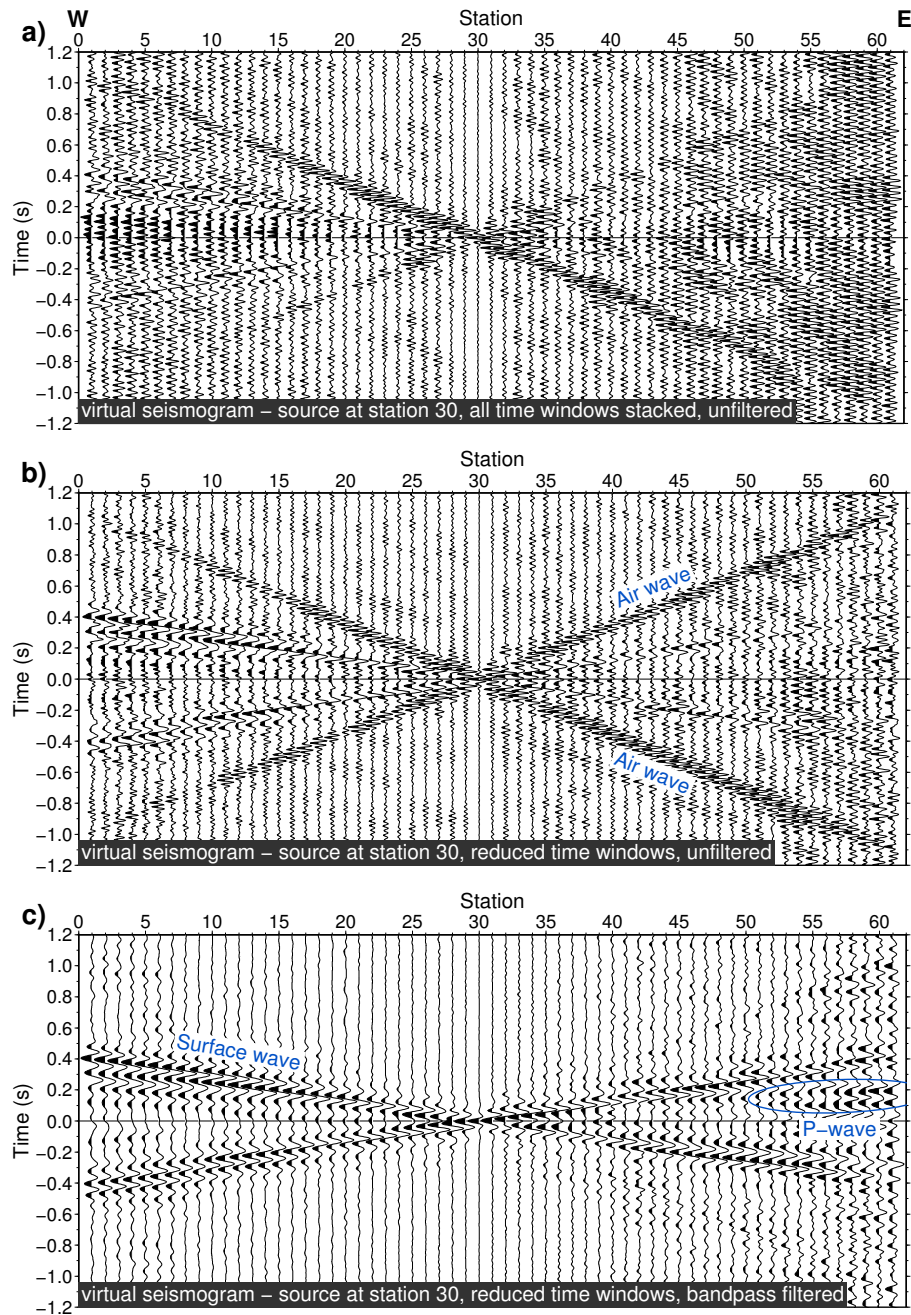


**Figure 5.3:** Interferograms after the different steps of data preparation: (a) When all time windows are used for the stacking, the interferogram is very noisy showing hardly any correlation. (b) Using only the last hours of registration lead to a higher signal-to-noise ratio, but the air wave is dominating the interferogram. (c) After applying a bandpass filter (2 - 20 Hz), the air wave is completely removed and surface wave and P-wave signals become visible.



## 5.4 Extracted interferograms

Figure 5.4 shows the interferograms (all crosscorrelations of one station with all the other stations) of both edges of the profile to illustrate differences along the seismic profile. The signals for station 1 (Figure 5.4a) are very clearly displayed whereas the noise level is increased in the interferogram of station 61 (Figure 5.4b). Also the air wave becomes visible in the data of station 61. The deterioration of the data quality from station 1 to station 61 (from west to east) is observable in the complete data set where the eastern edge of each interferogram shows a lower signal-to-noise ratio compared to the rest of the seismic section.

Both interferograms in Figure 5.4 show no symmetrical behavior of the signals but higher amplitudes are visible for negative times at station 1 and for positive times at station 61. Therefore, the noise is not assumed to be evenly distributed around the stations but has a main direction coming from east to west (see, e. g., Snieder, 2004). That means, the main noise is first passing station 61 and then station 1.

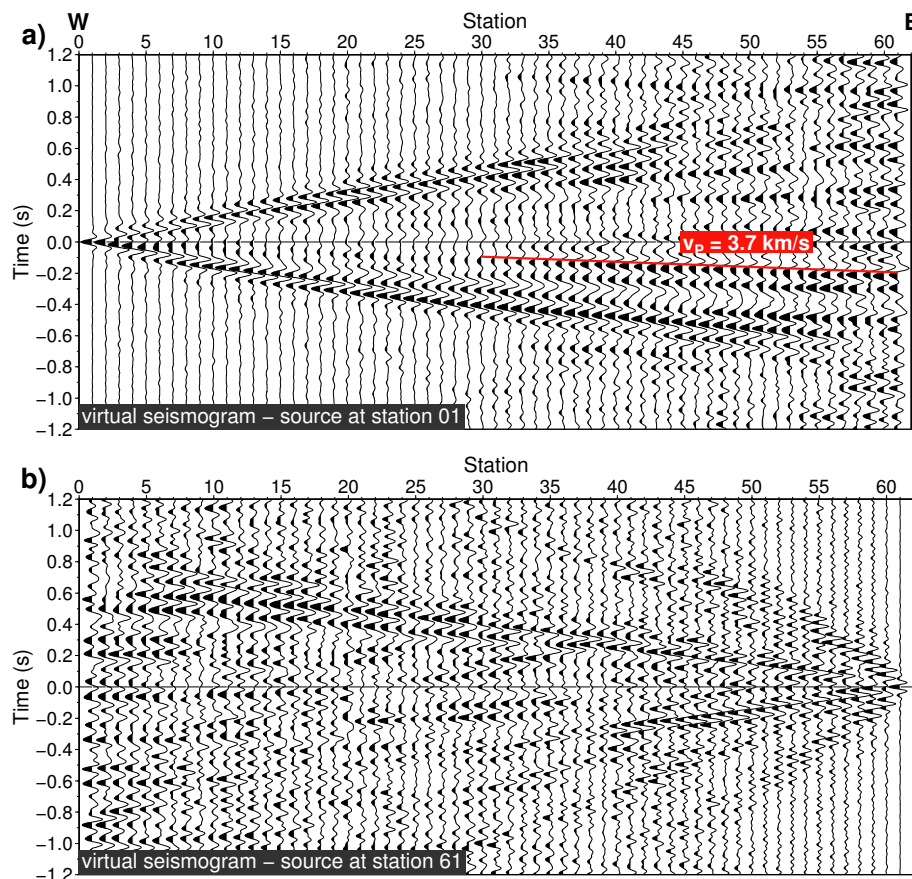


**Figure 5.4:** Final interferograms of station 1 (a) and station 61 (b). The signal-to-noise ratio is considerably lower for the station at the eastern edge of the profile (station 61). Besides the surface waves also a P-wave arrival is observable for station 1 with an apparent velocity of 3.7 km/s.

Because of the small station distances (12 m), P-wave arrivals are observed (Roux et al., 2005). For station 1, they have an apparent velocity of 3.7 km/s (Figure 5.4a). In addition to the P-wave arrivals at station 1, also the other stations were investigated according to the P-wave content. Almost all interferograms show strong or less strong P-wave signals. The signal quality of the P-wave signals also decreases from west to east like the overall quality of the data. Furthermore, for the interferograms of different stations different apparent velocities are observed. Figure 5.5 shows the interferograms of station 3 and station 5 with the identified P-wave arrivals and the corresponding apparent velocities. The images reveal a decrease of the apparent P-wave velocity from 3.4 to 3.1 km/s with increasing station number.

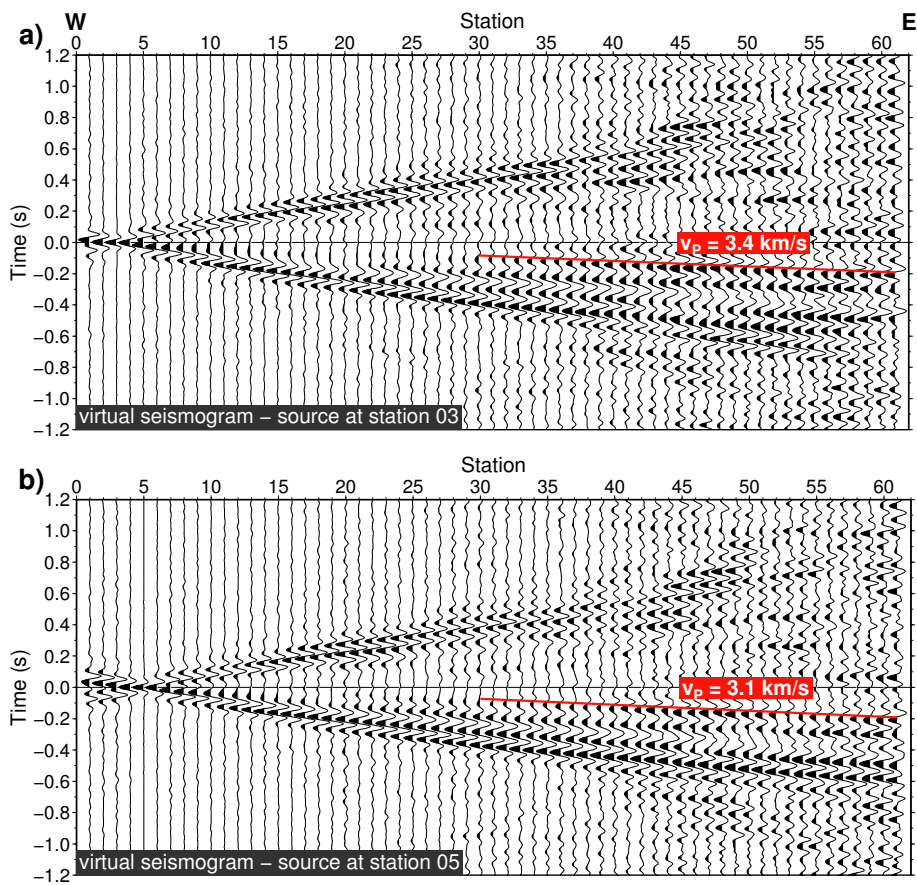


**Figure 5.5:** In the interferograms of station 3 (a) and station 5 (b) the P-wave arrival shows different apparent velocities of 3.4 km/s and 3.1 km/s, respectively, also compared to the interferogram of station 1 (Figure 5.4a).

In the interferograms, the crosscorrelations of one station with all the other stations are summarized in a way that they are comparable to the active weight drop experiment. The interferogram of one station corresponds to the seismogram of the source point at the location of that station. A comparison of the interferogram of station 1 and the data of the weight drop source at this location is plotted in Figure 5.6. The data of the weight



drop experiment was bandpass-filtered in the same way as the crosscorrelations (passband 2 - 20 Hz). However, the seismogram (blue-to-red image in Figure 5.6) seems to contain higher frequencies than the interferogram (black wiggles).

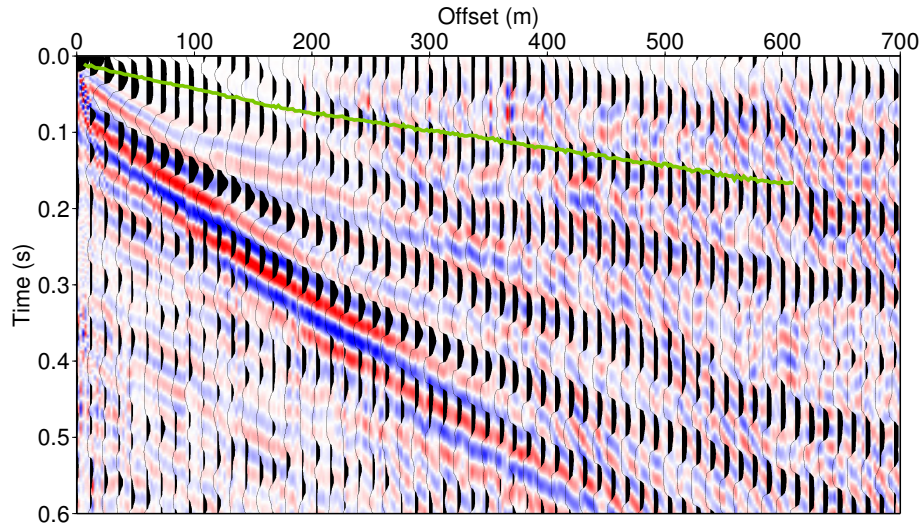


**Figure 5.6:** Comparison of the interferogram of the first station (black wiggles) and the seismogram of the first shot of the weight drop experiment at the profile Line-3 (blue-to-red image). The seismograms match really well and the interferometry of passive seismic data can be assumed to produce seismic wave information consistent to the active experiment. Even the arrivals of the P-wave identified in Figure 5.4 are in accordance to the picked first arrivals of the weight drop profile of Line-3 (green line).

The phases of the surface waves match quite well, although the surface waves in the interferogram show a higher apparent velocity. But the surface waves in the noise records have a higher signal-to-noise ratio and are visible throughout the entire data set, whereas the surface wave energy in the weight drop data is decayed after an offset of 500 m.

The P-wave arrivals of the noise correlations are in good agreement to the weight drop data. Strong near-field effects in the noise recordings impede to reveal the first arrivals up to an offset of 250 m. After that distance, the picked traveltimes for the tomographic inversion (green line) are nearly identical to the P-wave arrivals in the interferogram.

All in all, the comparison confirms the assumption that the crosscorrelation of the noise recordings of one station with all other stations equals the seismic data if that one station had been a source. That means, although the sources of noise were close to the recorders and not equally distributed around the stations, the interferograms presented here are a reliable estimation of the Green's function.

## 5.5 Discussion and conclusions

In the analysis of the crosscorrelations of ambient noise presented here, a new approach considering a very small scale was used which was not often applied before. The noise field was recorded in a very short time interval, whereas normally large time ranges of up to several years were investigated. The recorded noise data was separated into time windows of only one hour length. The crosscorrelations were calculated for each individual time window and then stacked. In this work, only the time windows with sufficient signal-to-noise ratio were chosen before the stack was carried out. That is a special procedure which was not done in previously described works about seismic interferometry.

A correlation was found between crosscorrelations showing a high signal-to-noise ratio and the occurrence of traffic. That means, the traffic noise was assumed to be the main cause for the signals in the interferograms. The road running parallel to the recorders reduced the 3D problem of seismic interferometry to an almost 1D case, which might also be the reason that the crosscorrelation of the nearby traffic noise gave accurate results. The noise field was identified to have a main direction coming from east to west.

When traffic is considered the main cause of the noise correlations, then the decreasing signal quality to the east might be caused by the elevation of the profile. In the eastern part of the profile a small knoll probably shields the noise field to the west. In the western part, the terrain is very flat allowing more consistency in the noise field and, therefore, better correlations.

Due to the very small station distances along the profile also P-wave arrivals are observed. The determination of P-wave information from the interferograms seems to be difficult because the apparent velocity of the P-wave arrivals significantly varies from one station to the next. The analysis of body wave signals in seismic interferograms may be a subject for further investigations along with the examination of the surface wave signals by ambient noise tomography.

All in all, it is particularly remarkable that seismic interferometry is possible and that the Green's function can be accurately estimated with this kind of recordings, where only a small area and a very short time range were considered.

## 6 Laboratory analysis

### 6.1 Principles of ultrasonic measurements

The purpose of this part was to determine the seismic velocities under different pressure and temperature conditions and to examine the anisotropy of black shale samples on a laboratory scale. There are only few laboratory studies relating shales in the literature. That might be because of the low permeability of shales, the difficulty in handling and their structural and compositional complexity (D. H. Johnston, 1987). Shales are by nature anisotropic (Jones & Wang, 1981). Velocity and anisotropy of shales strongly depend on the clay and kerogen composition (Meissner, 1984) and the bulk density (Jones & Wang, 1981). Both are influenced by interactions of pore fluids with the clay matrix (D. H. Johnston, 1987).

Ultrasonic velocity measurements were performed using the pulse transmission technique (e.g., Birch, 1960). Therefore, shale samples were plugged between a transmitting and a receiving transducer and the traveltime between both transducers was recorded.

Ultrasonic waves were generated using the piezoelectric effect. The arrangement of atoms of piezoelectric crystals can be changed under pressure or tension (Figure 6.1). The previously neutral crystal is then behaving as a dipole and electrical charges occur at the surface of the crystal. If contraction and expansion are interchanged, the charges at the surface change their sign. Therefore, an alternation of contraction and expansion generates an alternating voltage. The piezoelectric effect is reversible (inverse piezoelectric effect). That means, that an alternating voltage applied to a piezoelectric crystal results in oscillations of the crystal, which then emits seismic waves.

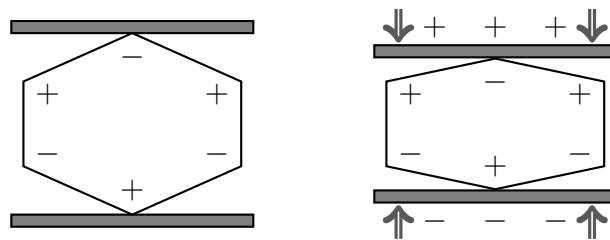


**Figure 6.1:** Changing of the distribution of charges in between a piezoelectric crystal (here: quartz). After contraction of the crystal, the atomic charges are no longer balanced and charges at the surface of the crystal occur.

## 6.2 Ultrasonic measurements

### 6.2.1 Sample preparation

The black shale cores of the Alum Shale Formation on Bornholm were obtained during the drilling of the Skelbro-2 well in August 2010 (Section 2.4). Between a depth of 5 and 43 m, a total of 14 core sections (Bo-AS-K1 to Bo-AS-K14) were extracted. To preserve the in-situ conditions, the cores were vacuum-sealed directly at the drill site.


Parts of the cores Bo-AS-K3 and Bo-AS-K7 (Figure 6.2) were provided for the seismic experiment. They were extracted from two different units of the Alum Shale (Lower Ordovician and Furungian). It was necessary for the ultrasonic measurements, that the samples had a diameter of 30 mm. Therefore, the samples had to be plugged from the core material. It was extremely difficult to get samples, because the cores were already broken or broke during the drilling with the diamond drilling head. Cores were taken both parallel and perpendicular to the bedding. It was especially challenging to get samples with orientation perpendicular to the core axis which also were long enough for the ultrasonic measurements later on. The minimum sample length had to be 40 mm. For shorter samples it was hardly possible to record the S-wave signal due to interferences with reflected P-wave signals. The ends of the samples were smoothed to achieve the best possible coupling between the transducers and the sample.

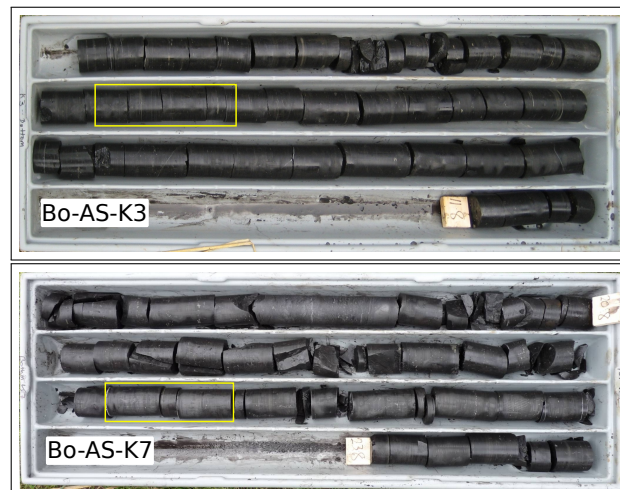


**Figure 6.2:** The full extracted cores Bo-AS-K3 (top) and Bo-AS-K7 (bottom). Highlighted with a yellow rectangle are the parts, which were provided for the seismic velocity measurements. © Tobias Meier, GFZ Potsdam

Finally, four black shale samples could be extracted, two of each core with perpendicular orientation. Table 6.1 summarizes the length, corresponding depth and unit of the Alum Shale of the extracted samples, in which axial means samples for wave propagation perpendicular to the bedding and radial means wave propagation parallel to the bedding. The orientation of the different sample types is illustrated by the sketches in Table 6.1.

Sample	Axial Length (mm)	Radial Length (mm)	Corresponding depth (m)	Corresponding stratigraphy
Bo-AS-K3	44.86	44.52	10.5	Ordovician AS
Bo-AS-K7	56.60	44.70	23.5	Furungian AS



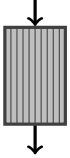


**Table 6.1:** Measured length of all black shale samples according to the direction of layering. For axial samples the wave propagation will be perpendicular to the bedding and for the radial samples the wave propagation will be parallel to the bedding. Additionally, the depths which are corresponding to the extracted samples and their stratigraphical unit are written in the right column (AS – Alum Shale).

### 6.2.2 Experimental setup

A simplified illustration of the experimental setup is plotted in Figure 6.3. The pulse generator (Agilent Technologies) generated an electric impulse with a specified frequency. The electric signal was transformed in the transmitting transducer using the piezoelectric effect and a seismic wave in the ultrasonic frequency range was transmitted into the sample. The receiving transducer transformed the seismic waveform back into an electric signal. That signal was then recorded by the oscilloscope and was directly displayed. With the oscilloscope, the seismic signal could first be optically analyzed and was later saved as ASCII file to a USB flash drive.

To obtain seismic signals for different pressures and temperatures, the samples (Figure 6.4a) were plugged in a pressure vessel filled with edible oil. Therefore, the samples needed to be 30 mm in diameter to fit the diameter of the transducers. Both sample and transducers were then sealed with a shrinking tube to prevent infiltration of the oil. During the measurements, the coupling of sample and transducers was achieved only by the confining pressure. The temperature was controlled with a temperature sensor, which was connected to the measuring unit consisting of the sample and both transducers (Figure 6.4b). The measuring unit was carefully bolted into the pressure vessel and connected to the pulse generator and the oscilloscope (Figure 6.4c).

The measurements were achieved under different pressure and temperature conditions. For a measurement, one parameter (pressure or temperature) should remain fixed, whereas the other was systematically decreased or increased. Therefore, the first parameter also had to be adjusted to achieve the expected conditions. After a short time, an equilibrium was reached and the recordings could be carried out.

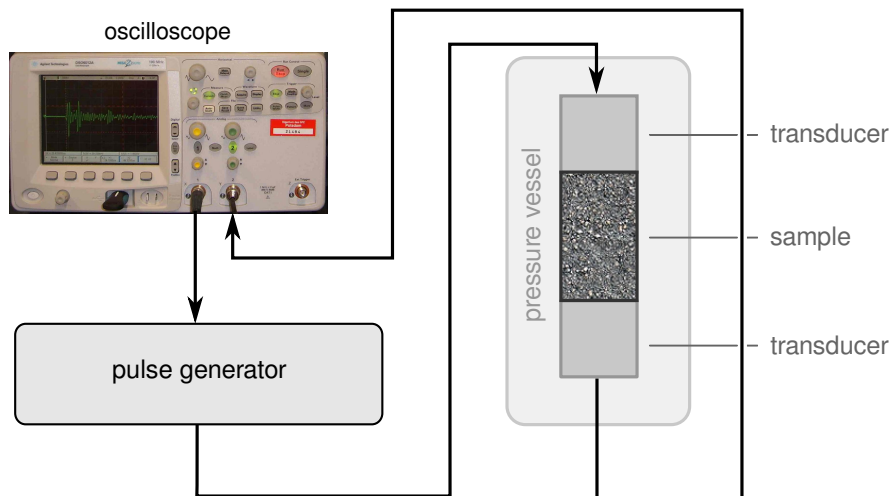


**Figure 6.3:** Schematic setup of the ultrasonic measurements. The pulse generator transmits an electric impulse, which is transformed in the transducer. The transducer is then transmitting seismic waves with ultrasonic frequency into the sample. The signal is again transformed in the receiving transducer and visualized by the oscilloscope.

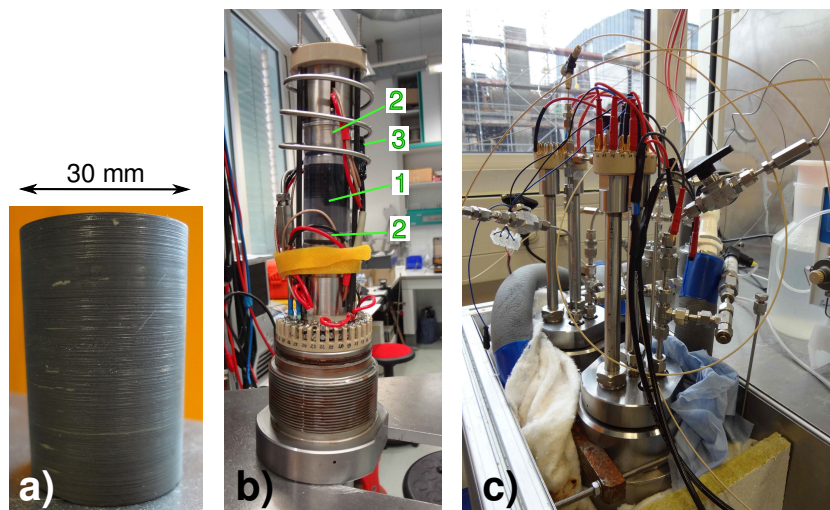


**Figure 6.4:** (a) Example of a black shale sample. All samples had to be 30 mm in diameter to fit into the ultrasonic measuring unit. (b) The sample (1) and the transducers (2) in the measuring unit. Both are embedded in a shrinking tube to prevent infiltration of the oil of the pressure vessel. A temperature sensor (3) is also included for  $1/100^\circ\text{C}$  exact temperature measurements. The measuring unit is shown after disassembling, therefore, oil ingressed between sample and shrinking tube. (c) The measuring unit plugged into the pressure vessel.

For all samples, a pressure cycle at room temperature ( $\vartheta = 20^\circ\text{C}$ ) was conducted, where the pressure was first increased from 2 MPa to 40 - 50 MPa with an interval of 2 MPa and immediately afterward decreased to the starting value. Additionally, for both samples of Bo-AS-K7 a second pressure cycle was carried out at a temperature of  $\vartheta = 80^\circ\text{C}$  in the same pressure interval as for the first pressure cycle. The measurements depending on the temperature were conducted at constant pressure of  $p = 12$  MPa for the samples of Bo-AS-K3 and  $p = 2$  MPa for the samples of Bo-AS-K7. The higher pressure value for the Bo-AS-K3 samples was necessary, because the P-wave arrivals at lower pressures were too weak to be picked exactly. The temperatures have been increased from 20 to  $80^\circ\text{C}$ .

### 6.2.3 Wave recordings

Only one emitted ultrasonic impulse would have resulted in a relatively noisy seismogram. Therefore, a total of 256 impulses was stacked for every wave recording. That was done automatically by the oscilloscope. The transmitted frequency was 1 MHz and the waves were recorded with a sample interval of 0.05 and  $0.1\ \mu\text{s}$  for P-wave and S-wave, respectively. When stable conditions of pressure and temperature were reached, the ultrasonic seismograms for the P-wave transducer and the S-wave transducer were written to disk in separate files.

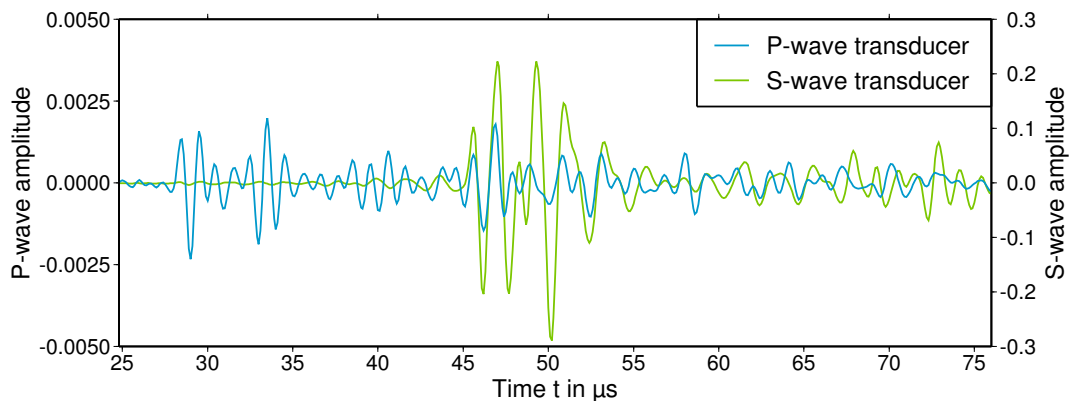


**Figure 6.5:** Example of both P-wave (blue) and S-wave (green) recordings for the axial sample Bo-AS-K3 for a pressure of 30 MPa and a temperature of  $20^\circ\text{C}$ .

Figure 6.5 shows examples of the ultrasonic seismograms of the P- and S-wave recordings at a particular pressure and temperature state. Obvious are the much higher amplitudes of the S-wave signal. It can be seen in this plot, that the S-wave signal also is observable in the P-wave recordings but can hardly be distinguished from P-wave arrivals.

Traveltimes were then picked manually for each seismogram. Normally, the first maxima of the P-wave and S-wave signal was picked. Because the first maximum of the radial sample Bo-AS-K3 was disturbed, the arrival time of the first minimum was extracted.



The picked traveltimes for all samples are summarized in Appendix A. With the known length  $L_S$  of each sample (Table 6.1), the velocity  $v_S$  could then easily be calculated:

$$v_S = \frac{L_S}{t}, \quad (6.1)$$

where  $t$  is the traveltime. However, the measured traveltimes present not only the traveltimes through the sample but also the time needed to pass the transducers. Therefore, a certain time has to be removed from the recorded traveltimes to get the real values, which can then be used to calculate the sample velocities. The estimation of the so-called dead time is explained in Section 6.2.4. The final sample velocities are then calculated in the following way:

$$v_S = \frac{L_S}{t_{rec} - t_{dead}}, \quad (6.2)$$

where  $t_{rec}$  is the recorded traveltime and  $t_{dead}$  is the dead time.

### 6.2.4 Dead time correction

The ultrasonic waves have to travel through the transducers, which have unknown P- and S-wave velocities. For the experiment, it is important to measure the real arrival times of P- and S-wave of the samples. Therefore, the time in which the waves are traveling through the transducers (dead time) must be subtracted from the measured arrival times. To estimate the dead time of the experimental setup, samples with different length but of the same material and, hence, the same velocities are used. The traveltimes of the samples  $t_S$  are recorded for P- and S-wave arrivals for all sample lengths  $L_S$ . The traveltime as a function of sample length is plotted in Figure 6.6. With a linear regression, the dead time can then be calculated. It is the intercept of the obtained linear function (traveltime normal)

$$t_S = a L_S + t_{dead}, \quad (6.3)$$

where  $a$  is the slope of the traveltime normal and  $t_{dead}$  is the dead time. The calculated dead times for the used measuring system are summarized in Table 6.2. For the S-wave signal no first arrival traveltime could be identified because of interferences with the P-wave signal.



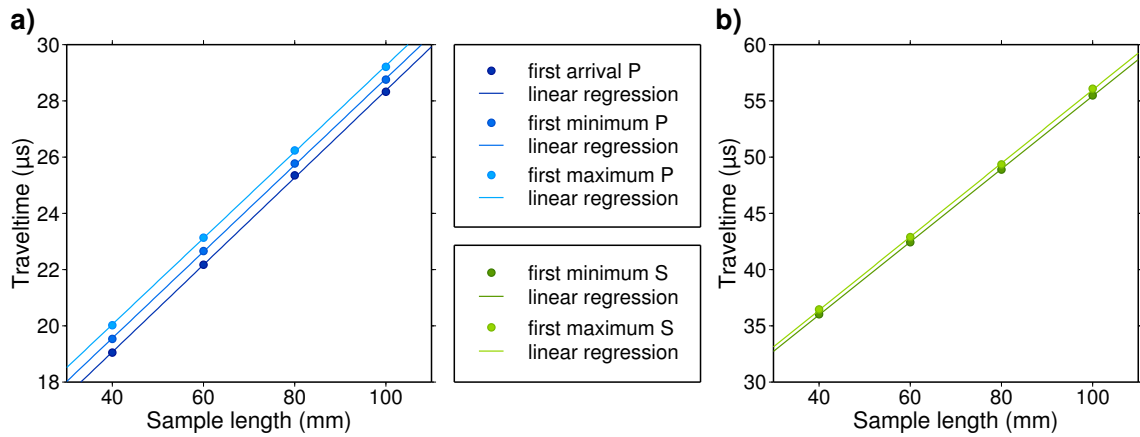


**Figure 6.6:** Estimation of the traveltime normal (dead time) of the ultrasonic transducers using samples of the same material with different length. (a) Traveltimes for four different sample sizes and the P-wave transducer. Recorded are the first arrival traveltime and the traveltimes of the first minimum and the first maximum of the trace. (b) Traveltimes of the first minimum and the first maximum of the S-Wave signal. Due to the overlap with the P-wave signal, the first arrival traveltime of the S-wave cannot be recorded.

	P-wave	S-wave
	$t_{dead}$ in $\mu s$	$t_{dead}$ in $\mu s$
1. arrival	12.868	
1. minimum	13.407	22.997
1. maximum	13.913	23.331

**Table 6.2:** Summary of calculated dead times for all recorded P- and S-wave arrivals. These values must be subtracted from the arrival times after the measurements to obtain the real traveltimes.

### 6.2.5 Error estimation

Laboratory measurements are influenced by several sources of errors. Therefore, the measured traveltimes and lengths of the samples should be evaluated carefully. There are a lot of errors possible and the main sources of errors considered here are listed below:

- measurement of sample length
- traveltime measurement (picking error)
- unstable pressure and temperature conditions

- inaccuracy of pressure and temperature sensors
- inaccuracy of piezoelectric transducers
- insufficient coupling

All measured values are used to calculate the final velocities for the given pressure and temperature conditions. Therefore, the errors of the single measurements may be propagated resulting in a non-negligible discrepancy. The calculation of the single errors is difficult, so the errors of the final velocities were expected to be around 1 % for the P-wave and around 2 % for the S-wave (D. H. Johnston, 1987).

## 6.3 Velocity data

### 6.3.1 Velocity with temperature and pressure

The calculated velocities depending on the different pressure and temperature conditions, as described before, are presented in the following Figures 6.7 - 6.10. Displayed in blue and in the upper part of each figure are the P-wave velocities, in the middle part of each figure are the S-wave velocities in green colors and the lower part of the figures presents the compressional to shear wave velocity ratio  $v_P/v_S$  with yellow colors. Some data points are missing. That is due to unreadable seismogram files or the impossibility to pick the arrival times. Generally, it was very difficult to extract the S-wave arrival times due to the overlap of the signal with the P-wave arrivals.

#### Bo-AS-K3, axial

The velocities of the wave propagation perpendicular to the bedding of sample Bo-AS-K3 are plotted in Figure 6.7. Both velocities as a function of pressure first increase with increasing pressure and then decrease when the pressure is reduced again. The curves show the shape of a hysteresis, that means that the starting value is not reached again but the velocities are higher for decreasing pressure than for increasing pressure. For the pressure dependency, the difference between the highest and lowest velocity values amounts to 0.15 km/s for the P-wave and 0.07 km/s for the S-wave. At low pressures, the velocity changes rapidly, whereas the velocity increase for higher pressures is smaller.

Velocities as a function of temperature show a negative gradient (right panel in Figure 6.7). Highest velocities occur at lowest temperatures. The P-wave velocities are reduced by 0.15 km/s when the temperature is increased from 20 to 80 °C, whereas the S-wave velocities of lowest and highest temperature differ by a value of 0.10 km/s. That means, that the P-waves are more dependent on pressure and temperature changes than the S-wave.

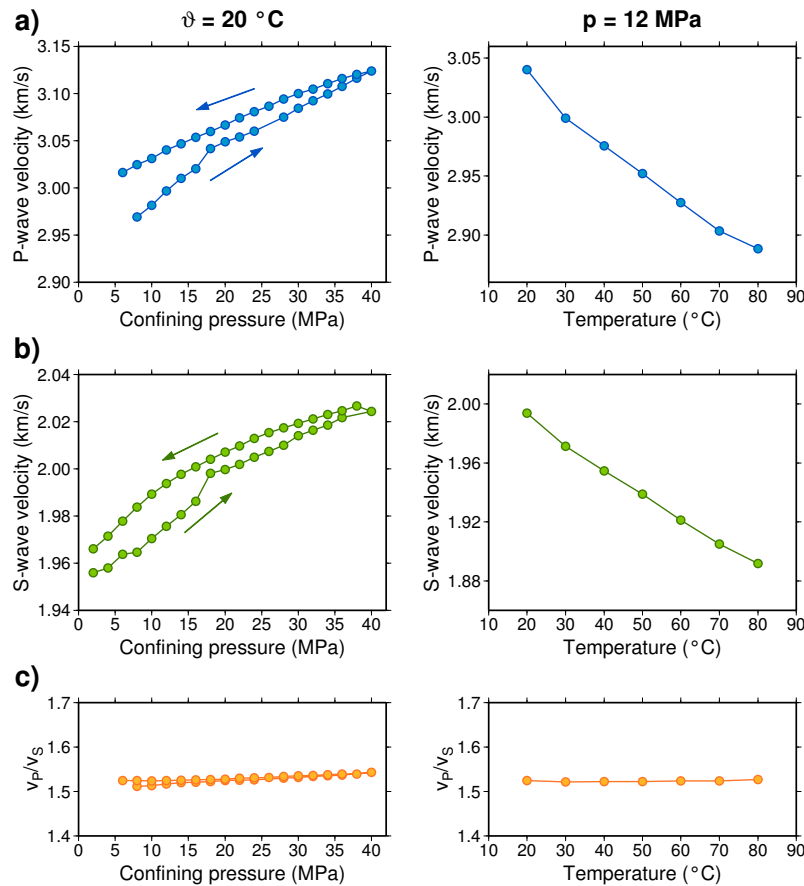


**Figure 6.7:** P-wave velocity (a), S-wave velocity (b) and the velocity ratio (c) of the axial sample Bo-AS-K3 according to pressure changes at room temperature (left panel) and as a function of temperature at a constant pressure of  $p = 12\text{ MPa}$  (right panel).

The P-wave velocities are in a range between 2.89 km/s for the highest temperature and 3.12 km/s for the highest pressure. The S-wave velocity is highest with a value of 2.03 km/s also for high pressures and the lowest value of 1.89 km/s occurs at high temperature. The velocity ratio (Figure 6.7c) is relatively stable for all pressure and temperature conditions and shows a value of about  $v_P/v_S = 1.52$ .

### Bo-AS-K3, radial

For wave propagation parallel to the bedding of the shale sample Bo-AS-K3 (radial sample), the velocities and velocity ratios in dependency to pressure and temperature are displayed in Figure 6.8. Again, the pressure curves show the shape of a hysteresis with higher velocities for decreasing pressure. P- and S-wave velocities with temperature (right panel of Figure 6.8) have an almost linear trend with a negative slope. The P-wave velocity is now much higher than for the axial sample (Figure 6.7a) and it is in a range between 4.33 and 4.48 km/s for the pressure dependency and between 4.25 and 4.41 km/s

for the temperature curve. The S-wave velocity is a little less than for the axial sample and changes between 1.82 and 1.92 km/s for both pressure and temperature curves. Both P- and S-wave show a higher dependency on temperature changes than on pressure variations.

The much higher P-wave velocity also has an influence on the compressional to shear velocity ratio (Figure 6.8c). With a value of about  $v_P/v_S = 2.32$ , it is much higher for the radial sample compared to the axial one. But the tendency of a relatively stable velocity ratio also is valid for the radial sample shown here.

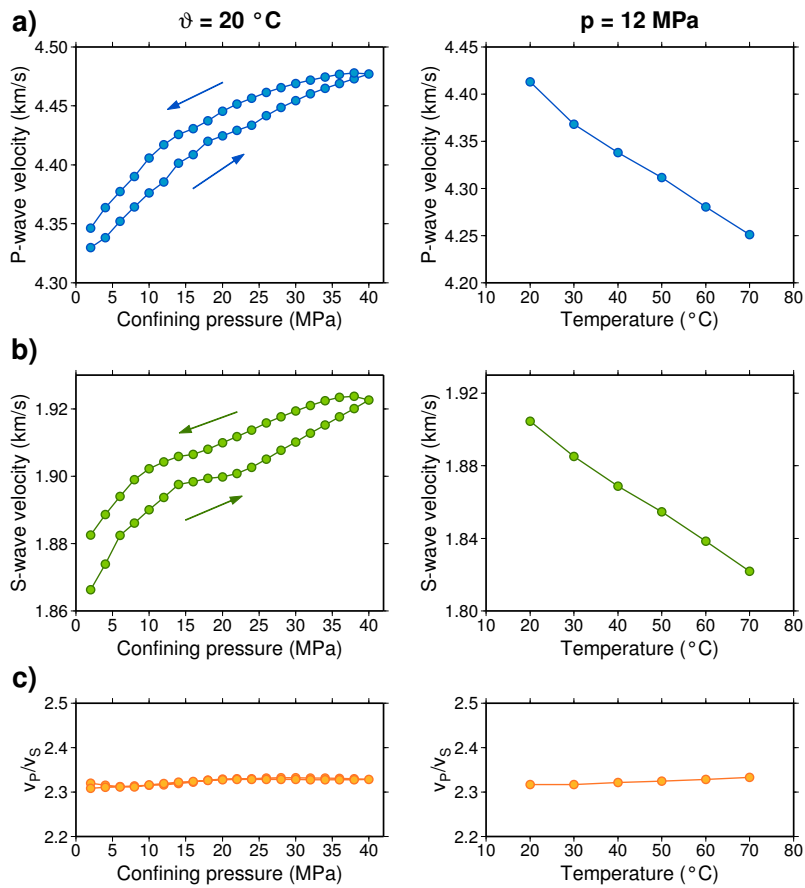


**Figure 6.8:** P-wave velocity (a), S-wave velocity (b) and the velocity ratio (c) of the radial sample Bo-AS-K3 according to pressure changes at room temperature (left panel) and as a function of temperature at a constant pressure of  $p = 12\text{ MPa}$  (right panel).

### Bo-AS-K7, axial

Two pressure cycles for the sample Bo-AS-K7 were conducted, a first at room temperature and a second at the highest temperature of  $\vartheta = 80\text{ }^{\circ}\text{C}$ . Unfortunately, during the first pressure cycle of the axial sample of Bo-AS-K7 no S-wave could be observed. Therefore, the S-wave velocities and velocity ratios are missing for these measurements. Additionally,

it was difficult to extract the P-wave arrival times and impossible to get the S-wave information for the first three pressure stages of the second pressure cycle (Figure 6.9a-b, middle part).

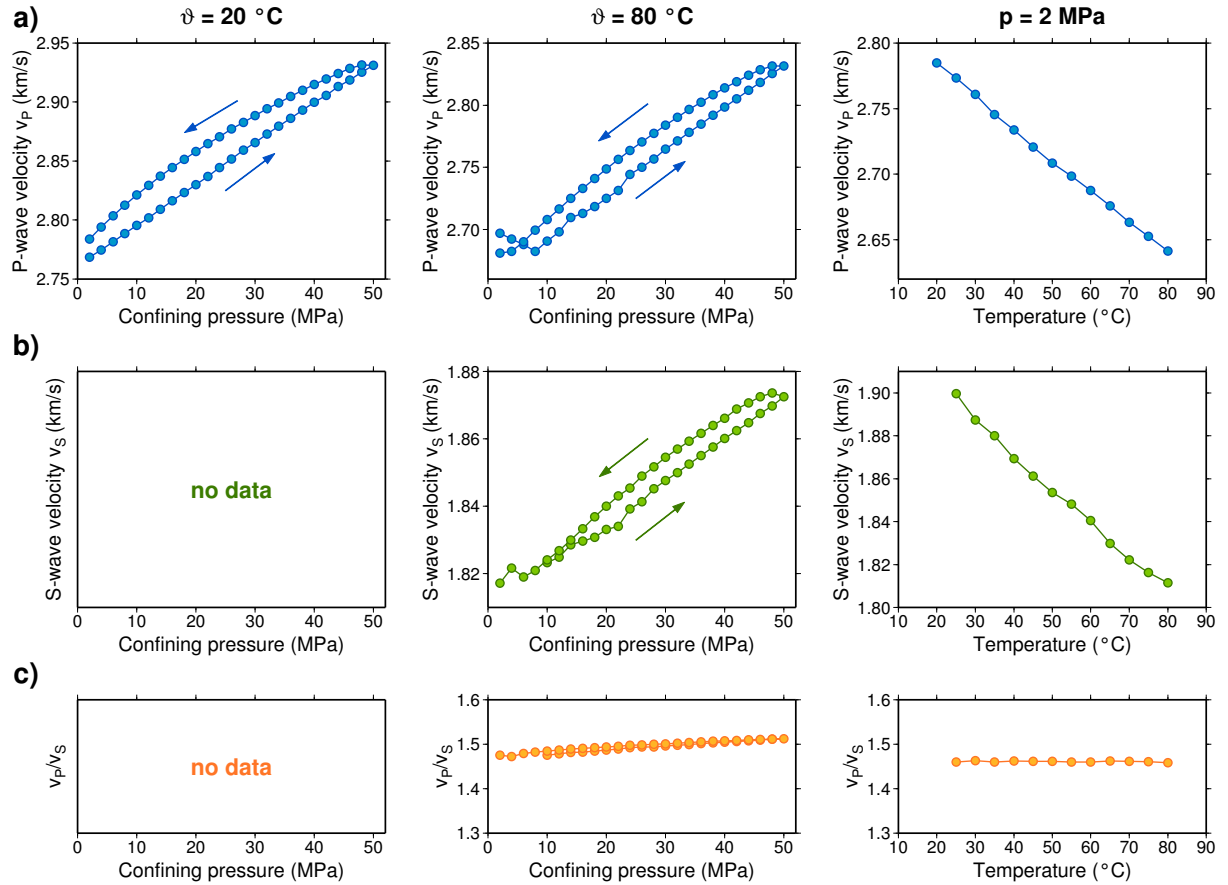


**Figure 6.9:** P-wave velocity (a), S-wave velocity (b) and the velocity ratio (c) of the axial sample Bo-AS-K7 according to pressure changes at room temperature (left column) and at a temperature of 80 °C (middle column) and as a function of temperature at a constant pressure of  $p = 2$  MPa (right column).

In accordance to pressure, the P-wave velocity for both pressure cycles (Figure 6.9a, left and middle column) is in a range between 2.77 and 2.93 km/s and between 2.68 and 2.83 km/s, respectively. The velocity during the pressure cycle at high temperature is little lower and the difference between largest and lowest velocity value is less than for the first pressure cycle at room temperature. The S-wave velocities range between 1.82 and 1.87 km/s for the second pressure cycle and between 1.81 and 1.90 km/s when the temperature is changed.

Again, the temperature depending curves show a negative velocity gradient. In comparison to the pressure dependency, the temperature appears to have more influence on velocity changes for the S-wave than for the P-wave. No difference in the relative velocity ranges of the P-wave can be found between pressure and temperature dependency. In

both cases the P-wave velocity varies by 0.15 km/s.

The P-wave to S-wave velocity ratio is very low and differs for pressure and temperature measurements. For the second pressure cycle, the ratio shows a value of about 1.50 and is slightly increasing with increasing pressure. The velocity ratio for the temperature dependency again is very stable at all temperatures with a value of  $v_P/v_S = 1.46$ .

### Bo-AS-K7, radial

For the Bo-AS-K7 sample with wave propagation parallel to the bedding, all velocity curves for both pressure cycles and decreasing temperature could be determined, although the S-wave arrival again was very difficult to pick. The resulting P- and S-wave velocities are depicted in Figure 6.10.

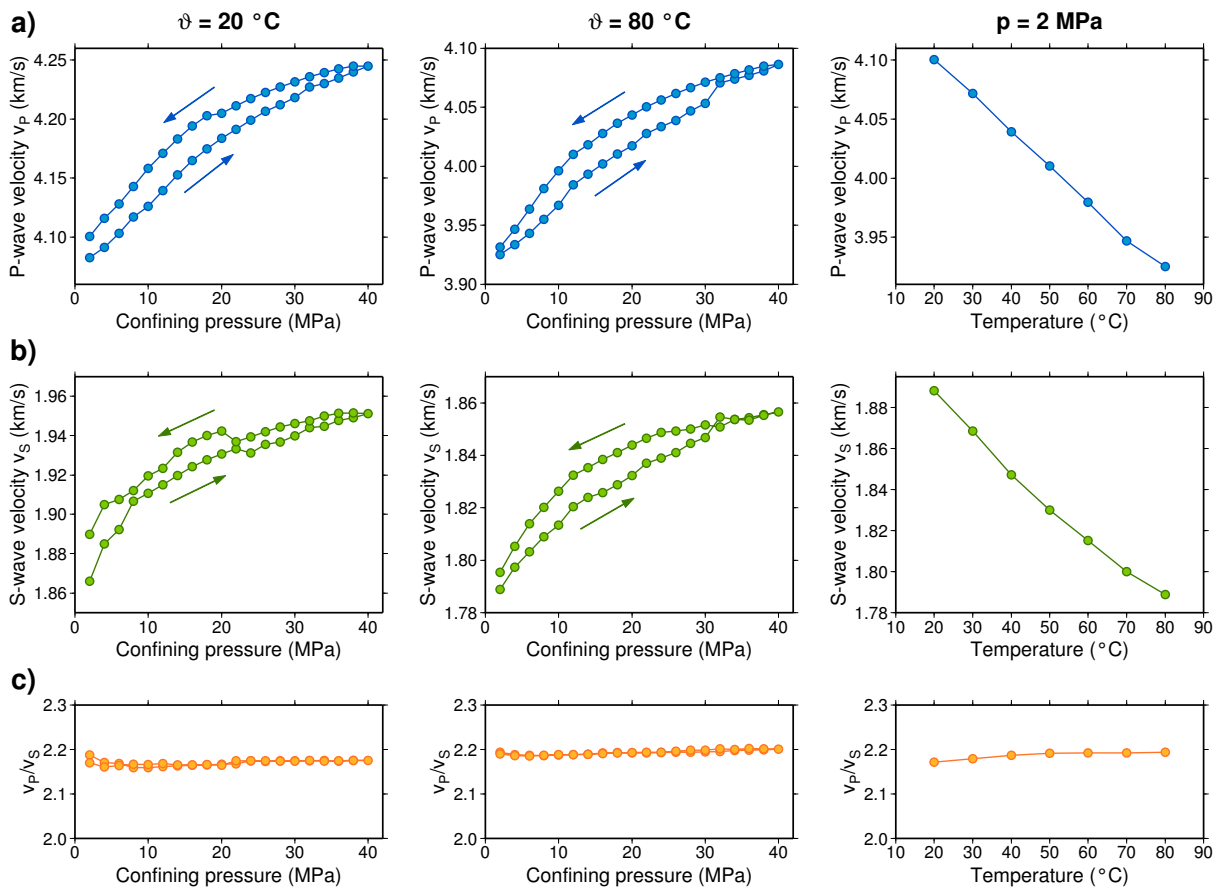


**Figure 6.10:** P-wave velocity (a), S-wave velocity (b) and the velocity ratio (c) of the radial sample Bo-AS-K7 according to pressure changes at room temperature (left column) and at a temperature of  $80\text{ }^{\circ}\text{C}$  (middle column) and as a function of temperature at a constant pressure of  $p = 2\text{ MPa}$  (right column).

The P-wave velocities are again much higher than for the same sample but different alignment (Figure 6.9). They range between 4.08 and 4.25 km/s during the pressure changes at room temperature, between 3.93 and 4.09 km/s for the second pressure cycle

and between 3.93 and 4.10 km/s when the temperature is changed. Once again, the pressure curves show the shape of a hysteresis. The small jump of P-wave velocity during the second pressure cycle at increasing pressure from 30 to 32 MPa was caused by pausing the measurements (center of Figure 6.10a). The sample has been left in the measuring unit under pressure during a whole weekend. Probably, not till than stable conditions have been reached.

This jump of the velocity is also visible in the values of the S-wave (Figure 6.10b). The velocity values of the S-wave in the first pressure cycle are considerably disturbed, again indicating that the picking of the S-wave arrivals was particularly complicated. For higher temperatures the S-wave signal in the seismograms becomes much clearer leading to a smoother curve in the second pressure cycle. The velocity range of the S-wave is between 1.79 and 1.95 km/s, in which the variance of velocity is largest for the temperature dependency.

Like the radial sample of Bo-AS-K3 (Figure 6.8), the velocity ratios are on a high level with values of approximately 2.2 (Figure 6.10c). Little deviations from a constant trend can be seen for low pressures and at low temperatures. That is again caused by the difficult extraction of S-wave arrivals from the ultrasonic seismograms. The small jump of velocities in the second pressure cycle described before has no influence on the velocity ratio.

In summary, all pressure dependent measurements show a hysteresis, where the velocities for increasing pressure are always lower than the velocities for the afterward decreasing pressure. Jones and Wang (1981) found the same behavior for samples of Cretaceous shales. The temperature curves are almost linear with a negative velocity gradient. The P-wave velocities for the axial samples are higher compared to the radial ones showing a high amount of anisotropy, whereas the S-wave velocities measured here are almost independent of the direction of wave propagation. Normally, the S-wave shows shear-wave splitting for wave propagation parallel to the bedding. With the used ultrasonic measuring system, it was not possible to record and distinguish the splitted S-waves. Therefore, the results for the velocity ratio and the S-wave velocity anisotropy should be considered with care.

All samples show a higher dependency of the S-wave velocity according to temperature than according to pressure. No different behavior of the P-wave velocity can be observed when the pressure and temperature dependencies are compared. The P-wave velocity curves are more evenly shaped than the S-wave curves because the arrival times of the S-wave were more difficult to identify so that the picking error is much greater for the S-wave. Changes in P-wave velocity are much higher than changes in S-wave velocity for all pressure and temperature dependencies.

In the measurements, the compressional to shear wave velocity ratio emerged as independent on both pressure and temperature changes. The velocity ratio is dependent on mineralogical changes in the sample, but during the ultrasonic measurements only the structure of the samples is changed with pressure and temperature. Therefore, a constant value was expected. Due to the anisotropic P-wave, the velocity ratio also shows a great amount of anisotropy. The velocity anisotropy will be analyzed in more detail in the next section.

### 6.3.2 Velocity anisotropy

Black shales are known to be strongly anisotropic. There are various causes for the occurrence of anisotropy. The most common assumption for the cause of anisotropy of shales is the preferred alignment of clay minerals and organic material (e.g., Vernik & Liu, 1997). The black shales of the Alum Shale Formation are horizontally layered. Therefore, they can be assumed being transverse isotropic (TI) media with a vertical symmetry axis (J. E. Johnston & Christensen, 1995). TI media are seismically characterized by a faster wave propagation in the horizontal direction and slower wave propagation in the vertical direction. That behavior can also be seen in the results of the seismic measurements of both black shale samples. Wang (2002) found the anisotropy of the P-wave velocity of shales to be up to 30 %, depending on porosity, compaction history and the type of clays. To estimate the anisotropy that is obviously visible in the velocity values of the different orientated samples (Figures 6.7 - 6.10), the relative anisotropy for each pressure and temperature state was calculated with equation 6.4:

$$A(\%) = \left| 1 - \frac{v_{axial}}{v_{radial}} \right| \cdot 100 \%, \quad (6.4)$$

where  $v_{axial}$  are either the P-wave or the S-wave velocities of the sample with wave propagation perpendicular to the bedding and  $v_{radial}$  are the P-wave or S-wave velocities of the sample with wave propagation parallel to the bedding.

The estimated anisotropy values are summarized in Appendix B and are plotted in Figures 6.11 and 6.12 for the P-wave velocity and the velocity ratio, respectively. The anisotropy with pressure and temperature shows an opposite behavior to the velocities: With increasing pressure, the anisotropy is decreasing and the temperature dependent anisotropy is increasing with increasing temperature.

The anisotropy of the P-wave velocity is decreasing by 1 % during the pressure increase of 40 MPa (Figure 6.11a). Around pressures of 15 - 20 MPa, the anisotropy of the sample Bo-AS-K7 shows slightly heightened values. That deeper sample also shows an overall trend of 1 % higher anisotropy compared to the sample Bo-AS-K3. Therefore, a small increase of P-wave velocity anisotropy with depth was observed. The gap in the anisotropy



values at highest pressures for Bo-AS-K7 is caused by the slightly different pressure cycles for the axial and radial sample. For the axial sample the pressure was increased to 50 MPa, whereas the pressure was already decreased after reaching 40 MPa for the radial sample. During the heating of the sample from room temperature to 80 °C (Figure 6.11b), the anisotropy increases by 0.5 %. That means, contrary to the behavior of the velocities (Section 6.3.1), the anisotropy shows a higher dependency according to pressure changes.

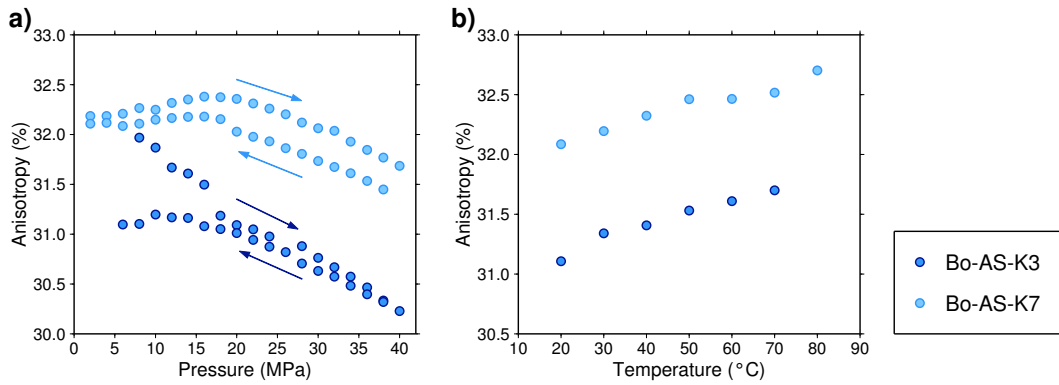


**Figure 6.11:** P-wave velocity anisotropy as a function of pressure (a) and temperature (b). The results of the shallower sample Bo-AS-K3 are plotted in dark blue, whereas the values of the deeper sample Bo-AS-K7 are depicted with light blue dots. The shallower sample shows lower anisotropy than the deeper sample. Both dependencies have a reverse behavior to the pressure and temperature dependent curves of the P-wave velocity (Figures 6.7 - 6.10).

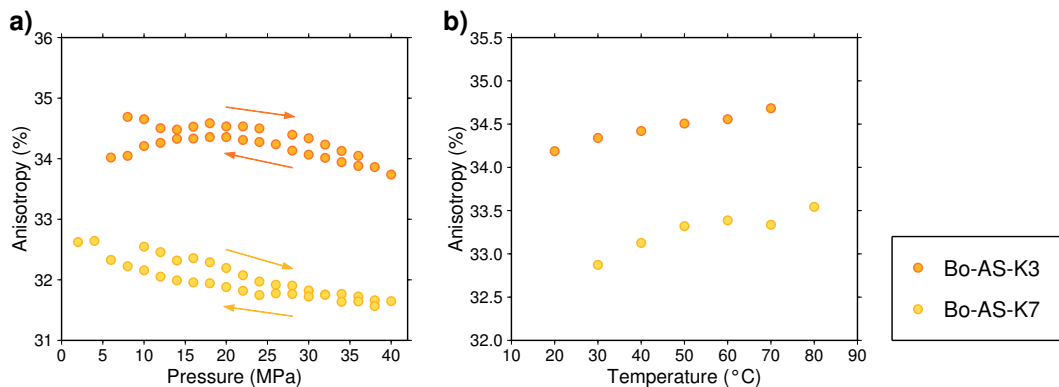


**Figure 6.12:** The anisotropy of the velocity ratio with pressure (a) and temperature variation (b). The shallower sample (Bo-AS-K3, orange dots) has higher anisotropy values than the deeper sample (Bo-AS-K7, yellow dots). The velocity ratio also shows decreasing anisotropy with pressure and increasing anisotropy with temperature.

The shapes of the pressure and temperature dependent curves of the velocity ratio anisotropy (Figure 6.12) equal the corresponding curves for the P-wave anisotropy. The

differences between the maximum and minimum values are again 1% for the pressure curve and 0.5% for the temperature curve. But now, the anisotropy shows 1.5 - 2% higher values for the shallower sample Bo-AS-K3. That is due to the much lower anisotropy of the S-wave velocity for that sample. The S-wave anisotropy as a function of pressure and temperature is not plotted here because the found S-wave recorded with the measurement system described here shows almost no anisotropy at all.

Due to interferences with other wave types, the picking of the S-wave arrival times was especially difficult. Therefore, the S-wave values must be considered with care. The errors of the S-wave estimation are then transferred to the values of the velocity ratio, which, therefore, also have to be analyzed critically.

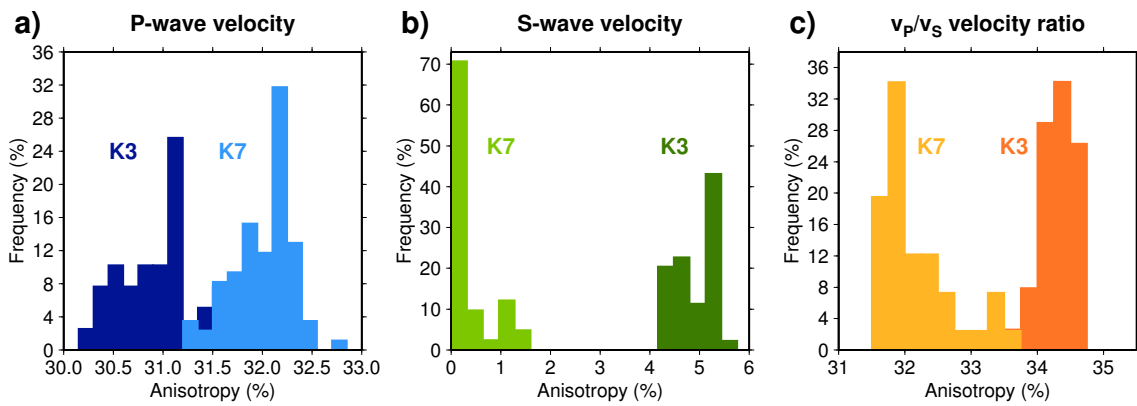


**Figure 6.13:** Histograms of laboratory P-wave velocity (a), S-wave velocity (b) and velocity ratio anisotropy (c), respectively. Results of the deeper sample (Bo-AS-K7) are highlighted by lighter colors. The S-wave shows only little anisotropy, but the P-wave has significant anisotropy values of more than 30% leading to also high velocity ratio anisotropy.

Sample	$A_P$ (%)	$A_S$ (%)	$A_{P/S}$ (%)
Bo-AS-K3	31.0294	4.8997	34.2949
Bo-AS-K7	32.0077	0.3843	32.1767

**Table 6.3:** Average anisotropy values of P-wave velocity, S-wave velocity and the velocity ratio for both samples.

Histograms of all calculated anisotropy values are depicted in Figure 6.13. Here, it is not distinguished between pressure or temperature measurements, but the two different samples are marked by different colors. Darker colors highlight the values for the shallower sample Bo-AS-K3 and lighter colors represent the deeper sample Bo-AS-K7. For the sample Bo-AS-K7 two pressure cycles for different temperatures have been conducted. Therefore, more velocity and anisotropy data are available. The anisotropy of the P-wave

velocity ranges between 30 and 31.5 % for Bo-AS-K3 and between 31.5 and 33 % for Bo-AS-K7 (Figure 6.13a). The same variance is found in the anisotropy distribution of both samples. The maximum of Bo-AS-K3 is around 31.2 % and the maximum of Bo-AS-K7 is at 32.2 %. That means, the deeper sample Bo-AS-K7 of the Furungian part of the Alum Shale has 1 % higher anisotropy values for the P-wave. The S-wave velocity of that sample shows hardly any anisotropy (Figure 6.13b). The anisotropy values of up to 1.5 % are in the range of the measurement error for the S-wave. Therefore, anisotropy can be neglected for the S-wave velocity of the sample Bo-AS-K7. However, the shallow sample Bo-AS-K3 of the Lower Ordovician part of the Alum Shale shows 4 - 6 % S-wave anisotropy. That value is not negligible and clearly demonstrates, that the different samples, thus the different parts of the Alum Shale show a different anisotropy behavior. Due to the fact that only S -wave velocity anisotropy for the shallow Bo-AS-K3 sample was recorded, the velocity ratio shows, contrary to the P-wave velocity anisotropy, higher anisotropy for that shallow sample (Figure 6.13c). The anisotropy of Bo-AS-K3 is now between 33.5 and 34.8 % and the anisotropy of Bo-AS-K7 ranges between 31.5 and 33.8 %. The maximum values are around 34.5 and 32 % for Bo-AS-K3 and Bo-AS-K7, respectively. The average anisotropy values are summarized in Table 6.3.

## 6.4 Discussion and conclusions

Ultrasonic measurements were carried out to determine the seismic velocities and the velocity anisotropy of black shale samples under different temperature and pressure conditions. Samples of two different depths representing two different units of the Alum Shale Formation (see Section 2.4) were used. For each of the depths range two perpendicular samples were extracted – one with wave propagation parallel to the bedding and the other with wave propagation perpendicular to the bedding – to calculate the anisotropy values. The P-wave and S-wave velocities of the different samples along with the corresponding velocity ratios were determined for pressure cycles at room temperature and for one sample depth additionally at 80 °C. Therefore, the pressure was systematically increased and then decreased again. The temperature dependency of the velocities was measured for increasing temperatures from 20 to 80 °C.

All pressure dependent curves of P-wave and S-wave velocity show the shape of a hysteresis, which was expected from the literature. That means, the values for decreasing pressures are higher than for the pressure increase leaving a small gap between the starting point and the endpoint. The velocity curves for the temperature increase are linear with a negative velocity gradient. In additional measurements with a temperature decrease directly after the increase (not shown here), equal velocity values occur for both temperature changes with no gap between starting point and endpoint. Consequently,

the seismic velocities show a different behavior according to pressure changes than to temperature changes.

Comparing both body wave types, the P-wave velocity is depending more on pressure and temperature changes than the S-wave, which can be seen in the larger value range of the P-wave velocity. The P-wave is equally influenced by pressure and temperature, whereas the S-wave velocity shows a higher dependency with a larger value range when the temperature is changed. Surprisingly, both velocities are lower for the deeper sample, but the difference for the S-wave velocity between both sample depths is not as large as for the P-wave velocity. It was expected, that the velocity is increasing with depth, but the found trend is also visible in the sonic log velocities (Sections 2.4 and 3.3.2) for the depths of 10.5 m ( $v_P(\text{sonic}) = 3.09 \text{ km/s}$ ) and 23.5 m ( $v_P(\text{sonic}) = 2.90 \text{ km/s}$ ). The velocity is not only varying due to the increased compaction with increasing depth. Additionally, the different stratigraphical parts of the black shale (Section 2.4, Table 6.1) have slightly different mineralogical compositions which leads to the unexpected behavior of decreasing values with depth.

The P-wave velocity for the sample with wave propagation parallel to the bedding is much larger than for wave propagation perpendicular to the bedding. In contrast, the S-wave velocity is quite independent of the sample direction. That fact has a large effect on the ratio of compressional and shear wave velocity. The perpendicular samples have a much lower  $v_P/v_S$  ratio than the parallel samples. Compared to a reference value of 1.7, the perpendicular samples are slightly below and the parallel samples are significantly above this ratio. Independent of the value that is changed, the velocity ratio is very stable showing almost constant values for all pressure cycles and temperature curves. That means, the  $v_P/v_S$  ratio is also independent of the depositional depth (different pressure/temperature) of the black shale layer. The velocity ratio is only dependent on the mineralogical composition and, therefore, an optimal seismic value for the characterization of black shales.

A significantly different anisotropy behavior for P-wave and S-wave velocity was observed. The P-wave velocity shows an average anisotropy of little more than 30 %, which is a value also found in the literature. In contrary, the S-wave velocity in the measurements presented here has almost no anisotropy. The P-wave has higher anisotropy in the deeper sample Bo-AS-K7 and the S-wave anisotropy of this sample can be neglected because it is in the range of the measurement error. Therefore, the velocity ratio shows a reverse behavior to the P-wave with higher anisotropy for the shallow sample Bo-AS-K3.

Unfortunately, only perpendicular samples of two different depths and, hence, two different units of the Alum Shale could be extracted. Therefore, it is questionable, if the achieved depth dependencies are representative for the whole Alum Shale Formation. But

---

a first trend of increasing P-wave velocity anisotropy with depth is observable. Additionally, also other parameters like geochemical components (e. g., TOC) or the maturity are related to the P-wave anisotropy. Maturity values were not available for different depths, but the TOC content (Figure 3.21) shows higher values around the deeper sample, which is in correlation with the P-wave anisotropy found here.



---

## 7 Joint interpretation

The previous chapters, each describing one method to interpret the seismic data achieved on Bornholm, were all self-contained but were discussed individually. In this chapter, the different results will now be combined and analyzed with regard to the given objective of this work to, amongst others, seismically characterize the black shale formation according to its potential as a source rock.

The results of the two active field experiments are combined by calculating the velocity ratio for the profile Line-3. Only for this seismic profile, different methods were carried out. Therefore, the joint interpretation is concentrated on this profile. The velocity ratio is an indicator for the gas content in the shale and is properly analyzed, also with regard to the different length scales of the measurements. Different methods may reveal different information from the subsurface. Hence, the combination of the methods will improve the overall understanding of the subsurface at the study location.

### Velocity ratio of the black shale layer

In Chapter 3, the P-wave velocity model of the seismic profile Line-3 was obtained with travelttime tomography. The final result clearly shows the Alum Shale layer between the Komstad Limestone layer with higher velocities on top and the Læså Sandstone Formation beneath the black shale (Figure 7.1a,b). A S-wave velocity model along the same profile was then determined with surface wave inversion (Chapter 4). The smoothed S-wave model (Figure 7.1c) only covers the inner part of the P-wave model. Therefore, Figure 7.1b shows a cutout of the P-wave tomography result of Line-3.

Both P-wave and S-wave velocity models were then used to calculate the compressional to shear velocity ratio  $v_P/v_S$  of that part of the profile Line-3 (Figure 7.1d). For the Læså Sandstone Formation values around  $v_P/v_S = 1.7$  are found (green colors). That represents the reference value for consolidated rocks. In contrary, the black shale layer is clearly separated from the adjacent layers by very low  $v_P/v_S$  ratios around 1.4 (blue colors). When the distribution of the velocity ratio is compared to the contour lines which were determined in Section 3.3.1 to separate the individual layers, it can be seen that there is a good match for the Alum Shale Formation. Because the limestone layer was not seen by the surface wave inversion, it is not present in the S-wave model and it is also absent in the  $v_P/v_S$  distribution.

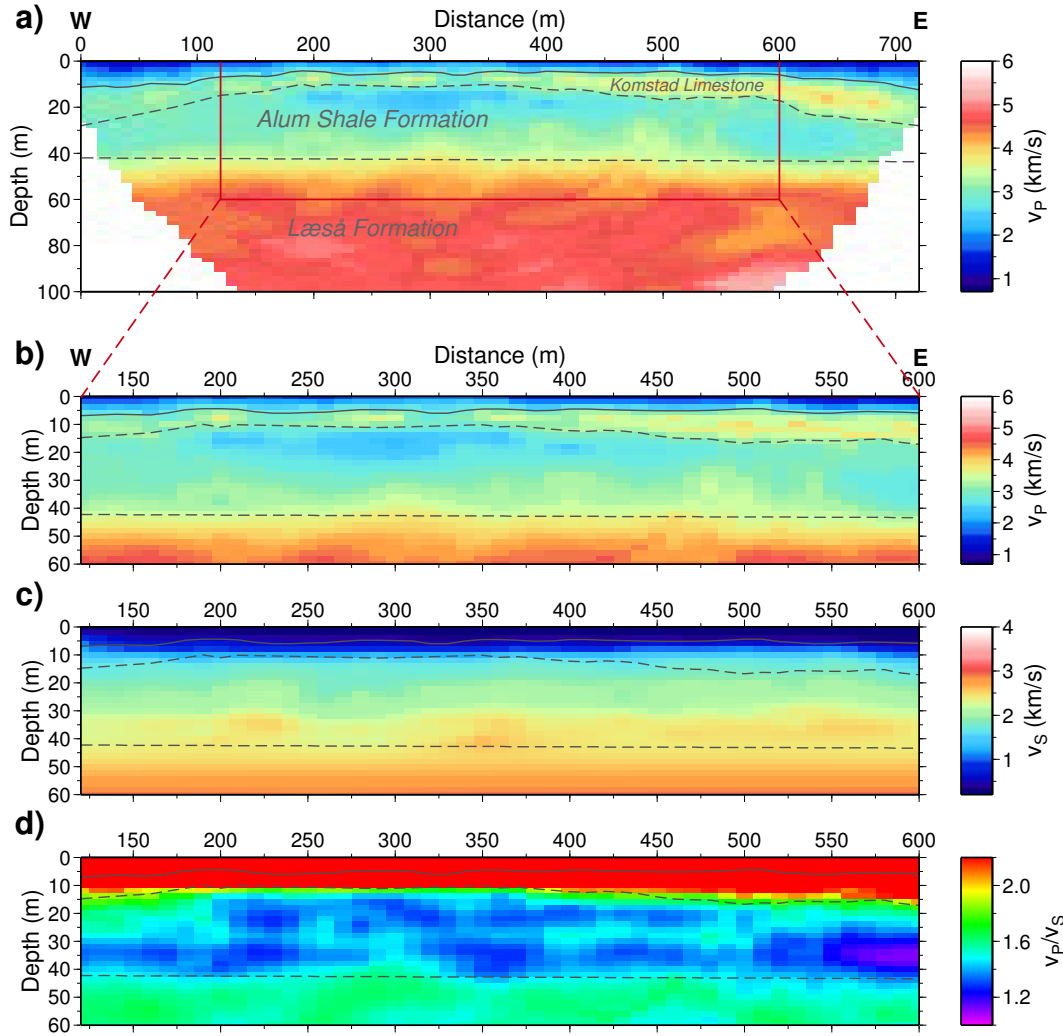


**Figure 7.1:** The P-wave velocity model determined with travelt ime tomography (a, b), the S-wave velocity model obtained with surface wave inversion (c) and the estimated  $v_P/v_S$  ratio of Line-3 (d).

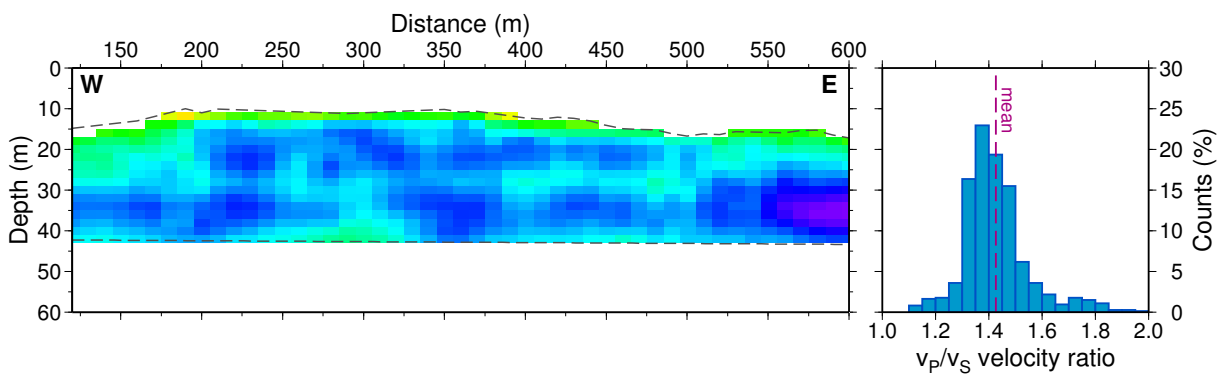


**Figure 7.2:** Distribution of the  $v_P/v_S$  ratio of the separated Alum Shale layer. The histogram plotted in the right part shows the distribution of the calculated  $v_P/v_S$  ratios. Inserted with a dashed magenta line is the average ratio of  $v_P/v_S = 1.426$ .



The velocity ratio of the black shale layer is investigated further by extracting only the values between the contour lines representing the found edges of the black shale (Figure 7.2). The left part of the figure shows a disturbed distribution with a high variance of the velocity ratio which can also be seen in the histogram plot in the right part of Figure 7.2. The average ratio is at  $v_P/v_S = 1.426$ , but the ratios vary from 1.1 to almost 2.0. The highest values are found in the upper part of the Alum Shale. As discussed in Section 3.2.3, the high velocity limestone layer results in higher P-wave velocities in the upper part of the underlying black shale layer. Hence, higher velocity ratios are observed there. A large minimum is present in the lower east part of the Alum Shale. The values there are around  $v_P/v_S = 1.1$ . These extremely low values suggest to be an artifact. In that part, also the P-wave velocity is a little less compared to areas further to the west. That anomaly might be caused by boundary effects and by the overlain limestone layer. The limestone layer is thickened at the outer edges of the model also influencing the layers below. Therefore, the thickness of the Alum Shale is reduced in that part of the model and the velocity must then be lower to achieve the correct traveltimes. Hence, the low P-wave velocity is the cause for the very low  $v_P/v_S$  in that part.

The P-wave and S-wave velocity models were derived with different data sets (of different sources) using different methods. The traveltimes of the P-wave tomography and the dispersive surface waves used for the surface wave inversion are, therefore, influenced by the subsurface velocity structure in a different way which led to the artifacts in the  $v_P/v_S$  distribution described above. Additionally, the S-wave velocity model was smoothed before the calculation of the  $v_P/v_S$  model which might also be the cause for the anomalously high or low ratios at the outer edges of the model. The smoothing results in a little loss of S-wave information but makes the before discrete surface wave model comparable to the P-wave tomogram. However, even if the S-wave model is smoothed, the blocky structure of the original S-wave models is still visible, for example, in the rapidly increasing S-wave velocity around 30 m depth. The vertical velocity changes are, therefore, little different for P-wave and S-wave and, hence, the final  $v_P/v_S$  model shows a slightly disturbed distribution.

However, the combined investigation of P-wave and S-wave velocity from the field experiments shows that the black shale layer is clearly identified by a reduced  $v_P/v_S$  ratio. The velocity ratio is dependent on the in-situ rock parameters like TOC content, mineral composition or porosity (Zhu et al., 2011). But normally, a reduced velocity ratio indicates the presence of gas in the shale. If gas is contained in the black shale, the P-wave velocity is reduced but the S-wave velocity remains constant leading to lower  $v_P/v_S$  (Kumar & Hovørsten, 2012). The Alum Shale layer at the study location can, therefore, be considered as a layer with high reservoir quality and a large shale gas potential.

## Comparison of field scale and laboratory scale

The seismic velocities at the study location were determined and analyzed at different scales: On the field scale of several hundreds of meters the P-wave and S-wave models were obtained by traveltime tomography and surface wave inversion. The sonic log of the borehole Skelbro-2 covers a smaller scale of several meters and the velocities of the black shale samples were determined on the laboratory scale of only a few centimeters. No significant differences can be found for the velocities at the different scales. That shows, that the individual results are very consistent when the length scale is changed. Therefore, it might be possible to characterize a black shale layer on a regional scale by using only small scale and selective measurements from the laboratory and vice versa. For the Alum Shale Formation, the results can be easily conveyed from one scale to another without the need of a calibration. That is a very important fact for future investigations of black shales and is also a proof of the reliability of the individually derived results.

The velocities that are characteristic for the black shale layer in the field experiments are around  $v_P = 3 \text{ km/s}$  and  $v_S = 2 \text{ km/s}$ . The average velocity ratio presented in the previous section is, hence, very low with a value of 1.426. In the laboratory results, the velocities and the velocity ratio depend on the direction of wave propagation through the black shale sample. Interestingly, the field scale values are all comparable to the sample velocities with wave propagation perpendicular to the bedding (axial samples). The average velocity ratios of both axial samples are 1.52 and 1.46 for Bo-AS-K3 and Bo-AS-K7, respectively. That is a little more than the average value on the field scale but is still considerably below a reference value of 1.7.

The laboratory analysis shows, that P-wave velocity and velocity ratio strongly depend on the wave propagation direction. The samples with wave propagation parallel to the bedding of the black shale (radial samples) have much higher P-wave velocity and velocity ratio values compared to the axial samples. With a velocity ratio of more than 2.0 the presence of gas in the shale would not be considered for the radial samples. Therefore, it is really important to know the direction of wave propagation which is mostly influencing the final results of the measurements. Otherwise, an exact classification of the reservoir potential of a studied formation would be difficult.

## Complementary character of the field experiments

The different measurements and methods were used because each is sensitive to a different frequency range and, hence, a different depth range. The complementary character of the different methods can easily be seen in the frequency spectra of the methods (Figure 7.3). With the sweep from 20 to 160 Hz, the vibroseis experiment covers the largest frequency

range (gray line). But due to the rather low energy that is penetrated by the minivibrator, the largest observable offset and the penetration depth are limited to 150 m and 40 m, respectively. In contrary, the weight drop experiment is sensitive to a medium frequency range between 40 and 80 Hz (blue line in Figure 7.3). The penetration depth is much larger reaching more than 100 m and the largest observed offset for the weight drop is around 700 m. The ambient noise measurements are a good addition to both active experiments because much lower frequencies are recorded (green line in Figure 7.3). The lower frequencies in the data will extend the afterward obtained velocity models to larger depths because deeper parts of the subsurface are penetrated by the ambient noise field. The P-waves found in the final interferograms of the ambient noise measurements show apparent velocities around 3.5 km/s. The first arrivals of the weight drop data, in contrast, have apparent velocities of  $v_P = 4.3$  km/s. The apparent velocity of the active experiment is mostly influenced by the high velocity limestone layer between 4 and 8 m depths and the passive experiment mostly sees the black shale or sandstone layers with lower velocities. That confirms the assumption that the ambient noise is more sensitive to larger depths than the weight drop data.

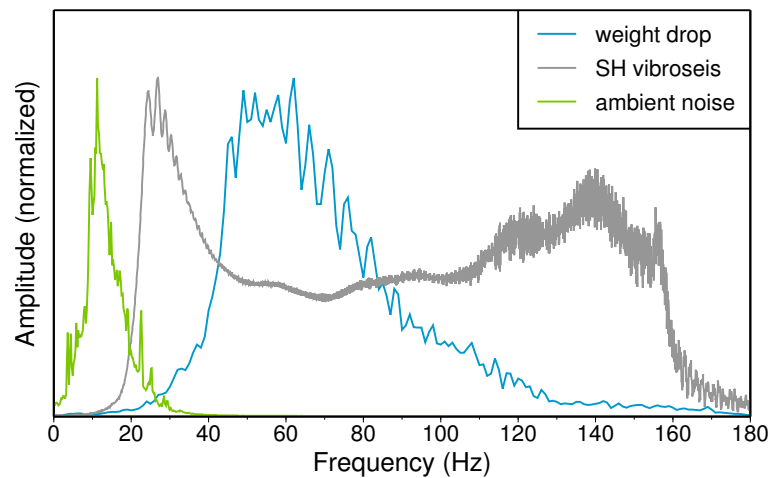


**Figure 7.3:** Comparison of the frequency spectra of the different data sets. The amplitudes of the individual spectra are normalized for a better comparability.

The seismic interferometry can be used to extract information about greater depths of the subsurface velocity distribution. But much more effort is needed to prepare the data so that the interferograms can be analyzed with tomographic methods. It would be possible to apply filters to the interferograms to obtain accurate dispersion curves for a surface wave inversion analog to the vibroseis data. That could not have been done during the work of the thesis but would be a subject for future studies.

Each applied method has its advantages and disadvantages. The travelttime tomography, for instance, can be easily carried out after simply picking the first arrivals of all shot

points. In contrast, the surface wave inversion is much more time-consuming because the process of calculating the phase velocity spectrum, picking the dispersion curve and inverting for the S-wave model has to be done separately for each source point. The seismic interferometry is rather simple because only crosscorrelations of the noise records of two stations have to be calculated; but it is a computationally expensive technique which requires much memory space. The laboratory analysis is also very time-consuming because before the single measurements can be carried out the equilibrium of pressure and temperature needs to be reached, which takes a lot of time. Although it is really laborious, applying all these methods to the data is a good opportunity to combine the best properties of each approach to finally get a very well resolved image of the subsurface.

---

## 8 Conclusions

Active and passive seismic experiments were carried out on Bornholm and sample measurements were conducted in the laboratory to analyze the seismic properties of black shales. The black shale layer at the study location should be located and characterized according to its reservoir properties.

The high-quality travelttime data of the weight drop experiments were used to calculate a P-wave tomography model of each of the three crossing profiles. All models are in a very good match and the regional extension of the black shale formation clearly shows a southward dipping of the found layers. The black shale layer is clearly identified by the P-wave response, especially the bottom depth is imaged very well. The reliability of the models is proven by the comparison with the sonic log data which shows a good agreement between the different scales. Even a correlation with the TOC content can be estimated for which the black shale layer is characterized by a high amount of organic matter.

The S-wave model of Line-3 was obtained with surface wave inversion of Love waves. For each source point 1D S-wave models were determined. All individual models are very consistent throughout the profile and image the black shale layer quite well. Although the high velocity limestone layer cannot be imaged, the reliability of the velocity models is proven by the very consistent bottom depths of the black shale and by comparable S-wave velocities observed in the laboratory.

Ambient noise data was used for a seismic interferometry. For the final interferograms only the crosscorrelations were stacked which show an appropriate signal-to-noise ratio in a selected time window. With this new approach a really short time interval and a very small regional scale was considered. However, reliable results were produced where even P-waves are visible. The very special way of seismic interferometry described here will be the basis for a future research.

The seismic body wave velocities were measured in the laboratory for different pressure and temperature conditions and for perpendicular samples of two different stratigraphical parts of the Alum Shale. The velocities for the samples with wave propagation perpendicular to the bedding are comparable to the results of the field experiments. The P-wave velocity shows a high amount of anisotropy because the velocities for wave propagation parallel to the bedding are about 30 % higher. In contrary, the S-wave velocity is quite independent of the wave direction. The laboratory studies also reveal the independence

of the  $v_P/v_S$  ratio on pressure and temperature changes. Therefore, this seismic value is particularly suitable to characterize the black shale at different depths.

All in all, the black shale is imaged very well with the different methods and the three-dimensional extension is localized at the study location with a southward dipping of the layers. The results are very consistent throughout the different scales and the different methods. The black shale layer shows a reduced P-wave velocity compared to the adjacent layers. It also has a reduced  $v_P/v_S$  ratio which clearly separates this layer from the surrounding formations. A low velocity ratio is an indication for gas contained in the black shale formation. Therefore, with a high TOC value and a low  $v_P/v_S$  ratio, the Alum Shale layer on Bornholm is assumed to be a hydrocarbon source rock with a considerable gas content.

The different stratigraphical formations identified at the study location are characterized mostly as a whole. But the laboratory measurements of the samples of different depths and also the P-wave tomography revealed a partitioning of the Alum Shale into different units with slightly varying seismic properties. Future seismic investigations of the Alum Shale at shallow depth, therefore, should be designed to even detect these small scale changes, for example, by using higher frequencies and smaller source and receiver distances. The P-wave vibroseis was not considered in this work. The Rayleigh waves of the P-wave vibroseis data can be used for a joint inversion of surface waves together with the Love waves of the SH vibroseis data. That method probably gives better resolved velocity models were also the limestone layer can be imaged. The seismic interferometry was done to extend the frequency range to lower values and, hence, to reveal information of greater depths. It was not possible to extract dispersion curves from the interferograms during the work on the thesis, but maybe a different approach can be found in future researches to use the additional information of the ambient seismic noise.

# Acknowledgments

The topic of the thesis was provided by Prof. Michael H. Weber, head of Department 2 and Section 2.2 at GFZ Potsdam. He is thanked for his helpful comments and his support with problems not only concerning the scientific work but also administrative issues.

I am also grateful to Klaus Bauer, who introduced to me the method of seismic tomography and who supported me with his comprehensive knowledge in various parts of the thesis.

Manfred Stiller is thanked for his help with ProMAX and the seismic data processing. He also accurately proofread large parts of the thesis and gave copious helpful hints.

Klaus and Manfred were instrumental in preparing and conducting the seismic measurements. Along with the other team members of both Bornholm experiments, Mike Hönig, Karl Otto, Kevin Bogott, Thomas Haberlau and Manuel Amberger, they are thanked for their effort to bring in excellent seismic data and for the cheerful evenings on this wonderful island.

The field work would not have been possible without Niels H. Schovsbo from the Geological Survey of Denmark and Greenland, who contacted the farmers on Bornholm and helped with the permissions. Besides, he gave constructive comments to the geological part of the thesis.

Erik Spangenberg helped with the preparation of the black shale samples, the setup and function of the laboratory experiment and proofread the corresponding part of the thesis. For the interferometry part, Trond Ryberg provided the computationally expensive cross-correlations and useful comments.

Ariane Siebert is thanked for preparing the geological map of Bornholm and Albrecht Schulze is thanked for the proofreading of the complete thesis.

The morning "Kaffeerunde" and all other colleagues are thanked for their friendly company and their temporary distraction from the strenuous work.

Last but not least, I would like to thank my family and friends for the support during the sometimes stressful time as a PhD. You always brought me back down to earth when I was far up in the scientific sphere. A special thanks go to Lisa and Paul, my niece and nephew, who always make me laugh.





# List of Figures

2.1	Location of the seismic study area. . . . .	6
2.2	Configuration of the vibroseis experiments. . . . .	8
2.3	Geology of Bornholm (after Graversen, 2009). . . . .	9
2.4	Lithostratigraphy of the boreholes Skelbro-1 and Skelbro-2. . . . .	11
2.5	Logging report of the borehole Skelbro-2. . . . .	14
3.1	Definition of velocity structure with grid points. . . . .	18
3.2	The pseudo-bending method of Um and Thurber (1987). . . . .	20
3.3	Examples of the raw data. . . . .	21
3.4	Effect of the rebound of the striking plate. . . . .	22
3.5	Traveltime picks for all profiles. . . . .	23
3.6	Histogram of traveltime differences for reversed shot and receiver pairs. . . . .	25
3.7	Trade-off curves. . . . .	26
3.8	Development of the graded inversion for all profiles. . . . .	28
3.9	Residual traveltimes for each inversion step. . . . .	30
3.10	Evolution of the RMS error during the iteration steps. . . . .	31
3.11	Example of a checkerboard pattern. . . . .	32
3.12	Original and resolved checkerboard patterns for three pattern sizes. . . . .	33
3.13	Distribution of the spread value for all profiles. . . . .	34
3.14	Imaging test of a high velocity layer. . . . .	35
3.15	Final P-wave velocity model for Line-1. . . . .	37
3.16	Final P-wave velocity model for Line-2. . . . .	37
3.17	Final P-wave velocity model for Line-3. . . . .	37
3.18	Final velocity models of all lines in a combined plot. . . . .	39
3.19	Comparison of velocity models with borehole logging. . . . .	40
3.20	Correlation of TOC and seismic velocities. . . . .	42
3.21	TOC values. . . . .	43
4.1	Calculated dispersion curve. . . . .	49
4.2	The Voronoi geometry. . . . .	51
4.3	Example of the SH vibroseis data after processing. . . . .	52

4.4	Theoretical dispersion curve of Line-3. . . . .	55
4.5	Resolved dispersion curves and models. . . . .	57
4.6	Result of the Love wave inversion for Line-3. . . . .	58
5.1	Phase velocity spectrum of an exemplary interferogram. . . . .	62
5.2	Crosscorrelations plotted according to the time window. . . . .	64
5.3	Differently generated interferograms of station 30. . . . .	66
5.4	Final interferograms of stations 1 and 61. . . . .	67
5.5	Final interferograms of stations 3 and 5 with P-wave arrival. . . . .	68
5.6	Comparison of the interferogram and the active seismogram. . . . .	69
6.1	Piezoelectric effect. . . . .	71
6.2	The full extracted cores Bo-AS-K3 and Bo-AS-K7. . . . .	72
6.3	Schematic setup of the ultrasonic measurements. . . . .	74
6.4	Sample, measuring unit and pressure vessel. . . . .	74
6.5	Example of recorded ultrasonic seismograms. . . . .	75
6.6	Estimation of dead time. . . . .	77
6.7	Velocities with pressure and temperature of Bo-AS-K3, axial. . . . .	79
6.8	Velocities with pressure and temperature of Bo-AS-K3, radial. . . . .	80
6.9	Velocities with pressure and temperature of Bo-AS-K7, axial. . . . .	81
6.10	Velocities with pressure and temperature of Bo-AS-K7, radial. . . . .	82
6.11	P-wave velocity anisotropy as a function of pressure and temperature. . . . .	85
6.12	The anisotropy of the velocity ratio with pressure and temperature variation. . . . .	85
6.13	Histograms of laboratory velocity anisotropy. . . . .	86
7.1	Calculation of the $v_P/v_S$ ratio with the individual results of Line-3. . . . .	92
7.2	Distribution of the $v_P/v_S$ ratio of the Alum Shale. . . . .	92
7.3	Comparison of the frequency spectra of the different data sets. . . . .	95

# List of Tables

3.1	Standard deviations $\sigma$ estimated with different methods for all profiles. . .	24
3.2	Grid spacings of the graded inversion. . . . .	27
3.3	Correlation of TOC and velocity. . . . .	42
4.1	Value ranges for the first inversion run. . . . .	54
4.2	Value ranges for the second inversion run. . . . .	54
6.1	Sample length and corresponding depth of each black shale sample. . . . .	73
6.2	Calculated dead times for P- and S-wave arrivals. . . . .	77
6.3	Average anisotropy values for both samples. . . . .	86
A.1	Pressure cycle of axial Bo-AS-K3 . . . . .	114
A.2	Temperature increase of axial Bo-AS-K3 . . . . .	115
A.3	Pressure cycle of radial Bo-AS-K3 . . . . .	117
A.4	Temperature increase of radial Bo-AS-K3 . . . . .	117
A.5	First pressure cycle of axial Bo-AS-K7 . . . . .	119
A.6	Temperature increase of axial Bo-As-K7 . . . . .	120
A.7	Second pressure cycle of axial Bo-AS-K7 . . . . .	122
A.8	First pressure cycle of radial Bo-AS-K7 . . . . .	124
A.9	Temperature increase of radial Bo-As-K7 . . . . .	124
A.10	Second pressure cycle of radial Bo-AS-K7 . . . . .	125
B.1	Anisotropy values for the pressure cycle of Bo-AS-K3. . . . .	128
B.2	Anisotropy values for the temperature increase of Bo-AS-K3. . . . .	128
B.3	Anisotropy values for the first pressure cycle of Bo-AS-K7. . . . .	130
B.4	Anisotropy values for the temperature increase of Bo-AS-K7. . . . .	130
B.5	Anisotropy values for the second pressure cycle of Bo-AS-K7. . . . .	131



## References

- Arthur, M. A., & Sageman, B. B. (1994). Marine black shales: Depositional mechanisms and environments of ancient deposits. *Annu. Rev. Earth Planet. Sci.*, *22*, 499-551.
- Astiz, M. M., Correig, A. M., & Ortiz, R. (1991). A numerical filter for the restitution of digital seismograms. *Computers & Geosciences*, *17*(7), 1009-1016.
- Baumann-Wilke, M., Bauer, K., Schovsbo, N. H., & Stiller, M. (2012). P-wave travel-time tomography for a seismic characterization of black shales at shallow depth on Bornholm, Denmark. *Geophysics*, *77*, EN53-EN60.
- Bensen, G. D., Ritzwoller, M. H., Barmin, M. P., Levshin, A. L., Moschetti, M. P., Shapiro, N. M., et al. (2007). Processing seismic ambient noise data to obtain reliable broad-band surface wave dispersion measurements. *Geophysical Journal International*, *169*, 1239-1260.
- Birch, F. (1960). The velocity of compressional waves in rocks to 10 kilobars, 1. *J. Geophys. Res.*, *65*, 1083-1102.
- Blundell, C. A. (1993). *Resolution analysis of seismic P-wave velocity estimates using reflection tomographic inversion*. Unpublished doctoral dissertation, Monash University.
- Buchardt, B., Clausen, J., & Thomsen, E. (1986). Carbon isotope composition of Lower Palaeozoic kerogen: Effects of maturation. *Organic geochemistry*, *10*, 127-134.
- Buchardt, B., & Lewan, M. D. (1990). Reflectance of vitrinite-like macerals as a thermal maturity index for Cambrian-Ordovician Alum Shale, southern Scandinavia. *AAPG Bulletin*, *74*, 394-406.
- Buchardt, B., & Nielsen, A. T. (1985). Carbon and oxygen isotope composition of Cambro-Silurian limestone and anthraconite from Bornholm: evidence for deep burial diagenesis. *Bulletin of the Geological Society of Denmark*, *33*, 415-435.
- Buchardt, B., Nielsen, A. T., & Schovsbo, N. H. (1997). Alun Skiferen i Skandinavien. *Geologisk Tidsskrift*, *3*, 1-30.
- Buchardt, B., Nielsen, A. T., & Schovsbo, N. H. (1998). Lower Palaeozoic source rocks in southern Baltoscandia. In *Perspectives of the petroleum exploration in the baltic region* (p. 53-57). P. Suveizdis and O. Zdanaviciute. (Proceedings of the International Scientific Conference, 21-24 October 1998, Vilnius)
- Bullen, K. E. (1963). *An introduction to the theory of seismology*. Cambridge Univ.

- Press.
- Campillo, M., & Paul, A. (2003). Long-range correlations in the diffuse seismic coda. *Science*, *299*, 547-549.
- Claerbout, J. F. (1968). Synthesis of a layered medium from its acoustic transmission response. *Geophysics*, *33*, 264-269.
- Curtis, A., Gerstoft, P., Sato, H., Snieder, R., & Wapenaar, K. (2006). Seismic interferometry - turning noise into signal. *The Leading Edge*, *25*, 1082-1092.
- Curtis, C. D. (1977). Sedimentary geochemistry: environments and processes dominated by involvement of an aqueous phase. *Philos. Trans. Roy. Soc. London, A* *286*, 353-372.
- Demaison, G. J., & Moore, G. T. (1980). Anoxic environments and oil source bed genesis. *Am. Assoc. Petrol. Geol. Bull.*, *64*, 1179-1209.
- Didyk, B. M., Simoneit, B. R. T., Brassell, S. C., & Eglinton, G. (1978). Organic geochemical indicators of paleoenvironmental conditions of sedimentation. *Nature*, *272*, 216-222.
- Eberhart-Phillips, D. (1986). Three-dimensional velocity structure in Northern California Coast Ranges from inversion of local earthquake arrival times. *Bull. Seismol. Soc. Am.*, *76*(4), 1025-1052.
- Eberhart-Phillips, D. (1990). Three-dimensional P and S velocity structure in the Coalinga region, California. *Journal of Geophysical Research*, *95*, 15343-15363.
- Eberhart-Phillips, D., & Reyners, M. (1997). Continental subduction and three-dimensional crustal structure: The northern South Island, New Zealand. *Journal of Geophysical Research*, *102*(11), 843-861.
- Evans, J. R., Eberhart-Phillips, D., & Thurber, C. H. (1994). User's Manual for SIMULPS12 for imaging vp and vp/vs: A derivative of the "Thurber" tomographic inversion SIMUL3 for local earthquakes and explosions. *U.S. Geological Survey Open-File Report*, *431*, 1-101.
- Geman, S., & Geman, D. (1984). Stochastic relaxation, Gibbs distribution and the Bayesian restoration of images. *IEEE Trans. Patt. Analysis Mach. Int.*, *6*, 721-741.
- Graversen, O. (2009). Structural analysis of superposed fault systems of the Bornholm horst block, Tornquist Zone, Denmark. *Bulletin of the Geological Society of Denmark*, *57*, 25-49.
- Ivanov, J., Miller, R. D., Lacombe, P., Johnson, C. D., & Lane Jr., J. W. (2006). Delineating a shallow fault zone and dipping bedrock strata using multichannel analysis of surface waves with a land streamer. *Geophysics*, *71*, A39-A42.
- Iyer, H. M., & Hirahara, K. (1993). *Seismic tomography: Theory and practice*. Chapman & Hall.

- Jaanusson, V. (1963). Classification of the Harjuan (Upper Ordovician) rocks of the mainland of Sweden. *Geologiska Föreningens i Stockholm Förhandlingar*, 85, 110-114.
- Jensenius, J. (1987). Regional studies of fluid inclusions in Paleozoic sediments from southern Scandinavia. *Bulletin of the Geological Society of Denmark*, 36, 221-235.
- Johnston, D. H. (1987). Physical properties of shale at temperature and pressure. *Geophysics*, 52(10), 1391-1401.
- Johnston, J. E., & Christensen, N. I. (1995). Seismic anisotropy of shales. *Journal of Geophysical Research*, 100(B4), 5991-6003.
- Jones, L. E. A., & Wang, H. F. (1981). Ultrasonic velocities in Cretaceous shales from the Williston basin. *Geophysics*, 46(3), 288-297.
- Julian, B. R., & Gubbins, D. (1977). Three-dimensional seismic ray tracing. *Journal of Geophysics*, 43, 95-113.
- Koren, T., & Bjerreskov, M. (1997). Early Llandovery monograptids from Bornholm and the southern Urals: taxonomy and evolution. *Bulletin of the Geological Society of Denmark*, 44, 1-43.
- Kumar, D., & Hoversten, G. M. (2012). Geophysical model response in a shale gas. *Geohorizons*, 17, 31-37.
- Larose, E., Derode, A., Campillo, M., & Fink, M. (2004). Imaging from one-bit correlations of wideband diffuse wave fields. *Journal of Applied Physics*, 95, 8393-8399.
- Lee, W. H. K., & Pereya, V. (1993). Mathematical introduction to seismic tomography. In *Seismic tomography: Theory and practice*. H. M. Iyer and K. Hirahara.
- Lee, Y. W. (1960). *Statistical Theory of Communication*. Wiley, New York.
- Liboriussen, J., Ashton, P., & Tygesen, T. (1987). The tectonic evolution of the Fennoscandian Border Zone in Denmark. *Tectonophysics*, 137, 21-29.
- Manen, D. van, Curtis, A., & Robertsson, J. (2006). Interferometric modeling of wave propagation in inhomogeneous elastic media using time reversal and reciprocity. *Geophysics*, 71, SI47-SI60.
- Meissner, F. F. (1984). Petroleum geology of the Bakken Formation, Williston basin, North Dakota and Montana. *AAPG Memoir*, 35, 159-179.
- Menke, W. (1989). *Geophysical Data Analysis: Discrete Inverse Theory*. Academic Press, Orlando.
- Meyers, P. A., & Mitterer, R. M. (1986). Introduction and overview. *Marine Geology*, 70, 1-8.
- Michelini, A., & McEvelly, T. V. (1991). Seismological studies at Parkfield, I, Simultaneous inversion for velocity structure and hypocenters using cubic b-splines parameterization. *Bull. Seismol. Soc. Am.*, 81, 524-552.
- Michelsen, O., & Nielsen, L. H. (1993). Structural development of the Fennoscandian

- Border Zone, offshore Denmark. *Marine and Petroleum Geology*, 10, 124-134.
- Nazarian, S., Stokoe, K. H., & Hudson, W. R. (1983). Use of spectral analysis of surface waves method for determination of moduli and thicknesses of pavement systems. *Transport. Res. Record*, 930, 38-45.
- Nicolson, H., Curtis, A., Baptie, B., & Galetti, E. (2011). Seismic interferometry and ambient noise tomography in the British Isles. *Proceedings of the Geologists' Association*, 123, 74-86.
- Nielsen, A. T., & Schovsbo, N. H. (2006). Cambrian to basal Ordovician lithostratigraphy in southern Scandinavia. *Bulletin of the Geological Society of Denmark*, 53, 47-92.
- Park, C. B., Miller, R. D., & Xia, J. (1999). Multichannel analysis of surface waves. *Geophysics*, 64, 800-808.
- Park, C. B., Xia, J., & Miller, R. D. (1998). Ground roll as a tool to image near-surface anomaly. *68th Ann. Internat. Mtg, Soc. Expl. Geophys., Expanded Abstracts*, 874-877.
- Pedersen, G. K. (1989). The sedimentology of Lower Palaeozoic black shales from the shallow wells Skelbro 1 and Billegrav 1, Bornholm, Denmark. *Bulletin of the Geological Society of Denmark*, 37, 151-173.
- Pedersen, G. K., & Klitten, K. (1990). Anvendelse af gamma-logs ved correlation af marine skifre i vandforsyningsboringer på bornholm. *Danmarks Geologisk Forening Årskrift 1987-89*, 21-35.
- Prasad, M., Pal-Bathija, A., Johnston, M., Rydzy, M., & Batzle, M. (2009). Rock physics of the unconventional. *The Leading Edge*, 28(1), 34-38.
- Rashed, M., & Nakagawa, K. (2006). The effect of different CMP stacking techniques on signal-to-noise ratio of seismic data: two examples from Osaka and Nara, Japan. *Journal of Geosciences*, 49(1), 1-10.
- Rawlinson, N., & Sambridge, M. (2003). Seismic travelttime tomography of the crust and lithosphere. *Advances in Geophysics*, 46, 81-197.
- Rickett, J., & Claerbout, J. (1999). Acoustic daylight imaging via spectral factorization: Helioseismology and reservoir monitoring. *The Leading Edge*, 18, 957-960.
- Rothman, D. H. (1985). Nonlinear inversion, statistical mechanics, and residual statics estimation. *Geophysics*, 50, 2784-2796.
- Rothman, D. H. (1986). Automatic estimation of large residual static corrections. *Geophysics*, 51, 332-346.
- Roux, P., Sabra, K. G., Gerstoft, P., Kuperman, W. A., & Fehler, M. C. (2005). P-waves from cross-correlation of seismic noise. *Geophysical Research Letters*, 32, L19303.
- Sabra, K. G., Gerstoft, P., Roux, P., Kuperman, W. A., & Fehler, M. C. (2005). Surface wave tomography from microseisms in southern California. *Geophysical Research Letters*, 32, L14311.



- Sambridge, M. (1999). Geophysical inversion with a neighbourhood algorithm - I. Searching the parameter space. *Geophys. J. Int.*, *138*, 479-494.
- Sambridge, M., & Drijkoningen, G. G. (1992). Genetic algorithms in seismic waveform inversion. *Geophys. J. Int.*, *109*, 323-342.
- Sambridge, M., & Kennett, B. L. N. (1990). Boundary value ray tracing in a heterogeneous medium: A simple and versatile algorithm. *Geophysical Journal International*, *101*, 157-168.
- Saygin, E., & Kennett, B. L. N. (2010). Ambient seismic noise tomography of Australian continent. *Tectonophysics*, *481*, 116-125.
- Scherbaum, F., Hinzen, K.-G., & Ohrnberger, M. (2003). Determination of shallow shear wave velocity profiles in the Cologne/Germany area using ambient vibrations. *Geophys. J. Int.*, *152*, 597-612.
- Schovsbo, N. H. (2002). Uranium enrichment shorewards in black shales: A case study from the Skandinavian Alum Shale. *GFF*, *124*, 107-115.
- Schovsbo, N. H. (2011). Geochemical and stratigraphical evaluation of the Lower Palaeozoic Shales on Bornholm: The Skelbro-1 and -2 and Billegrav-1 and -2 wells. *GEUS Report*.
- Schovsbo, N. H., Nielsen, A. T., Klitten, K., Mathiesen, A., & Rasmussen, P. (2011). Shale gas investigations in Denmark: Lower Palaeozoic shales on Bornholm. *Geological Survey of Denmark and Greenland Bulletin*, *23*, 9-12.
- Sen, M. K., & Stoffa, P. L. (1991). Nonlinear one-dimensional seismic waveform inversion using simulated annealing. *Geophysics*, *56*, 1624-1638.
- Shapiro, N. M., Campillo, M., Stehly, L., & Ritzwoller, M. H. (2005). High-resolution surface wave tomography from ambient seismic noise. *Science*, *307*, 1615-1617.
- Sharma, P. V. (1974). A note on seismic velocities of rock formations on bornholm. *Bulletin of the Geological Society of Denmark*, *23*, 191-196.
- Snieder, R. (2004). Extracting the Green's function from the correlation of coda waves: A derivation based on stationary phase. *Physical Review E*, *69*, 046610.
- Socco, L. V., Foti, S., & Boiero, D. (2010). Surface-wave analysis for building near-surface velocity models - Established approaches and new perspectives. *Geophysics*, *75*, 75A83-75A102.
- Sorgenfrei, T., & Buch, A. (1964). Deep tests in Denmark, 1935-1959. *Danm. Geol. Unders., III Række*, *36*, 146 pp.
- Stokoe, K. H., Wright, G. W., James, A. B., & Jose, M. R. (1994). Characterization of geotechnical sites by SASW method. In *Geophysical characterization of sites*. R. D. Woods.
- Stouge, S., & Nielsen, A. T. (2003). An integrated biostratigraphical analysis of the Volkhov-Kunda (Lower Ordovician) succession at Fågelsång, Scania, Sweden. *Bul-*

- letin of the Geological Society of Denmark*, 50, 75-94.
- Thurber, C. (1983). Earthquake locations and three-dimensional crustal structure in the Coyote Lake area, central California. *Journal of Geophysical Research*, 88, 8226-8236.
- Thurber, C., & Eberhart-Phillips, D. (1999). Local earthquake tomography with flexible gridding. *Computational Geosciences*, 25, 809-818.
- Thurber, C., & Ellsworth, W. L. (1980). Rapid solution of ray tracing problems in heterogeneous media. *Bulletin of the Seismological Society of America*, 70, 1137-1148.
- Toomey, D. R., & Foulger, G. (1989). Tomographic inversion of local earthquake data from the Hengill-Grensdalur central volcano complex, Iceland. *Journal of Geophysical Research*, 94, 17497-17510.
- Tourtelot, H. A. (1979). Black shales - its deposition and diagenesis. *Clays and Clay Minerals*, 27, 313-321.
- Červený, V. (1993). Ray tracing algorithms in three-dimensional laterally layered structures. In: *Seismic tomography: With applications in global seismology and exploration geophysics*, D. Reidel.
- Um, J., & Thurber, C. (1987). A fast algorithm for two-point seismic ray tracing. *Bulletin of the Seismological Society of America*, 77, 972-986.
- Vanorio, T., Mukerji, T., & Mavko, G. (2008). Emerging methodologies to characterize the rock physics properties of organic-rich shales. *The Leading Edge*, 27(6), 780-787.
- Vejbæk, O., Stouge, S., & Poulsen, K. D. (1994). Palaeozoic tectonic and sedimentary evolution and hydrocarbon prospectivity in the Bornholm area. *Geological Survey of Denmark*, A34, 1-23.
- Vernik, L., & Liu, X. (1997). Velocity anisotropy in shales: A petrophysical study. *Geophysics*, 62(2), 521-532.
- Walker, J. S. (1996). *Fast Fourier Transforms*. CRC Press.
- Wang, Z. (2002). Seismic anisotropy in sedimentary rocks, part 2: Laboratory data. *Geophysics*, 67(5), 1423-1440.
- Wapenaar, K. (2003). Synthesis of an inhomogeneous medium from its acoustic transmission response. *Geophysics*, 68, 1756-1759.
- Wapenaar, K. (2004). Retrieving the elastodynamic Green's function of an arbitrary inhomogeneous medium by crosscorrelation. *Physical Review Letters*, 93, 254301.
- Wapenaar, K., & Fokkema, J. (2006). Green's function representations for seismic interferometry. *Geophysics*, 71, SI133-SI144.
- Wathelet, M. (2005). *Array recordings of ambient vibrations: Surface wave inversion*. Unpublished doctoral dissertation, Liège Univ., Liège, Belgium.

- Wathelet, M. (2008). An improved neighborhood algorithm: parameter conditions and dynamic scaling. *Geophys. Res. Lett.*, *35*, L09301.
- Wathelet, M., Jongmans, D., & Ohrnberger, M. (2004). Surface-wave inversion using a direct search algorithm and its application to ambient vibration measurements. *Near Surface Geophysics*, *2*, 211-221.
- Weaver, R. L., & Lobkis, O. I. (2001). Ultrasonics without a Source: thermal fluctuation correlations at MHz frequencies. *Physical Review Letters*, *87*, 134301.
- Weissert, H. (1981). The environment of deposition of black shales in the Early Cretaceous: An ongoing controversy. *SEPM, Spec. Publ.*, *32*, 547-560.
- Woodring, W. P. (1954). Conference on biochemistry, paleoecology, and evolution. *Natl. Acad. Sci.*, *40*, 219-224.
- Zelt, C. A. (1998). Lateral velocity resolution from three-dimensional seismic refraction data. *Geophysical Journal International*, *135*, 1101-1112.
- Zhu, Y., Liu, E., Martinez, A., Payne, M. A., & Harris, C. E. (2011). Understanding geophysical responses of shale-gas plays. *The Leading Edge*, *30*, 332-338.



# Appendix A - Velocity data of ultrasonic measurements

## Sample Bo-AS-K3, axial

### Pressure cycle

$\vartheta$ in °C	p in MPa	$t_P$ in $\mu$ s	$t_S$ in $\mu$ s	$v_P$ in m/s	$v_S$ in m/s	$v_P/v_S$
20	2	–	46.27	–	1955.96	–
20	4	–	46.24	–	1957.93	–
20	6	–	46.17	–	1963.80	–
20	8	29.02	46.16	2969.05	1964.61	1.511
20	10	28.96	46.10	2981.54	1970.49	1.513
20	12	28.88	46.04	2996.58	1975.65	1.517
20	14	28.81	45.98	3010.13	1980.64	1.520
20	16	28.76	45.92	3020.14	1986.20	1.521
20	18	28.66	45.78	3041.54	1998.16	1.522
20	20	28.62	45.76	3048.88	1999.66	1.525
20	22	28.60	45.74	3053.92	2001.88	1.526
20	24	28.57	45.70	3060.30	2004.93	1.526
20	26	–	45.68	–	2007.37	–
20	28	28.50	45.65	3074.94	2009.94	1.530
20	30	28.45	45.60	3084.24	2014.13	1.531
20	32	28.42	45.58	3092.36	2016.36	1.534
20	34	28.38	45.55	3099.74	2018.62	1.536
20	36	28.35	45.52	3107.57	2021.71	1.537
20	38	28.31	–	3116.21	–	–
20	40	28.27	45.49	3123.80	2024.36	1.543
20	38	28.29	45.46	3120.26	2026.66	1.540
20	36	28.31	45.49	3115.86	2024.63	1.539

Table A.1: (continued on next page)

$\vartheta$ in °C	p in MPa	$t_P$ in $\mu\text{s}$	$t_S$ in $\mu\text{s}$	$v_P$ in m/s	$v_S$ in m/s	$v_P/v_S$
20	34	28.33	45.50	3110.59	2023.05	1.538
20	32	28.36	45.53	3104.71	2021.16	1.536
20	30	28.38	45.55	3100.01	2019.32	1.535
20	28	28.41	45.57	3094.37	2017.45	1.534
20	26	28.44	45.59	3086.49	2015.41	1.531
20	24	28.47	45.62	3080.62	2012.86	1.530
20	22	28.50	45.65	3074.12	2009.70	1.530
20	20	28.54	45.68	3066.83	2007.16	1.528
20	18	28.57	45.71	3059.67	2004.08	1.527
20	16	28.60	45.75	3053.59	2000.89	1.526
20	14	28.63	45.79	3046.60	1997.66	1.525
20	12	28.67	45.83	3040.24	1993.72	1.525
20	10	28.71	45.88	3031.33	1989.22	1.524
20	8	28.74	45.94	3024.62	1983.81	1.525
20	6	28.78	46.01	3016.14	1977.88	1.525
20	4	–	46.08	–	1971.45	–
20	2	–	46.15	–	1966.12	–

**Table A.1:** Ultrasonic traveltimes, calculated velocities and the velocity ratio for the pressure cycle of the axial sample Bo-AS-K3. The temperature remained constant during the measurement. The gaps in the table are due to errors in recording the wavelets or due to difficulties in picking the arrival times.

## Temperature increase

$\vartheta$ in °C	p in MPa	$t_P$ in $\mu\text{s}$	$t_S$ in $\mu\text{s}$	$v_P$ in m/s	$v_S$ in m/s	$v_P/v_S$
20	12	28.67	45.83	3040.24	1993.72	1.525
30	12	28.87	46.09	2999.14	1971.38	1.521
40	12	28.99	46.28	2975.65	1954.60	1.522
50	12	29.11	46.47	2952.17	1938.84	1.523
60	12	29.23	46.68	2927.40	1921.18	1.524
70	12	29.36	46.88	2903.56	1905.05	1.524
80	12	29.44	47.04	2888.36	1891.82	1.527

**Table A.2:** Ultrasonic traveltimes, calculated velocities and and the velocity ration for increasing temperature for the axial sample Bo-AS-K3. The pressure remained constant at 12 MPa.

## Sample Bo-AS-K3, radial

### Pressure cycle

$\vartheta$ in °C	p in MPa	$t_P$ in $\mu$ s	$t_S$ in $\mu$ s	$v_P$ in m/s	$v_S$ in m/s	$v_P/v_S$
20	2	23.6923	46.8521	4329.77	1866.27	2.320
20	4	23.6722	46.7550	4338.25	1873.90	2.315
20	6	23.6392	46.6477	4352.25	1882.40	2.312
20	8	23.6111	46.6018	4364.24	1886.06	2.314
20	10	23.5833	46.5527	4376.16	1889.99	2.315
20	12	23.5618	46.5069	4385.43	1893.67	2.316
20	14	23.5250	46.4593	4401.38	1897.51	2.320
20	16	23.5080	46.4494	4408.79	1898.31	2.322
20	18	23.4825	46.4360	4419.96	1899.40	2.327
20	20	23.4720	46.4310	4424.57	1899.80	2.329
20	22	23.4616	46.4187	4429.15	1900.80	2.330
20	24	23.4512	46.3964	4433.73	1902.61	2.330
20	26	23.4330	46.3665	4441.78	1905.05	2.332
20	28	23.4173	46.3341	4448.75	1907.69	2.332
20	30	23.4042	46.3049	4454.58	1910.08	2.332
20	32	23.3913	46.2723	4460.34	1912.76	2.332
20	34	23.3813	46.2424	4464.81	1915.22	2.331
20	36	23.3717	46.2132	4469.12	1917.63	2.331
20	38	23.3627	46.1837	4473.16	1920.07	2.330
20	40	23.3538	46.1537	4477.16	1922.55	2.329
20	38	23.3520	46.1404	4477.97	1923.66	2.328
20	36	23.3549	46.1439	4476.67	1923.37	2.328
20	34	23.3597	46.1558	4474.51	1922.38	2.328
20	32	23.3655	46.1726	4471.90	1920.99	2.328
20	30	23.3722	46.1922	4468.89	1919.36	2.328
20	28	23.3796	46.2131	4465.58	1917.63	2.329
20	26	23.3888	46.2348	4461.46	1915.84	2.329
20	24	23.4000	46.2607	4456.46	1913.71	2.329
20	22	23.4109	46.2849	4451.60	1911.72	2.329
20	20	23.4247	46.3075	4445.47	1909.87	2.328
20	18	23.4426	46.3306	4437.53	1907.98	2.326

**Table A.3:** (continued on next page)

$\vartheta$ in °C	p in MPa	$t_P$ in $\mu\text{s}$	$t_S$ in $\mu\text{s}$	$v_P$ in m/s	$v_S$ in m/s	$v_P/v_S$
20	16	23.4581	46.3492	4430.69	1906.46	2.324
20	14	23.4692	46.3567	4425.80	1905.85	2.322
20	12	23.4892	46.3767	4417.02	1904.22	2.320
20	10	23.5147	46.4017	4405.87	1902.18	2.316
20	8	23.5512	46.4409	4390.01	1899.00	2.312
20	6	23.5804	46.5024	4377.41	1894.03	2.311
20	4	23.6120	46.5701	4363.85	1888.59	2.311
20	2	23.6527	46.6458	4346.51	1882.55	2.309

**Table A.3:** Ultrasonic traveltimes, calculated velocities and the velocity ratio for the pressure cycle of the radial sample Bo-AS-K3. The temperature remained constant during the measurement.

## Temperature increase

$\vartheta$ in °C	p in MPa	$t_P$ in $\mu\text{s}$	$t_S$ in $\mu\text{s}$	$v_P$ in m/s	$v_S$ in m/s	$v_P/v_S$
20	12	23.4985	46.3721	4412.95	1904.59	2.317
30	12	23.6019	46.6121	4368.17	1885.23	2.317
40	12	23.6723	46.8197	4338.21	1868.81	2.321
50	12	23.7355	47.0023	4311.66	1854.59	2.325
60	12	23.8109	47.2142	4280.40	1838.36	2.328
70	12	23.8825	47.4335	4251.13	1821.86	2.333

**Table A.4:** Ultrasonic traveltimes, calculated velocities and the velocity ratio for the pressure cycle of the radial sample Bo-AS-K3. The pressure remained constant at 12 MPa.



## Sample Bo-AS-K7, axial

### First pressure cycle

$\vartheta$ in °C	p in MPa	$t_P$ in $\mu\text{s}$	$t_S$ in $\mu\text{s}$	$v_P$ in m/s	$v_S$ in m/s	$v_P/v_S$
20	2	34.1030	–	2768.67	–	–
20	4	34.0599	–	2774.52	–	–
20	6	34.0080	–	2781.60	–	–
20	8	33.9570	–	2788.59	–	–
20	10	33.9067	–	2795.52	–	–
20	12	33.8617	–	2801.74	–	–
20	14	33.8076	–	2809.27	–	–
20	16	33.7575	–	2816.27	–	–
20	18	33.7074	–	2823.31	–	–
20	20	33.6590	–	2830.14	–	–
20	22	33.6103	–	2837.05	–	–
20	24	33.5580	–	2844.51	–	–
20	26	33.5067	–	2851.86	–	–
20	28	33.4551	–	2859.29	–	–
20	30	33.4103	–	2865.78	–	–
20	32	33.3618	–	2872.83	–	–
20	34	33.3161	–	2879.51	–	–
20	36	33.2700	–	2886.28	–	–
20	38	33.2239	–	2893.08	–	–
20	40	33.1783	–	2899.84	–	–
20	42	33.1390	–	2905.69	–	–
20	44	33.0897	–	2913.07	–	–
20	46	33.0530	–	2918.58	–	–
20	48	33.0077	–	2925.41	–	–
20	50	32.9695	–	2931.20	–	–
20	48	32.9674	–	2931.52	–	–
20	46	32.9865	–	2928.62	–	–
20	44	33.0151	–	2924.29	–	–
20	42	33.0463	–	2919.59	–	–
20	40	33.0772	–	2914.94	–	–
20	38	33.1099	–	2910.04	–	–
20	36	33.1453	–	2904.75	–	–

**Table A.5:** (continued on next page)

$\vartheta$ in °C	p in MPa	$t_P$ in $\mu$ s	$t_S$ in $\mu$ s	$v_P$ in m/s	$v_S$ in m/s	$v_P/v_S$
20	34	33.1819	–	2899.31	–	–
20	32	33.2161	–	2894.24	–	–
20	30	33.2537	–	2888.68	–	–
20	28	33.2939	–	2882.77	–	–
20	26	33.3320	–	2877.19	–	–
20	24	33.3765	–	2870.69	–	–
20	22	33.4177	–	2864.71	–	–
20	20	33.4625	–	2858.22	–	–
20	18	33.5091	–	2851.51	–	–
20	16	33.5576	–	2844.56	–	–
20	14	33.6092	–	2837.21	–	–
20	12	33.6643	–	2829.39	–	–
20	10	33.7213	–	2821.35	–	–
20	8	33.7830	–	2812.70	–	–
20	6	33.8485	–	2803.58	–	–
20	4	33.9171	–	2794.08	–	–
20	2	33.9905	–	2783.99	–	–

**Table A.5:** Ultrasonic traveltimes, calculated velocities and the velocity ratio for the first pressure cycle of the axial sample Bo-AS-K7 at constant temperature 20 °C. It was impossible to identify any S-wave arrival for this pressure cycle.

## Temperature increase

$\vartheta$ in °C	p in MPa	$t_P$ in $\mu\text{s}$	$t_S$ in $\mu\text{s}$	$v_P$ in m/s	$v_S$ in m/s	$v_P/v_S$
20	2	33.9841	–	2784.87	–	–
25	2	34.0679	54.0759	2773.44	1899.59	1.4600
30	2	34.1608	54.2681	2760.87	1887.42	1.4628
35	2	34.2759	54.3860	2745.45	1880.02	1.4603
40	2	34.3645	54.5583	2733.71	1869.33	1.4624
45	2	34.4628	54.6902	2720.79	1861.22	1.4618
50	2	34.5575	54.8167	2708.46	1853.51	1.4613
55	2	34.6337	54.9057	2698.62	1848.12	1.4602
60	2	34.7194	55.0336	2687.64	1840.43	1.4603
65	2	34.8128	55.2132	2675.77	1829.75	1.4624
70	2	34.9109	55.3431	2663.42	1822.10	1.4617
75	2	34.9977	55.4431	2652.58	1816.25	1.4605
80	2	35.0875	55.5254	2641.47	1811.47	1.4582

**Table A.6:** Ultrasonic traveltimes, calculated velocities and the velocity ratio for increasing temperature of the axial sample Bo-AS-K7. The pressure remained constant at 2 MPa.

## Second pressure cycle

$\vartheta$ in °C	p in MPa	$t_P$ in $\mu\text{s}$	$t_S$ in $\mu\text{s}$	$v_P$ in m/s	$v_S$ in m/s	$v_P/v_S$
80	2	34.6469	–	2696.92	–	–
80	4	34.6831	–	2692.28	–	–
80	6	34.7173	–	2687.90	–	–
80	8	34.7612	–	2682.31	–	–
80	10	34.6975	55.3236	2690.43	1823.24	1.4756
80	12	34.6394	55.2944	2697.88	1824.96	1.4783
80	14	34.5500	55.2340	2709.43	1828.52	1.4818
80	16	34.5241	55.2143	2712.79	1829.68	1.4827
80	18	34.4811	55.1950	2718.40	1830.83	1.4848
80	20	34.4302	55.1564	2725.06	1833.12	1.4866

**Table A.7:** (continued on next page)

$\vartheta$ in °C	p in MPa	$t_P$ in $\mu$ s	$t_S$ in $\mu$ s	$v_P$ in m/s	$v_S$ in m/s	$v_P/v_S$
80	22	34.3819	55.1415	2731.41	1834.00	1.4893
80	24	34.2851	55.0543	2744.23	1839.20	1.4921
80	26	34.2417	55.0192	2750.02	1841.30	1.4935
80	28	34.1917	54.9542	2756.71	1845.20	1.4940
80	30	34.1327	54.9130	2764.66	1847.68	1.4963
80	32	34.0848	54.8757	2771.14	1849.93	1.4980
80	34	34.0344	54.8328	2778.00	1852.53	1.4996
80	36	33.9856	54.7919	2784.67	1855.01	1.5012
80	38	33.9336	54.7500	2791.81	1857.56	1.5029
80	40	33.8847	54.7084	2798.56	1860.10	1.5045
80	42	33.8372	54.6702	2805.15	1862.44	1.5062
80	44	33.7884	54.6321	2811.95	1864.78	1.5079
80	46	33.7425	54.5867	2818.37	1867.57	1.5091
80	48	33.6915	54.5518	2825.55	1869.73	1.5112
80	50	33.6500	54.5073	2831.42	1872.48	1.5121
80	48	33.6485	54.4894	2831.63	1873.59	1.5113
80	46	33.6711	54.5070	2828.43	1872.50	1.5105
80	44	33.7016	54.5361	2824.13	1870.70	1.5097
80	42	33.7382	54.5659	2818.98	1868.86	1.5084
80	40	33.7737	54.6103	2814.00	1866.12	1.5079
80	38	33.8131	54.6444	2808.50	1864.02	1.5067
80	36	33.8563	54.6837	2802.49	1861.62	1.5054
80	34	33.8981	54.7214	2796.71	1859.31	1.5042
80	32	33.9451	54.7601	2790.23	1856.95	1.5026
80	30	33.9914	54.8006	2783.87	1854.49	1.5012
80	28	34.0394	54.8467	2777.31	1851.69	1.4999
80	26	34.0894	54.8917	2770.52	1848.97	1.4984
80	24	34.1414	54.9505	2763.48	1845.42	1.4975
80	22	34.1945	54.9903	2756.34	1843.03	1.4955
80	20	34.2514	55.0401	2748.72	1840.05	1.4938
80	18	34.3098	55.0938	2740.95	1836.84	1.4922
80	16	34.3691	55.1527	2733.10	1833.33	1.4908

Table A.7: (continued on next page)

$\vartheta$ in °C	p in MPa	$t_P$ in $\mu\text{s}$	$t_S$ in $\mu\text{s}$	$v_P$ in m/s	$v_S$ in m/s	$v_P/v_S$
80	14	34.4314	55.2093	2724.90	1829.98	1.4890
80	12	34.4952	55.2623	2716.56	1826.85	1.4870
80	10	34.5613	55.3095	2707.97	1824.07	1.4846
80	8	34.6270	55.3618	2699.48	1821.00	1.4824
80	6	34.7000	55.3952	2690.11	1819.05	1.4789
80	4	34.7607	55.3500	2682.38	1821.69	1.4725
80	2	34.7718	55.4274	2680.97	1817.17	1.4754

**Table A.7:** Ultrasonic traveltimes, calculated velocities and the velocity ratio for the second pressure cycle of the axial sample Bo-AS-K7 at a temperature of 80°C.

## Sample Bo-AS-K7, radial

### First pressure cycle

$\vartheta$ in °C	p in MPa	$t_P$ in $\mu\text{s}$	$t_S$ in $\mu\text{s}$	$v_P$ in m/s	$v_S$ in m/s	$v_P/v_S$
20	2	24.6087	48.2343	4082.68	1866.05	2.188
20	4	24.5855	47.9934	4091.35	1885.01	2.170
20	6	24.5541	47.9020	4103.14	1892.30	2.168
20	8	24.5175	47.7248	4116.97	1906.61	2.159
20	10	24.4932	47.6752	4126.20	1910.65	2.160
20	12	24.4583	47.6205	4139.54	1915.13	2.161
20	14	24.4239	47.5639	4152.77	1919.78	2.163
20	16	24.3928	47.5087	4164.80	1924.34	2.164
20	18	24.3669	47.4680	4174.88	1927.72	2.166
20	20	24.3439	47.4326	4183.87	1930.67	2.167
20	22	24.3250	47.4000	4191.28	1933.39	2.168
20	24	24.3050	47.4265	4199.15	1931.18	2.174
20	26	24.2863	47.3745	4206.54	1935.53	2.173
20	28	24.2719	47.3587	4212.25	1936.85	2.175
20	30	24.2566	47.3220	4218.33	1939.94	2.174
20	32	24.2346	47.2722	4227.11	1944.14	2.174
20	34	24.2269	47.2641	4230.19	1944.82	2.175
20	36	24.2152	47.2287	4234.88	1947.82	2.174
20	38	24.2023	47.2126	4240.06	1949.19	2.175
20	40	24.1905	47.1881	4244.81	1951.27	2.175
20	38	24.1899	47.1842	4245.05	1951.61	2.175
20	36	24.1957	47.1877	4242.72	1951.31	2.174
20	34	24.2040	47.2037	4239.38	1949.95	2.174
20	32	24.2127	47.2324	4235.88	1947.51	2.175
20	30	24.2235	47.2475	4231.55	1946.23	2.174
20	28	24.2341	47.2680	4227.31	1944.49	2.174
20	26	24.2459	47.2969	4222.60	1942.05	2.174
20	24	24.2591	47.3285	4217.34	1939.39	2.175
20	22	24.2742	47.3584	4211.34	1936.88	2.174
20	20	24.2902	47.2937	4205.00	1942.32	2.165
20	18	24.2953	47.3196	4202.98	1940.14	2.166
20	16	24.3174	47.3602	4194.27	1936.72	2.166

**Table A.8:** (continued on next page)

$\vartheta$ in °C	p in MPa	$t_P$ in $\mu\text{s}$	$t_S$ in $\mu\text{s}$	$v_P$ in m/s	$v_S$ in m/s	$v_P/v_S$
20	14	24.3455	47.4211	4183.24	1931.63	2.166
20	12	24.3767	47.5198	4171.06	1923.42	2.169
20	10	24.4099	47.5674	4158.18	1919.49	2.166
20	8	24.4496	47.6577	4142.88	1912.08	2.167
20	6	24.4882	47.7125	4128.11	1907.61	2.164
20	4	24.5199	47.7442	4116.06	1905.03	2.161
20	2	24.5609	47.9328	4100.58	1889.84	2.170

**Table A.8:** Ultrasonic traveltimes, calculated velocities and the velocity ratio for the first pressure cycle of the radial sample Bo-AS-K7 at a temperature of 20 °C.

### Temperature increase

$\vartheta$ in °C	p in MPa	$t_P$ in $\mu\text{s}$	$t_S$ in $\mu\text{s}$	$v_P$ in m/s	$v_S$ in m/s	$v_P/v_S$
20	2	24.5611	47.9547	4100.50	1888.09	2.172
30	2	24.6379	48.2020	4071.82	1868.57	2.179
40	2	24.7262	48.4795	4039.33	1847.15	2.187
50	2	24.8064	48.7070	4010.26	1829.94	2.191
60	2	24.8925	48.9047	3979.52	1815.25	2.192
70	2	24.9856	49.1134	3946.81	1800.00	2.193
80	2	25.0483	49.2686	3925.08	1788.82	2.194

**Table A.9:** Ultrasonic traveltimes, calculated velocities and the velocity ratio for increasing temperature of the radial sample Bo-AS-K7. The pressure remained constant at 2 MPa.

### Second pressure cycle

$\vartheta$ in °C	p in MPa	$t_P$ in $\mu\text{s}$	$t_S$ in $\mu\text{s}$	$v_P$ in m/s	$v_S$ in m/s	$v_P/v_S$
80	2	25.0483	49.2686	3925.08	1788.82	2.194
80	4	25.0233	49.1491	3933.72	1797.41	2.189
80	6	24.9957	49.0682	3943.29	1803.28	2.187
80	8	24.9617	48.9900	3955.16	1808.98	2.186
80	10	24.9278	48.9293	3967.06	1813.44	2.188
80	12	24.8792	48.8351	3984.24	1820.40	2.189

**Table A.10:** (continued on next page)

$\vartheta$ in °C	p in MPa	$t_P$ in $\mu$ s	$t_S$ in $\mu$ s	$v_P$ in m/s	$v_S$ in m/s	$v_P/v_S$
80	14	24.8539	48.7875	3993.25	1823.93	2.189
80	16	24.8293	48.7623	4002.04	1825.81	2.192
80	18	24.8060	48.7222	4010.41	1828.80	2.193
80	20	24.7869	48.6755	4017.29	1832.31	2.192
80	22	24.7576	48.6133	4027.90	1836.99	2.193
80	24	24.7417	48.5864	4033.68	1839.02	2.193
80	26	24.7277	48.5603	4038.78	1841.00	2.194
80	28	24.7050	48.5130	4047.08	1844.59	2.194
80	30	24.6883	48.4839	4053.21	1846.81	2.195
80	32	24.6405	48.3825	4070.85	1854.58	2.195
80	34	24.6321	48.3936	4073.97	1853.73	2.198
80	36	24.6235	48.3854	4077.17	1854.36	2.199
80	38	24.6136	48.3704	4080.85	1855.51	2.199
80	40	24.5984	48.3571	4086.52	1856.54	2.201
80	38	24.6027	48.3732	4084.92	1855.30	2.202
80	36	24.6110	48.3972	4081.82	1853.45	2.202
80	34	24.6198	48.3943	4078.54	1853.67	2.200
80	32	24.6295	48.4307	4074.94	1850.88	2.202
80	30	24.6396	48.4208	4071.19	1851.64	2.199
80	28	24.6518	48.4413	4066.67	1850.07	2.198
80	26	24.6649	48.4511	4061.83	1849.32	2.196
80	24	24.6803	48.4581	4056.15	1848.78	2.194
80	22	24.6961	48.4880	4050.34	1846.50	2.194
80	20	24.7145	48.5226	4043.60	1843.86	2.193
80	18	24.7338	48.5605	4036.55	1840.98	2.193
80	16	24.7575	48.5937	4027.93	1838.47	2.191
80	14	24.7843	48.6357	4018.23	1835.30	2.189
80	12	24.8071	48.6745	4010.01	1832.38	2.188
80	10	24.8454	48.7557	3996.28	1826.30	2.188
80	8	24.8879	48.8385	3981.15	1820.14	2.187
80	6	24.9368	48.9232	3963.89	1813.89	2.185
80	4	24.9864	49.0398	3946.53	1805.35	2.186
80	2	25.0297	49.1771	3931.50	1795.39	2.190

**Table A.10:** Ultrasonic traveltimes, the velocities and the velocity ratio for the second pressure cycle of the radial sample Bo-AS-K7 at a temperature of 80 °C.



# Appendix B - Calculated anisotropy values

## Sample Bo-AS-K3

### Pressure cycle

$\vartheta$ in °C	p in MPa	$A_P$ in %	$A_S$ in %	$A_{P/S}$ in %
20	8	31.97	4.16	34.69
20	10	31.87	4.26	34.65
20	12	31.67	4.33	34.51
20	14	31.61	4.38	34.48
20	16	31.50	4.63	34.53
20	18	31.19	5.20	34.59
20	20	31.09	5.26	34.53
20	22	31.05	5.32	34.53
20	24	30.98	5.38	34.50
20	28	30.88	5.36	34.40
20	30	30.76	5.45	34.34
20	32	30.67	5.42	34.23
20	34	30.57	5.40	34.13
20	36	30.47	5.43	34.05
20	40	30.23	5.30	33.74
20	38	30.32	5.35	33.86
20	36	30.40	5.26	33.88
20	34	30.48	5.24	33.94
20	32	30.57	5.21	34.01
20	30	30.63	5.21	34.07
20	28	30.71	5.21	34.13

**Table B.1:** (continued on next page)

$\vartheta$ in °C	p in MPa	$A_P$ in %	$A_S$ in %	$A_{P/S}$ in %
20	26	30.82	5.20	34.24
20	24	30.87	5.18	34.28
20	22	30.94	5.13	34.31
20	20	31.01	5.09	34.36
20	18	31.05	5.04	34.36
20	16	31.08	4.95	34.33
20	14	31.16	4.82	34.33
20	12	31.17	4.70	34.26
20	10	31.20	4.58	34.21
20	8	31.10	4.47	34.05
20	6	31.10	4.43	34.02

**Table B.1:** The calculated P-wave, S-wave and velocity ratio anisotropy for the pressure cycle at 20°C of the sample Bo-AS-K3.

### Temperature increase

$\vartheta$ in °C	p in MPa	$A_P$ in %	$A_S$ in %	$A_{P/S}$ in %
20	12	31.11	4.68	34.19
30	12	31.34	4.57	34.34
40	12	31.41	4.59	34.42
50	12	31.53	4.54	34.51
60	12	31.61	4.51	34.56
70	12	31.70	4.57	34.68

**Table B.2:** The calculated P-wave, S-wave and velocity ratio anisotropy for the temperature increase of the sample Bo-AS-K3.

## Sample Bo-AS-K7

### First pressure cycle

$\vartheta$ in °C	p in MPa	$A_P$ in %	$A_S$ in %	$A_{P/S}$ in %
20	2	32.18	–	–
20	4	32.19	–	–
20	6	32.21	–	–
20	8	32.27	–	–
20	10	32.25	–	–
20	12	32.32	–	–
20	14	32.35	–	–
20	16	32.38	–	–
20	18	32.37	–	–
20	20	32.36	–	–
20	22	32.31	–	–
20	24	32.26	–	–
20	26	32.20	–	–
20	28	32.12	–	–
20	30	32.06	–	–
20	32	32.04	–	–
20	34	31.93	–	–
20	36	31.85	–	–
20	38	31.77	–	–
20	40	31.69	–	–
20	38	31.45	–	–
20	36	31.54	–	–
20	34	31.61	–	–
20	32	31.67	–	–
20	30	31.73	–	–
20	28	31.81	–	–
20	26	31.86	–	–
20	24	31.93	–	–
20	22	31.98	–	–
20	20	32.03	–	–
20	18	32.16	–	–

**Table B.3:** (continued on next page)

$\vartheta$ in $^{\circ}\text{C}$	p in MPa	$A_P$ in %	$A_S$ in %	$A_{P/S}$ in %
20	16	32.18	–	–
20	14	32.18	–	–
20	12	32.17	–	–
20	10	32.15	–	–
20	8	32.11	–	–
20	6	32.09	–	–
20	4	32.12	–	–
20	2	32.11	–	–

**Table B.3:** The calculated P-wave, S-wave and velocity ratio anisotropy for the first pressure cycle at  $20^{\circ}\text{C}$  of the sample Bo-AS-K7.

### Temperature increase

$\vartheta$ in $^{\circ}\text{C}$	p in MPa	$A_P$ in %	$A_S$ in %	$A_{P/S}$ in %
30	2	32.20	1.01	32.87
40	2	32.32	1.20	33.13
50	2	32.46	1.29	33.32
60	2	32.46	1.39	33.39
70	2	32.52	1.23	33.34
80	2	32.70	1.27	33.54

**Table B.4:** The calculated P-wave, S-wave and velocity ratio anisotropy for the temperature increase of the sample Bo-AS-K7.

### Second pressure cycle

$\vartheta$ in $^{\circ}\text{C}$	p in MPa	$A_P$ in %	$A_S$ in %	$A_{P/S}$ in %
80	10	32.18	0.54	32.55
80	12	32.29	0.25	32.46
80	14	32.15	0.25	32.32
80	16	32.21	0.21	32.36
80	18	32.22	0.11	32.29
80	20	32.17	0.04	32.20
80	22	32.19	0.16	32.08

**Table B.5:** (continued on next page)

$\vartheta$ in °C	p in MPa	$A_P$ in %	$A_S$ in %	$A_{P/S}$ in %
80	24	31.97	0.01	31.97
80	26	31.91	0.02	31.92
80	28	31.88	0.03	31.91
80	30	31.79	0.05	31.82
80	32	31.93	0.25	31.76
80	34	31.81	0.06	31.77
80	36	31.70	0.04	31.72
80	38	31.59	0.11	31.66
80	40	31.52	0.19	31.65
80	38	31.25	0.47	31.57
80	36	31.34	0.44	31.64
80	34	31.43	0.30	31.64
80	32	31.53	0.33	31.75
80	30	31.62	0.15	31.73
80	28	31.71	0.09	31.77
80	26	31.79	0.02	31.78
80	24	31.87	0.18	31.75
80	22	31.95	0.19	31.82
80	20	32.02	0.21	31.88
80	18	32.10	0.22	31.94
80	16	32.15	0.28	31.96
80	14	32.19	0.29	31.99
80	12	32.26	0.30	32.05
80	10	32.24	0.12	32.15
80	8	32.19	0.05	32.23
80	6	32.13	0.28	32.33
80	4	32.03	0.91	32.64
80	2	31.81	1.21	32.63

**Table B.5:** The calculated P-wave, S-wave and velocity ratio anisotropy for the second pressure cycle at 80 °C of the sample Bo-AS-K7.